arXiv:2610.38449v1 [cond-mat.supr-con] 28 Oct 2026

Layer-Parity Control of the Superconducting Diode Effect in Monolayer $NbSe_2$

Yusuf Wicaksono[1, *] and Toshikaze Kariyado[1, †]

[1] *International Center for Materials Nanoarchitectonics (WPI-MANA), National Institute for Materials Science, 1-1 Namiki, Tsukuba, Ibaraki 305-0044, Japan*

(Dated: October 30, 2026)

The superconducting diode effect is often associated with finite-momentum pairing, although model studies indicate that rectification reflects the asymmetry of the free energy about its minimum rather than the equilibrium pair momentum itself. Using a Wannier-based, self-consistent finite-$\mathbf{Q}$ Bogoliubov–de Gennes approach with a Fermi-surface-adaptive quadrature that converges the critical currents, we show that the layer parity and orientation of magnetic proximity select the diode response of monolayer $NbSe_2$. For in-plane exchange, the equilibrium pair momentum $\mathbf{Q}_{\rm eq}$ and the diode efficiency are both linear in the layer-odd exchange contrast: parallel proximity on the two Se sublayers is reciprocal, and antiparallel proximity doubles the response. An out-of-plane component separates the two observables. It leaves $\mathbf{Q}_{\rm eq}$ nearly unchanged but, through pair breaking, suppresses the efficiency by more than an order of magnitude and, at low temperature, reverses it. Purely out-of-plane exchange, for which C_3 symmetry forbids a helical term, keeps $\mathbf{Q}_{\rm eq} = 0$ yet produces a trigonal diode effect, controlled by the layer-even exchange and larger than the in-plane one above 0.65 meV at low temperature. Magnetic layer parity thus selects between a helical and a trigonal diode channel. The trigonal channel is an intrinsic, symmetry-allowed contribution to the field-free rectification reported in $NbSe_2/CrBr_3$ and predicts that two-sided out-of-plane proximity cancels it when antiparallel and, at the same exchange per layer, enhances it about fourfold when parallel, in the computed range.

Introduction. The most direct manifestation of nonreciprocal superconductivity is the superconducting diode effect (SDE), for which the positive and negative critical currents are unequal, $K_c^+ \neq |K_c^-|$ [1–4]. Superconducting nonreciprocity can emerge from broken inversion and time-reversal symmetry, spin–orbit coupling, Zeeman or exchange fields, and finite-momentum pairing [5–10]. These developments naturally connect the SDE to a helical superconducting state with an equilibrium pair momentum $Q_{\rm eq} \neq 0$. Ginzburg–Landau and model calculations have shown, however, that the diode efficiency is governed by the asymmetry of the free energy about its minimum rather than by the finite momentum itself, so that the two need not follow each other [4, 9, 11]; with threefold rotation symmetry, a cubic term even rectifies at zero pair momentum [4]. The two quantities probe different parts of the same free-energy landscape: $Q_{\rm eq}$ is fixed by its minimum, $\partial_Q \Omega_{\rm SC}(Q_{\rm eq}) = 0$, whereas the critical currents are extrema of the supercurrent $K(Q) \propto \partial_Q \Omega_{\rm SC}(Q)$ near directional depairing. For Ising superconductors, the in-plane diode effect has been analyzed in effective models of the K and K' pockets with a substrate that breaks the horizontal mirror [12, 13]. How the distinction plays out on the full multiband Fermi surface, and which magnetic configurations select which mechanism, has not been established.

In monolayer $1H$-$NbSe_2$, broken inversion symmetry and strong spin–orbit coupling generate Ising-type spin–valley locking, while superconductivity survives in the atomically thin limit [14–16]. How a time-reversal-breaking field rectifies depends on its orientation. In few-layer $NbSe_2$, the diode effect is driven by the out-of-plane field component and has been attributed to the valley-Zeeman coupling; an in-plane field does not rectify on its own, and its influence remains unexplained [17]. Magnetic proximity replaces the field by an interfacial exchange. $CrPS_4$ is an A-type antiferromagnet whose individual layers are magnetized out of plane [18]. On $CrPS_4$, $NbSe_2$ shows a proximity-induced diode effect in weak out-of-plane fields, and in $CrPS_4/NbSe_2/CrPS_4$ spin valves the response depends on the relative alignment of the two magnets; this was discussed in terms of finite-momentum pairing [19]. In $NbSe_2/CrBr_3$ [20], also magnetized out of plane, a large field-free diode effect, with polarity reversals traced to a history-dependent interfacial exchange, has instead been attributed to a cubic term that leaves the condensate at zero momentum [21]. Which orientations and layer configurations of the exchange rectify, and whether a finite pair momentum is involved, has thus remained open. Because van der Waals interfaces produce strongly layer-resolved exchange [22–24], the exchange on the two Se sublayers can differ, and its layer parity becomes a control parameter.

Here we combine a fully relativistic Wannier description of monolayer $NbSe_2$ with a self-consistent finite-$\mathbf{Q}$ Bogoliubov–de Gennes treatment that resolves the gapless depairing that sets the critical currents. The horizontal mirror assigns each diode channel to one magnetic layer parity. Layer-odd in-plane exchange produces a helical response, in which $\mathbf{Q}_{\rm eq}$ and the diode efficiency η are both linear in the exchange contrast; an out-of-plane component suppresses and, at low temperature, reverses η but leaves $\mathbf{Q}_{\rm eq}$ nearly unchanged. Layer-even out-of-plane exchange produces a trigonal diode effect

* Contact author: WICAKSONO.Yusuf@nims.go.jp
† Contact author: KARIYADO.Toshikaze@nims.go.jp

with $\mathbf{Q}_{\rm eq} = 0$, larger at strong exchange.

Model and finite-Q superconductivity. We describe monolayer 1H-$NbSe_2$ using a fully relativistic Wannier Hamiltonian constructed from Nb d and Se p orbitals [25–28]. The low-energy basis contains five Nb d orbitals and three Se p orbitals on each chalcogen sublayer, giving 11 spatial orbitals, or 22 spinor Wannier states. Magnetic proximity is introduced as a layer-selective exchange field acting on the Se orbitals,

$$H_{\rm ex} = \sum_{\ell=t,b} P_\ell \, \mathbf{D}_\ell \cdot \boldsymbol{\sigma}, \tag{1}$$

where P_ℓ projects onto the top (t) or bottom (b) Se sublayer and $\boldsymbol{\sigma}$ denotes the Pauli matrices in spin space. We write $\mathbf{D}_\ell = D_\ell(\sin\theta_\ell\cos\phi_\ell, \sin\theta_\ell\sin\phi_\ell, \cos\theta_\ell)$, with $\mathbf{a}_1 \parallel \hat{\mathbf{x}}$. The layer-even and layer-odd channels are $\mathbf{D}_\pm = (\mathbf{D}_b \pm \mathbf{D}_t)/2$, and we denote the in-plane exchange contrast by $\Delta\mathbf{D}_\parallel = 2\mathbf{D}_{-,\parallel}$, with x component $\Delta D_x = D_{b,x} - D_{t,x}$. We use $|\mathbf{D}_\ell| \le 1.84$ meV, with 1 meV as the reference value. On the Fermi surface, where the bottom Se sublayer carries on average 0.10–0.16 of the weight, $D_z = 1$ meV shifts the states by 0.10–0.20 meV, the Zeeman energy of a 1.7–3.5 T field, and in-plane exchange by less than 0.04 meV [29, Sec. S2.2], below the few-meV proximity splittings of transition-metal dichalcogenides on magnetic insulators [30, 31]. The out-of-plane component is also bounded by pair breaking, which closes the spectral gap between $D_z = 1$ and 1.5 meV [Fig. 2(f)].

To describe current-carrying superconducting states, Cooper pairs are allowed to acquire a center-of-mass wave vector $\mathbf{Q}$. Defining $\mathbf{k}_+ = \mathbf{k} + \mathbf{Q}/2$ and $\mathbf{k}_- = -\mathbf{k} + \mathbf{Q}/2$, the corresponding Bogoliubov–de Gennes Hamiltonian [7, 8, 32, 33] is

$$H_{\rm BdG}(\mathbf{k},\mathbf{Q}) = \begin{pmatrix} H_e(\mathbf{k}_+) - \mu & \hat{\Delta} \\ \hat{\Delta}^\dagger & -H_e^*(\mathbf{k}_-) + \mu \end{pmatrix}, \tag{2}$$

with $H_e(\mathbf{k}) = H_0(\mathbf{k}) + H_{\rm ex}$. We consider local spin-singlet pairing in the Nb d_{z^2}, $d_{x^2-y^2}$, and d_{xy} orbitals, $\hat{\Delta} = \Delta P_{\rm pair} \otimes i\sigma_y$, and determine $\Delta^\star(\mathbf{Q})$ self-consistently for each $\mathbf{Q}$. This choice, standard in models of Ising superconductivity in $NbSe_2$ [34] and consistent with phonon-mediated pairing [35], covers 0.73 of the Fermi-level weight in our model and is invariant under all crystal symmetries, so it does not bias the selection rules below [29, Sec. S6.3]. The singlet-only interaction retains the exchange-induced triplet correlations but no attractive triplet channel, which can reshape the in-plane diode response [13]. The pairing interaction is calibrated in pristine $NbSe_2$ to an order parameter $\Delta^\star = 0.4$ meV at $T = 0.12$ K, the value of the gap fitted to tunneling spectra of monolayer $NbSe_2$ at 0.34 K [36], and then kept fixed. Because pairing acts only in the Nb subspace, the model spectral gap is smaller, 0.24 meV [29, Sec. S2.3]. Unless stated otherwise, $\mu_0 = -2.4083$ eV and $T = 0.58$ K ($k_BT = 5\times10^{-5}$ eV), about $0.3\,T_c$ for the model $T_c \approx 1.9$ K estimated from $\Delta^\star(T)$ [29, Sec. S6.2]. We use the unreconstructed monolayer without the charge-density wave. The selection rules assume mirror-equivalent interfaces and do not depend on the exchange strength; the computed magnitudes are predictions of this effective model rather than parameter-free values for a specific heterostructure [29, Secs. S2.2 and S6.4].

The critical states are gapless [29, Sec. S6.1], and their supercurrent is carried by Bogoliubov Fermi surfaces that uniform meshes resolve poorly: with up to 1803×1803 points, η scatters by more than one percentage point [29, Sec. S3.1]. A Fermi-surface-adaptive quadrature (effective resolution 5427×5427; three levels for out-of-plane states) converges η to within ±0.1 percentage points; higher-precision differences below compare states on a common quadrature [29, Secs. S3 and S4.6].

On the selected self-consistent branch, we require $\Delta\Omega(\mathbf{Q}) = \Omega_{\rm SC}(\mathbf{Q}) - \Omega_{\rm N}(\mathbf{Q}) < 0$, where Ω is the grand potential per primitive cell of area $A_{\rm uc} = 10.1443$ Å^2. For representative states, the selected gap is the global minimum of $\Omega_{\rm SC}(\Delta)$ within the scalar-gap ansatz at the equilibrium and critical momenta [29, Sec. S6.5]. For a scan $\mathbf{Q} = Q\hat{\mathbf{n}}$, the sheet supercurrent, equilibrium momentum, and diode efficiency are

$$K(Q) = \frac{2e}{\hbar A_{\rm uc}}\frac{d\Omega_{\rm SC}(Q)}{dQ}, \qquad K(Q_{\rm eq}) = 0, \qquad \eta = \frac{K_c^+ - |K_c^-|}{K_c^+ + |K_c^-|}, \tag{3}$$

where $K_c^\pm$ are the positive and negative extrema of $K(Q)$ along the branch (1 A/m = 1 μA/μm). These extrema are intrinsic depairing currents of the uniform state; device switching can also involve vortices, edge barriers, Meissner currents, and orbital effects [37, 38]. Expanding about $Q = 0$ [7, 9, 11],

$$\Omega_{\rm SC}(Q) = \Omega_0 + \gamma_1 Q + \gamma_2 Q^2 + \gamma_3 Q^3 + \gamma_4 Q^4 + \cdots, \tag{4}$$

shows that the linear term shifts the free-energy minimum ($Q_{\rm eq} \simeq -\gamma_1/2\gamma_2$), whereas η depends on the part of the free energy that is odd about this minimum, near the depairing regions. A rigid shift of an even free energy produces no such part; to lowest order its coefficient is $\gamma_3 + 4\gamma_4 Q_{\rm eq}$. The two observables are therefore not tied to each other by symmetry.

Helical response and layer parity. Figure 1(b) shows $Q_{\rm eq}$ for one-sided, two-sided, and tilted textures scanned along $\hat{\mathbf{y}}$. All states collapse onto $Q_{\rm eq} = \chi_Q \Delta D_x$ with $\chi_Q = -17.8\times10^{-6}$ Å^{-1}meV^{-1}, to within 0.53×10^{-6} Å^{-1}. To this accuracy, the helical displacement depends neither on the layer-even exchange nor on the out-of-plane component. Symmetry explains why. The horizontal mirror σ_h exchanges the two Se sublayers and reverses in-plane axial vectors, so that parallel in-plane exchange ($\Delta D_x = 0$) is invariant under $\sigma_h\mathcal{T}$. This operation maps $\mathbf{Q} \to -\mathbf{Q}$ and enforces $\Omega_{\rm SC}(\mathbf{Q}) = \Omega_{\rm SC}(-\mathbf{Q})$, so that the parallel state is reciprocal [29, Sec. S1]. The

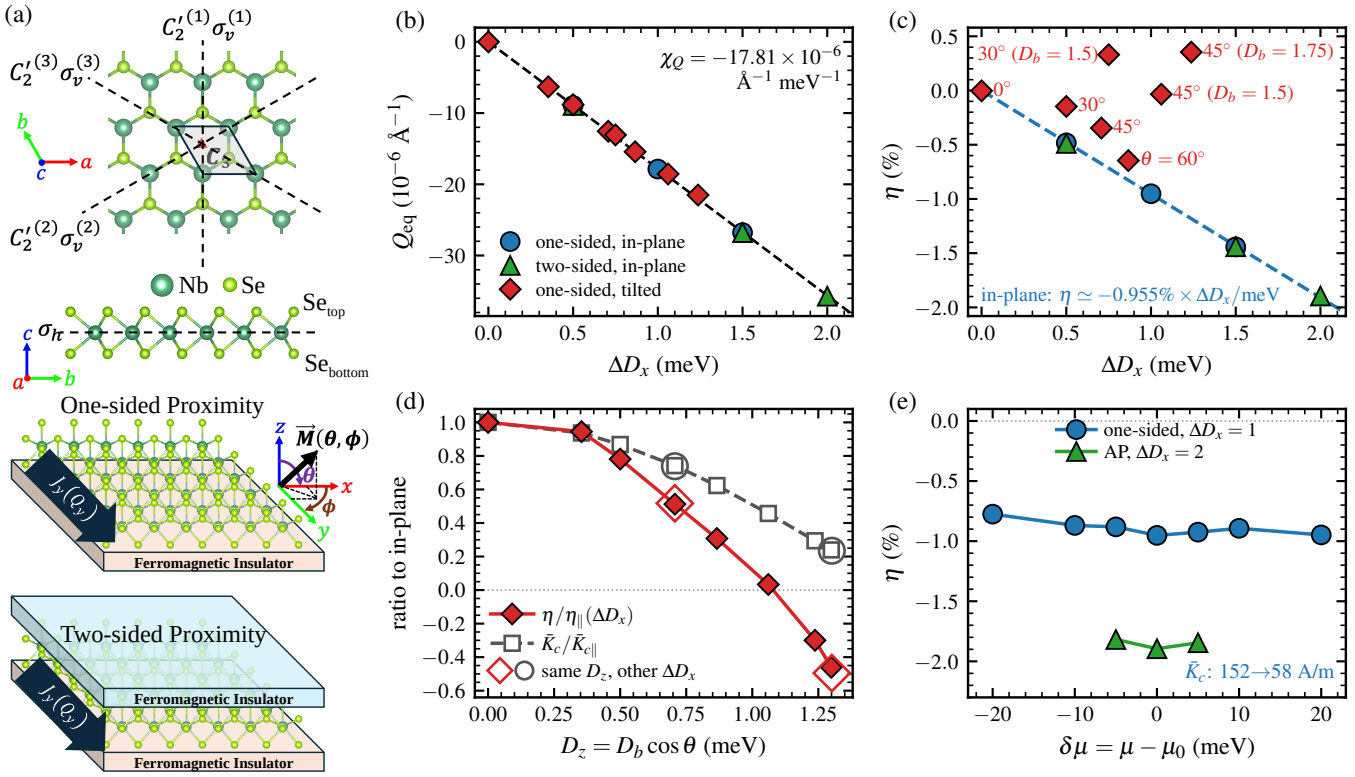


FIG. 1. **Helical response and its separation from rectification.** (a) Crystal structure of monolayer 1H-$NbSe_2$ and one- and two-sided magnetic-proximity geometries; (θ, ϕ) parameterize the proximity magnetization. Dashed lines mark the vertical mirrors σ_v and the C_2' axes; with $\mathbf{a}_1 \parallel \hat{\mathbf{x}}$ (zigzag), they run along $\hat{\mathbf{y}}$ and its C_3 images. (b) Equilibrium pair momentum versus the in-plane exchange contrast $\Delta D_x = D_{b,x} - D_{t,x}$ for one-sided and two-sided in-plane textures and for tilted one-sided textures (filled diamonds; Table S6), all scanned along $\hat{\mathbf{y}}$. The dashed line is $Q_{\rm eq} = \chi_Q \Delta D_x$. (c) Diode efficiency for the same states (except $\theta = 45°$, $D_b = 0.5$ meV, which lies on the in-plane line). In-plane textures (circles and triangles) follow a single line; tilted textures (diamonds, labeled by θ) have a smaller magnitude and, for $D_z \gtrsim 1.1$ meV, the opposite sign. (d) Efficiency of the tilted textures relative to the in-plane line at the same ΔD_x, and their mean critical current $\bar{K}_c = (K_c^+ + |K_c^-|)/2$ relative to the in-plane value, versus the out-of-plane component D_z. Large open symbols: states that repeat a D_z with a different ΔD_x. (e) Diode efficiency versus carrier filling $\delta\mu = \mu - \mu_0$ for the one-sided in-plane state ($D_b = 1$ meV) and the antiparallel (AP) texture. All results at $k_B T = 5 \times 10^{-5}$ eV on the converged quadrature (three-level for the tilted textures with $D_z > 1$ meV).

vertical mirror M_x combined with time reversal similarly makes textures with $D_{t,x} = D_{b,x} = 0$ reciprocal along $\hat{\mathbf{y}}$. The only term linear in both $\mathbf{Q}$ and the exchange is then $\mathbf{Q} \cdot (\hat{\mathbf{z}} \times \Delta\mathbf{D}_\parallel)$, and the helical momentum is $\mathbf{Q}_{\rm eq} \simeq \chi_Q \hat{\mathbf{z}} \times \Delta\mathbf{D}_\parallel$ [29, Sec. S4.4]. Scans along $\mathbf{b}_1$ reproduce its projections to 0.02×10^{-6} Å^{-1}.

For in-plane exchange, the diode efficiency follows the same rule [Fig. 1(c)]. It is linear in ΔD_x,

$$\eta \simeq -0.955\% \times \Delta D_x/\text{meV}, \tag{5}$$

over $0.5 \le \Delta D_x \le 2$ meV. Textures with the same ΔD_x but different layer-even exchange give the same η to within 0.005 percentage points [29, Sec. S4.2]. The critical-current scale, $\bar{K}_c \simeq 96$ A/m, is that of the unperturbed superconductor, because Ising spin–valley locking protects the condensate against in-plane exchange. Along $\mathbf{b}_1$, η also follows this projection, to within 4% [29, Sec. S4.4]. Parallel exchange on the two sublayers is reciprocal by symmetry, whereas antiparallel exchange (AP, $D_t = -D_b = -1$ meV) gives $Q_{\rm eq} = -35.7 \times 10^{-6}$ Å^{-1} and $\eta = -1.90\%$, twice the one-sided values. Reversing the magnetization reverses both [29, Sec. S4.3].

An out-of-plane exchange component breaks this correspondence. The tilted textures in Fig. 1(b) and (c) have the helical momentum predicted by their in-plane component but a much smaller $|\eta|$ than the in-plane line. Figure 1(d) shows that the suppression is controlled by $D_z = D_b \cos\theta$: states with equal D_z but different in-plane components give the same ratios [29, Sec. S4.1]. The most striking case is $\theta = 45°$ with $D_b = 1.5$ meV, which has $Q_{\rm eq} = -18.6 \times 10^{-6}$ Å^{-1}, almost the same as the in-plane state with $D_b = 1$ meV (-17.9×10^{-6} Å^{-1}), but an efficiency more than an order of magnitude smaller: -0.034% against -0.93% (-0.061% against -0.95% with two-level refinement). Unlike in-plane exchange, D_z is not protected by spin–

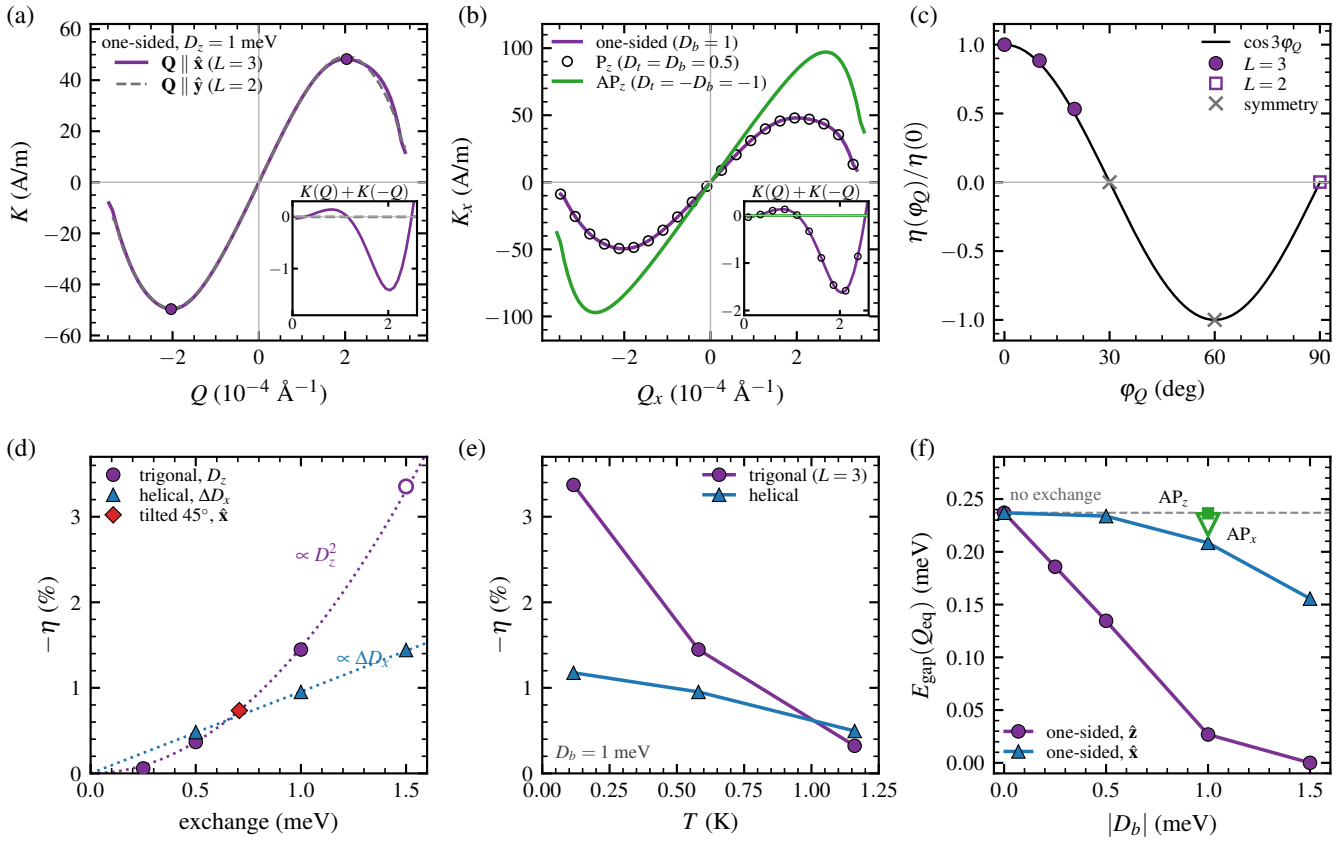


FIG. 2. **Trigonal diode channel of out-of-plane exchange.** (a) Sheet current for the one-sided out-of-plane texture ($D_z = 1$ meV) scanned along the mirror normal $\hat{\mathbf{x}}$ (filled circles: $K_c^{\pm}$) and along the mirror line $\hat{\mathbf{y}}$ (two-level quadrature). Inset: $K(Q)+K(-Q)$, twice the even-in-Q part, which vanishes along $\hat{\mathbf{y}}$. (b) Layer parity, all on the two-level quadrature: the parallel texture P_z reproduces the one-sided state with the same layer-even exchange $D_{+,z} = 0.5$ meV, while the antiparallel texture AP_z ($D_{+,z} = 0$) is reciprocal and not depaired. Inset as in (a). (c) Efficiency versus scan direction, normalized to $\varphi_Q = 0$; crosses are fixed by symmetry. (d) $-\eta$ versus exchange for the trigonal channel (one-sided D_z, along $\hat{\mathbf{x}}$; open circle: two-level quadrature) and the helical channel (one-sided ΔD_x, along $\hat{\mathbf{y}}$). The diamond is the tilted texture $\theta = 45°$, $D_b = 1$ meV, scanned along $\hat{\mathbf{x}}$ and plotted at its D_z. Dotted lines: $1.47\% \times (D_z/\text{meV})^2$ and $0.955\% \times \Delta D_x/\text{meV}$. (e) $-\eta$ versus temperature for $D_b = 1$ meV. (f) Spectral gap at the equilibrium momentum for one-sided out-of-plane ($\hat{\mathbf{z}}$) and in-plane ($\hat{\mathbf{x}}$) textures and for the antiparallel textures $D_t = -D_b$ ($\mathbf{Q}_{\rm eq} = 0$ for the out-of-plane textures); dashed line: no exchange. $k_BT = 5 \times 10^{-5}$ eV unless noted; three-level quadrature for the trigonal channel unless noted.

valley locking and is pair breaking: in this state it reduces the spectral gap at $Q_{\rm eq}$ from 0.21 meV (in-plane) to 7 μeV and reduces $\bar{K}_c$ by a factor of 2.2. The current asymmetry is, however, compensated rather than removed [29, Sec. S4.1]. It is carried by quasiparticle back-flow, in-plane mostly by the Γ pocket (-1.90 A/m, against $+0.10$ A/m from the K and K' pockets, to which effective models are restricted [12, 13]). D_z depairs the K and K' pockets, whose back-flow asymmetry, of opposite sign, grows to $+1.39$ A/m and cancels the Γ contribution (-1.40 A/m). A larger D_z tips this balance, and the rectification reverses near $D_z \approx 1.1$ meV [Fig. 1(c) and (d)], where the spectrum at $Q_{\rm eq}$ becomes gapless: $\theta = 30°$ with $D_b = 1.5$ meV ($D_z = 1.30$ meV) gives $\eta = +0.33\%$, now dominated by the K and K' pockets [29, Secs. S4.1 and S6.5], as for competing bands in Rashba superconductors [8]. The reversal persists on cooling to 0.12 K but not at 1.16 K, where thermal smearing removes the net asymmetry [29, Sec. S6.2]. $Q_{\rm eq}$ nevertheless stays near the in-plane line: it is fixed near the free-energy minimum, whereas the critical currents lie beyond the gap closing [29, Secs. S3.1 and S6.1].

Carrier filling and temperature also separate the two observables. Over $-20 \le \delta\mu \le 20$ meV [Fig. 1(e)], $Q_{\rm eq}$ changes by 0.27×10^{-6} Å^{-1} and $\bar{K}_c$ by a factor of 2.6, from 152 to 58 A/m. The efficiency stays between -0.78% and -0.95%. Lowering the temperature from $k_BT = 10^{-4}$ to 10^{-5} eV, in contrast, raises $|\eta|$ from 0.50% to 1.18% while $Q_{\rm eq}$ changes by 0.06×10^{-6} Å^{-1} [29, Sec. S6.2].

Rectification without helical momentum. For purely out-of-plane exchange, the magnetic point group of a one-sided texture is $3m'$: C_3 and the vertical mirrors

combined with time reversal. $M_x\mathcal{T}$ maps $(Q_x, Q_y) \to (Q_x, -Q_y)$ and therefore allows a linear term only along $\hat{\mathbf{x}}$, which C_3 then forbids. As a result, $\mathbf{Q} = 0$ is a stationary point of the free energy. The lowest odd term is cubic,

$$\Omega_{\mathrm{SC}}^{\mathrm{odd}} \propto D_z(Q_x^3 - 3Q_xQ_y^2) = D_z|\mathbf{Q}|^3 \cos 3\varphi_Q, \quad (6)$$

so a diode effect is allowed without any helical displacement [4, 21]. It is maximal along the mirror normal $\hat{\mathbf{x}}$ and vanishes along the mirror lines, including $\hat{\mathbf{y}}$.

The calculation confirms all three statements [Fig. 2(a) and (c)]. For $D_b = 1$ meV at $\theta = 0°$, the scan along $\hat{\mathbf{y}}$ is reciprocal ($\eta = -0.003\%$), and the scan along $\hat{\mathbf{x}}$ gives $|Q_{\mathrm{eq}}| < 0.1 \times 10^{-6}$ Å^{-1}, together with $\eta = -1.45\%$. Along every scanned direction (0°, 10°, 20°, and 90° from $\hat{\mathbf{x}}$; with $\pm\mathbf{Q}$ and the symmetries C_3 and $M_x\mathcal{T}$, these cover all inequivalent directions in 10° steps) the free energy is lowest at $\mathbf{Q} = 0$ over the whole superconducting branch. Since C_3 also makes the quadratic term isotropic, $\mathbf{Q} = 0$ is a local minimum in the full $\mathbf{Q}$ plane, and we identify it with the equilibrium [29, Sec. S4.6]. At $\varphi_Q = 10°$ and 20° the efficiency is 0.884 and 0.532 times that at 0°, close to $\cos 3\varphi_Q = 0.866$ and 0.500; the small excesses fit a symmetry-allowed $\cos 9\varphi_Q$ harmonic [29, Sec. S4.6].

Why can the efficiency be larger without any helical momentum, −1.45% against −0.93% for in-plane exchange of the same strength? Equation (4) gives the first part of the answer. Q_{eq} is set by the linear coefficient γ_1, which C_3 forbids here, whereas rectification requires only an odd part of Ω_{SC} about its minimum, which first enters through γ_3. A finite $\mathbf{Q}_{\mathrm{eq}}$ is thus neither necessary nor sufficient for a diode effect. The second part is the current scale. Writing $\eta = \Delta K/(2\bar{K}_c)$ with $\Delta K = K_c^+ - |K_c^-|$, the out-of-plane state has $\Delta K = -1.42$ A/m, about 0.8 times the in-plane value (−1.80 A/m). Its mean critical current, however, is halved (49.0 against 96.9 A/m). Unlike in-plane exchange, whose pair breaking Ising spin–valley locking suppresses, the out-of-plane exchange acts as a pair-breaking Zeeman field along the Ising axis and reduces the spectral gap at $\mathbf{Q} = 0$ to 27 μeV. The larger efficiency therefore reflects a comparable nonreciprocal current on a halved critical-current scale. Microscopically, the exchange adds to the Ising splitting in one valley and subtracts from it in the other. The trigonally warped pockets at K and K', whose odd contributions cancel in the time-reversal-symmetric state, then leave a net cubic term of the form of Eq. (6). The same mechanism underlies magnetochiral anisotropy in gated MoS_2 and has been invoked for the field-driven diode effect in few-layer $NbSe_2$ [5, 6, 17]; here the proximity exchange alone provides it, as proposed for $NbSe_2/CrBr_3$ [21].

The horizontal mirror leaves D_z invariant and exchanges the layers. With $D_\pm = (D_b \pm D_t)/2$, $\sigma_h\mathcal{T}$ reverses $\mathbf{Q}$, $D_{-,\parallel}$, and $D_{+,z}$ but keeps $D_{+,\parallel}$ and $D_{-,z}$. Only the layer-odd in-plane and the layer-even out-of-plane exchange can therefore rectify. A uniform Zeeman field is layer-even: an out-of-plane field rectifies, whereas an in-plane field alone does not, as observed in few-layer $NbSe_2$ [17]; in-plane rectification requires a one-sided interface or another source of σ_h breaking, such as a substrate [12, 13]. A proximity field on the Nb orbitals, which lie in the mirror plane, is layer-even by construction: for in-plane magnetization it cannot rectify on its own, and for out-of-plane magnetization it adds to the trigonal channel [29, Sec. S6.4]. Two-sided out-of-plane textures confirm this directly [Fig. 2(b)] [29, Sec. S4.6]. Parallel textures with $D_t = D_b = 0.25$ and 0.5 meV reproduce the one-sided states with the same $D_{+,z}$, $D_b = 0.5$ and 1 meV, in $\Delta^\star(Q)$ and $K(Q)$ to a relative 3×10^{-5}. The antiparallel texture $D_t = -D_b = -1$ meV is reciprocal ($|\eta| < 10^{-3}\%$), and its order parameter and spectral gap match the no-exchange values to 1 μeV. A layer-odd out-of-plane exchange, which couples only bands of opposite σ_h eigenvalue, thus acts on the condensate only at second order [29, Sec. S4.6]. Layer parity therefore acts oppositely on the two channels: the helical channel requires the layer-odd in-plane exchange, and the trigonal channel the layer-even out-of-plane exchange.

Figure 2(d)–(f) quantifies the trigonal channel. Its efficiency grows faster than linearly, $-\eta \simeq 1.47\% \times D_z|D_z|/\mathrm{meV}^2$ for $0.5 \le D_z \le 1.5$ meV and more steeply below (−0.058% at 0.25 meV), where opposite-sign gapped and gapless contributions compete, so that no linear term is resolved [29, Sec. S4.6]. It exceeds the linear helical response above $D_z \approx 0.65$ meV [Fig. 2(d)]. A tilted texture with $D_x = D_z = 0.71$ meV, scanned along $\hat{\mathbf{x}}$ through $\mathbf{Q}_{\mathrm{eq}}$, gives $\eta = -0.735\%$, against −0.729% interpolated for purely out-of-plane exchange of the same D_z: the in-plane component leaves the trigonal channel intact, whereas D_z strongly suppresses the helical one [Fig. 1(d)]. The spectral gap explains this asymmetry [Fig. 2(f)]. Out-of-plane exchange lowers E_{gap} linearly, from 0.24 meV by 0.42 meV per meV of $D_{+,z}$ ($D_{+,z} = D_b/2$ for one-sided textures), to 27 μeV at $D_b = 1$ meV and to zero at 1.5 meV; in-plane exchange reduces the gap at $\mathbf{Q}_{\mathrm{eq}}$ only weakly, to 0.21 and 0.16 meV at 1 and 1.5 meV; and AP_z leaves it unchanged. At $D_z = 1.5$ meV, near the Pauli limit, the superconducting solution remains the global minimum at the tested momenta within the scalar-gap ansatz [29, Sec. S6.5]. Temperature acts on the same small scale [Fig. 2(e)]. Between $k_BT = 10^{-4}$ and 10^{-5} eV (1.16 and 0.12 K), the trigonal $|\eta|$ increases tenfold, from 0.32% to 3.37%, against a factor of 2.4 for the helical channel, which is stronger at 1.16 K. The current asymmetry $|\Delta K|$ grows 35-fold while $\bar{K}_c$ grows 3.4-fold. This is consistent with an asymmetry that originates in the nearly gapless, exchange-split quasiparticles, whose structure on the scale of tens of μeV is washed out by thermal smearing; at 1.16 K the state is gapless already at $\mathbf{Q} = 0$. At 0.58 K, a larger gap does not change the ranking. Recalibrating the coupling to $\Delta^\star = 0.6$ meV, which raises the spectral gap toward the measured one, leaves $\mathbf{Q}_{\mathrm{eq}}$ nearly unchanged and lowers the helical $|\eta|$ to 0.79%, while the trigonal efficiency at $D_z = 1$ meV stays at −1.51% [29, Sec. S6.3].

Conclusion. We have shown that in magnetically prox-

imitized monolayer $NbSe_2$ the layer parity and orientation of the exchange select the superconducting diode channel, and that the equilibrium helical momentum and the diode efficiency respond differently within the same finite-$\mathbf{Q}$ free-energy landscape. For in-plane exchange, both are linear in the layer-odd exchange contrast $\hat{\mathbf{z}} \times \Delta\mathbf{D}_{\parallel}$: parallel proximity is reciprocal, and antiparallel proximity doubles the response. An out-of-plane exchange component leaves the helical momentum nearly unchanged but, by depairing the K and K' pockets, suppresses the rectification by more than an order of magnitude and, at low temperature, reverses it. Temperature changes the efficiency at nearly constant $\mathbf{Q}_{\mathrm{eq}}$. A finite helical momentum is therefore not a quantitative proxy for the diode efficiency. Purely out-of-plane exchange realizes the opposite limit: a trigonal diode effect with $\mathbf{Q}_{\mathrm{eq}} = 0$, larger than the in-plane one above 0.65 meV at low temperature because the same exchange that creates the asymmetry also lowers the critical current. Layer-odd out-of-plane exchange is reciprocal and leaves the condensate essentially unchanged. A layer-resolved proximity structure therefore chooses not only whether a monolayer superconductor rectifies, but also by which mechanism, within an effective model of mirror-equivalent interfaces. The trigonal channel is an intrinsic, symmetry-allowed contribution to the field-free rectification with a zero-momentum condensate reported in $NbSe_2/CrBr_3$ [21], whose measured efficiencies, up to 36%, exceed the computed depairing values by an order of magnitude. For monolayer devices it predicts that the polarity follows the magnetization of the interfacial magnetic layer rather than the net moment, consistent with the history-dependent reversals observed there; that the efficiency is largest for currents along the zigzag direction, with opposite signs for zigzag directions 60° apart, and vanishes along the armchair direction; that out-of-plane proximity on both sides cancels the rectification when antiparallel and enhances it about fourfold when parallel, at 0.5–0.75 meV per layer, as can be tested in $CrPS_4/NbSe_2/CrPS_4$ spin valves [19]; and that the efficiency grows faster than linearly with the exchange and strongly on cooling, because it is dominated by gapless depairing. In $2H$ bilayers, inversion makes parallel textures reciprocal for either orientation, so that out-of-plane spin valves can rectify only when antiparallel [29, Sec. S6.4].

Data availability. The data that support the findings of this article are available from the authors upon reasonable request.

Acknowledgments. The calculations in this study were performed on the Numerical Materials Simulator at NIMS. This work was supported by JSPS KAKENHI Grant No. JP24K06968 from MEXT, Japan.

[1] F. Ando, Y. Miyasaka, T. Li, J. Ishizuka, T. Arakawa, Y. Shiota, T. Moriyama, Y. Yanase, and T. Ono, Observation of superconducting diode effect, Nature **584**, 373 (2020).
[2] M. Nadeem, M. S. Fuhrer, and X. Wang, The superconducting diode effect, Nat. Rev. Phys. **5**, 558 (2023).
[3] M. Davydova, M. Geier, and L. Fu, Nonreciprocal superconductivity, Sci. Adv. **10**, eadr4817 (2024).
[4] D. Shaffer and A. Levchenko, Theories of superconducting diode effects (2025), arXiv:2510.25864 [cond-mat.supr-con].
[5] R. Wakatsuki, Y. Saito, S. Hoshino, Y. M. Itahashi, T. Ideue, M. Ezawa, Y. Iwasa, and N. Nagaosa, Nonreciprocal charge transport in noncentrosymmetric superconductors, Sci. Adv. **3**, e1602390 (2017).
[6] S. Hoshino, R. Wakatsuki, K. Hamamoto, and N. Nagaosa, Nonreciprocal charge transport in two-dimensional noncentrosymmetric superconductors, Phys. Rev. B **98**, 054510 (2018).
[7] N. F. Q. Yuan and L. Fu, Supercurrent diode effect and finite-momentum superconductors, Proc. Natl. Acad. Sci. U.S.A. **119**, e2119548119 (2022).
[8] A. Daido, Y. Ikeda, and Y. Yanase, Intrinsic superconducting diode effect, Phys. Rev. Lett. **128**, 037001 (2022).
[9] J. J. He, Y. Tanaka, and N. Nagaosa, A phenomenological theory of superconductor diodes, New J. Phys. **24**, 053014 (2022).
[10] S. Ilić and F. S. Bergeret, Theory of the supercurrent diode effect in Rashba superconductors with arbitrary disorder, Phys. Rev. Lett. **128**, 177001 (2022).
[11] A. Daido and Y. Yanase, Superconducting diode effect and nonreciprocal transition lines, Phys. Rev. B **106**, 205206 (2022).
[12] I. Bankier, L. Attias, A. Levchenko, and M. Khodas, Superconducting diode effect in Ising superconductors, Phys. Rev. B **111**, L180505 (2025).
[13] A. Levchenko and M. Khodas, Superconducting diode effect from field-induced $s+if$ pairing in Ising superconductors (2026), arXiv:2609.01476 [cond-mat.supr-con].
[14] M. M. Ugeda, A. J. Bradley, Y. Zhang, S. Onishi, Y. Chen, W. Ruan, C. Ojeda-Aristizabal, H. Ryu, M. T. Edmonds, H.-Z. Tsai, A. Riss, S.-K. Mo, D. Lee, A. Zettl, Z. Hussain, Z.-X. Shen, and M. F. Crommie, Characterization of collective ground states in single-layer $NbSe_2$, Nat. Phys. **12**, 92 (2016).
[15] X. Xi, Z. Wang, W. Zhao, J.-H. Park, K. T. Law, H. Berger, L. Forró, J. Shan, and K. F. Mak, Ising pairing in superconducting $NbSe_2$ atomic layers, Nat. Phys. **12**, 139 (2016).
[16] S. C. de la Barrera, M. R. Sinko, D. P. Gopalan, N. Sivadas, K. L. Seyler, K. Watanabe, T. Taniguchi, A. W. Tsen, X. Xu, D. Xiao, and B. M. Hunt, Tuning Ising superconductivity with layer and spin-orbit coupling in two-dimensional transition-metal dichalcogenides, Nat. Commun. **9**, 1427 (2018).
[17] L. Bauriedl, C. Bäuml, L. Fuchs, C. Baumgartner, N. Paulik, J. M. Bauer, K.-Q. Lin, J. M. Lupton, T. Taniguchi, K. Watanabe, C. Strunk, and N. Paradiso, Supercurrent diode effect and magnetochiral anisotropy in few-layer $NbSe_2$, Nat. Commun. **13**, 4266 (2022).

[18] Y. Peng, S. Ding, M. Cheng, Q. Hu, J. Yang, F. Wang, M. Xue, Z. Liu, Z. Lin, M. Avdeev, Y. Hou, W. Yang, Y. Zheng, and J. Yang, Magnetic structure and metamagnetic transitions in the van der Waals antiferromagnet $CrPS_4$, Adv. Mater. **32**, 2001200 (2020).

[19] J. Yun, S. Son, J. Shin, G. Park, K. Zhang, Y. J. Shin, J.-G. Park, and D. Kim, Magnetic proximity-induced superconducting diode effect and infinite magnetoresistance in a van der Waals heterostructure, Phys. Rev. Research **5**, L022064 (2023).

[20] S. Kezilebieke, M. N. Huda, V. Vaňo, M. Aapro, S. C. Ganguli, O. J. Silveira, S. Głodzik, A. S. Foster, T. Ojanen, and P. Liljeroth, Topological superconductivity in a van der Waals heterostructure, Nature **588**, 424 (2020).

[21] S. Sun, L. Xiao, C. Shen, B. Hao, J.-P. Peng, Z. Zhu, F. Wang, Q. Han, Y.-Q. Bie, S. Wang, T. Zhou, D. Yu, and B.-C. Lin, Large field-free superconducting diode effect with nonmonotonic polarity reversals in $NbSe_2/CrBr_3$ heterostructures (2026), arXiv:2608.19099 [cond-mat.supr-con].

[22] D. Zhong, K. L. Seyler, X. Linpeng, N. P. Wilson, T. Taniguchi, K. Watanabe, M. A. McGuire, K.-M. C. Fu, D. Xiao, W. Yao, and X. Xu, Layer-resolved magnetic proximity effect in van der Waals heterostructures, Nat. Nanotechnol. **15**, 187 (2020).

[23] H. Matsuoka, T. Habe, Y. Iwasa, M. Koshino, and M. Nakano, Spontaneous spin-valley polarization in $NbSe_2$ at a van der Waals interface, Nat. Commun. **13**, 5129 (2022).

[24] Y. Wicaksono and T. Kariyado, Layer-selective proximity symmetry breaking enables anomalous and nonlinear Hall responses in $1H$-NbX_2 ($X = \mathrm{S}, \mathrm{Se}, \mathrm{Te}$), Phys. Rev. B **114**, L171402 (2026).

[25] P. Giannozzi, S. Baroni, N. Bonini, M. Calandra, R. Car, C. Cavazzoni, D. Ceresoli, G. L. Chiarotti, M. Cococcioni, I. Dabo, A. Dal Corso, S. de Gironcoli, S. Fabris, G. Fratesi, R. Gebauer, U. Gerstmann, C. Gougoussis, A. Kokalj, M. Lazzeri, L. Martin-Samos, N. Marzari, F. Mauri, R. Mazzarello, S. Paolini, A. Pasquarello, L. Paulatto, C. Sbraccia, S. Scandolo, G. Sclauzero, A. P. Seitsonen, A. Smogunov, P. Umari, and R. M. Wentzcovitch, QUANTUM ESPRESSO: a modular and open-source software project for quantum simulations of materials, J. Phys.: Condens. Matter **21**, 395502 (2009).

[26] P. Giannozzi, O. Andreussi, T. Brumme, O. Bunau, M. Buongiorno Nardelli, M. Calandra, R. Car, C. Cavazzoni, D. Ceresoli, M. Cococcioni, N. Colonna, I. Carnimeo, A. Dal Corso, S. de Gironcoli, P. Delugas, R. A. DiStasio, A. Ferretti, A. Floris, G. Fratesi, G. Fugallo, R. Gebauer, U. Gerstmann, F. Giustino, T. Gorni, J. Jia, M. Kawamura, H.-Y. Ko, A. Kokalj, E. Küçükbenli, M. Lazzeri, M. Marsili, N. Marzari, F. Mauri, N. L. Nguyen, H.-V. Nguyen, A. Otero-de-la-Roza, L. Paulatto, S. Poncé, D. Rocca, R. Sabatini, B. Santra, M. Schlipf, A. P. Seitsonen, A. Smogunov, I. Timrov, T. Thonhauser, P. Umari, N. Vast, X. Wu, and S. Baroni, Advanced capabilities for materials modelling with Quantum ESPRESSO, J. Phys.: Condens. Matter **29**, 465901 (2017).

[27] A. A. Mostofi, J. R. Yates, Y.-S. Lee, I. Souza, D. Vanderbilt, and N. Marzari, wannier90: A tool for obtaining maximally-localised Wannier functions, Comput. Phys. Commun. **178**, 685 (2008).

[28] G. Pizzi, V. Vitale, R. Arita, S. Blügel, F. Freimuth, G. Géranton, M. Gibertini, D. Gresch, C. Johnson, T. Koretsune, J. Ibañez-Azpiroz, H. Lee, J.-M. Lihm, D. Marchand, A. Marrazzo, Y. Mokrousov, J. I. Mustafa, Y. Nohara, Y. Nomura, L. Paulatto, S. Poncé, T. Ponweiser, J. Qiao, F. Thöle, S. S. Tsirkin, M. Wierzbowska, N. Marzari, D. Vanderbilt, I. Souza, A. A. Mostofi, and J. R. Yates, Wannier90 as a community code: new features and applications, J. Phys.: Condens. Matter **32**, 165902 (2020).

[29] See the Supplemental Material appended to this article for the symmetry analysis, the Wannier–BdG and Fermi-surface-adaptive quadrature details, the convergence tests in mesh, refinement level, and momentum spacing, the temperature and gap-size dependence, the stability of the superconducting solutions, the scope of the proximity model, a pocket-resolved decomposition of the helical current asymmetry, and the full tables of critical currents. The Supplemental Material includes Refs. [30–32, 36, 39–46].

[30] C. Zhao, T. Norden, P. Zhang, P. Zhao, Y. Cheng, F. Sun, J. P. Parry, P. Taheri, J. Wang, Y. Yang, T. Scrace, K. Kang, S. Yang, G.-X. Miao, R. Sabirianov, G. Kioseoglou, W. Huang, A. Petrou, and H. Zeng, Enhanced valley splitting in monolayer WSe_2 due to magnetic exchange field, Nat. Nanotechnol. **12**, 757 (2017).

[31] K. Zollner, P. E. Faria Junior, and J. Fabian, Proximity exchange effects in $MoSe_2$ and WSe_2 heterostructures with CrI_3: Twist angle, layer, and gate dependence, Phys. Rev. B **100**, 085128 (2019).

[32] P.-G. de Gennes, *Superconductivity of Metals and Alloys*, Frontiers in Physics, Vol. 24 (W. A. Benjamin, New York, 1966).

[33] P. Fulde and R. A. Ferrell, Superconductivity in a strong spin-exchange field, Phys. Rev. **135**, A550 (1964).

[34] W.-Y. He, B. T. Zhou, J. J. He, N. F. Q. Yuan, T. Zhang, and K. T. Law, Magnetic field driven nodal topological superconductivity in monolayer transition metal dichalcogenides, Commun. Phys. **1**, 40 (2018).

[35] C.-S. Lian, C. Si, and W. Duan, Unveiling charge-density wave, superconductivity, and their competitive nature in two-dimensional $NbSe_2$, Nano Lett. **18**, 2924 (2018).

[36] P. Dreher, W. Wan, A. Chikina, M. Bianchi, H. Guo, R. Harsh, S. Mañas-Valero, E. Coronado, A. J. Martínez-Galera, P. Hofmann, J. A. Miwa, and M. M. Ugeda, Proximity effects on the charge density wave order and superconductivity in single-layer $NbSe_2$, ACS Nano **15**, 19430 (2021).

[37] Y. Hou, F. Nichele, H. Chi, A. Lodesani, Y. Wu, M. F. Ritter, D. Z. Haxell, M. Davydova, S. Ilić, O. Glezakou-Elbert, A. Varambally, F. S. Bergeret, A. Kamra, L. Fu, P. A. Lee, and J. S. Moodera, Ubiquitous superconducting diode effect in superconductor thin films, Phys. Rev. Lett. **131**, 027001 (2023).

[38] D. Kochan, A. Costa, I. Zhumagulov, and I. Žutić, Phenomenological theory of the supercurrent diode effect: The Lifshitz invariant (2023), arXiv:2303.11975 [cond-mat.supr-con].

[39] J. P. Perdew, A. Ruzsinszky, G. I. Csonka, O. A. Vydrov, G. E. Scuseria, L. A. Constantin, X. Zhou, and K. Burke, Restoring the density-gradient expansion for exchange in solids and surfaces, Phys. Rev. Lett. **100**, 136406 (2008).

[40] G. Kresse and D. Joubert, From ultrasoft pseudopotentials to the projector augmented-wave method, Phys. Rev. B **59**, 1758 (1999).

[41] A. Dal Corso, Pseudopotentials periodic table: From H to Pu, Comput. Mater. Sci. **95**, 337 (2014).
[42] N. Marzari, D. Vanderbilt, A. De Vita, and M. C. Payne, Thermal contraction and disordering of the Al(110) surface, Phys. Rev. Lett. **82**, 3296 (1999).
[43] A. Dal Corso and A. Mosca Conte, Spin-orbit coupling with ultrasoft pseudopotentials: Application to Au and Pt, Phys. Rev. B **71**, 115106 (2005).
[44] N. Marzari, A. A. Mostofi, J. R. Yates, I. Souza, and D. Vanderbilt, Maximally localized Wannier functions: Theory and applications, Rev. Mod. Phys. **84**, 1419 (2012).
[45] A. A. Mostofi, J. R. Yates, G. Pizzi, Y.-S. Lee, I. Souza, D. Vanderbilt, and N. Marzari, An updated version of wannier90: A tool for obtaining maximally-localised Wannier functions, Comput. Phys. Commun. **185**, 2309 (2014).
[46] N. N. Bogoliubov, A new method in the theory of superconductivity. I, Sov. Phys. JETP **7**, 41 (1958).

Supplemental Material for "Layer-Parity Control of the Superconducting Diode Effect in Monolayer $NbSe_2$"

Yusuf Wicaksono and Toshikaze Kariyado

International Center for Materials Nanoarchitectonics (WPI-MANA), National Institute for Materials Science, 1-1 Namiki, Tsukuba, Ibaraki 305-0044, Japan

This Supplemental Material provides the symmetry analysis, numerical implementation, convergence tests, and additional results supporting the main-text conclusions on the superconducting diode effect (SDE) in magnetically proximitized monolayer $NbSe_2$. The material is organized as follows. Section S1 derives the symmetry constraints associated with the horizontal mirror σ_h and the combined antiunitary operation $\sigma_h\mathcal{T}$, with particular emphasis on the reciprocal parallel two-sided configuration and the layer-parity selection rules. Section S2 summarizes the fully relativistic Wannier Hamiltonian, layer-selective proximity exchange, finite-$\mathbf{Q}$ Bogoliubov–de Gennes (BdG) formulation, self-consistent pairing procedure, thermodynamic potential, supercurrent, and critical-current extraction. Section S3 establishes numerical convergence and the reciprocity floor, including the Fermi-surface-adaptive Brillouin-zone quadrature and its refinement-level convergence, Q-grid resolution, self-consistency criteria, and the no-exchange and parallel-state checks. Section S4 presents the complete results for the helical response (angular and exchange-strength scans, a pocket-resolved decomposition of the current asymmetry, layer-even exchange, parallel/antiparallel and single-layer textures, and the vector form of the response) and for the trigonal channel generated by layer-even out-of-plane exchange. Section S5 gives the chemical-potential dependence of the critical currents and the diode efficiency. Finally, Section S6 collects superconducting-stability and robustness checks, including a representative finite-Q branch, the temperature dependence, the sensitivity to the magnitude of the superconducting gap, the pairing subspace, the scope of the proximity model, and the stability of the selected solutions within the scalar-gap ansatz. Reference numbers refer to the list at the end of the main text.

S1. SYMMETRY CONSTRAINTS, MAGNETIC LAYER PARITY, AND RECIPROCITY

This section establishes the symmetry constraint responsible for the reciprocal parallel (P) configuration used in the main text and verifies it numerically. We first derive the constraint at the normal-state and Bogoliubov–de Gennes (BdG) Hamiltonian levels, then obtain the corresponding selection rules for the finite-Q free energy. The numerical calculations are finally used to distinguish symmetry-enforced reciprocity from an accidental cancellation of the positive- and negative-current branches.

Throughout this Supplemental Material, $\mathbf{k}$ and $\mathbf{Q}$ denote physical wave vectors in Å^{-1}. Each scan varies the pair momentum along a fixed in-plane unit vector $\hat{\mathbf{n}}$, $\mathbf{Q} = Q\hat{\mathbf{n}}$, with $\hat{\mathbf{n}} = \hat{\mathbf{y}}$ (armchair) for the in-plane exchange and $\hat{\mathbf{n}} = \hat{\mathbf{x}}$ (zigzag) for the out-of-plane exchange unless stated otherwise; $Q \equiv Q_y$ or Q_x accordingly. Grand potentials are energies per primitive cell, and K denotes the two-dimensional sheet current along $\hat{\mathbf{n}}$ in A/m, $K = (2e/\hbar A_{\mathrm{uc}})\, d\Omega_{\mathrm{SC}}/dQ$, with $e > 0$. When the in-plane case is discussed explicitly we write K_y and Q_y. The diode efficiency η is quoted in percent, and differences of η in percentage points; relative changes of other quantities are given as ratios, fractions, or absolute values, so that the percent sign refers only to η. The dimensionless fractional coordinates $\boldsymbol{\kappa}$ and $\mathbf{q}$ used in the code are distinguished explicitly in Sec. S2.3.

S1.1. Horizontal mirror symmetry of monolayer $1H$-$NbSe_2$

Monolayer $1H$-$NbSe_2$ possesses a horizontal mirror σ_h whose mirror plane passes through the Nb layer. It exchanges the top and bottom Se sublayers,

$$\sigma_h : \quad (x, y, z) \to (x, y, -z). \tag{S1}$$

Because the proximity magnetization is an axial vector, its transformation under an improper spatial operation differs from that of a polar vector. For σ_h,

$$(M_x, M_y, M_z) \xrightarrow{\sigma_h} (-M_x, -M_y, M_z). \tag{S2}$$

Thus an in-plane magnetic moment changes sign under σ_h, while the top and bottom Se sublayers are interchanged. Time reversal acts as

$$\mathcal{T} : \quad \mathbf{M} \to -\mathbf{M}, \qquad \mathbf{k} \to -\mathbf{k}, \qquad \mathbf{Q} \to -\mathbf{Q}. \tag{S3}$$

For the in-plane configurations considered here, the additional sign reversal of the moment under $\mathcal{T}$ compensates the sign change generated by σ_h.

For collinear in-plane proximity exchange, we introduce the layer-even and layer-odd combinations

$$D_+ = \frac{D_b + D_t}{2}, \qquad D_- = \frac{D_b - D_t}{2} = \frac{\Delta D}{2}, \tag{S4}$$

where $\Delta D = D_b - D_t$ is the exchange contrast used in the main text. Since σ_h exchanges the two sublayers while $\sigma_h\mathcal{T}$ restores the direction of an in-plane axial exchange field,

$$\sigma_h\mathcal{T} : \; D_+ \to D_+, \; D_- \to -D_-, \; Q_y \to -Q_y. \tag{S5}$$

S1.2. Hamiltonian-level origin of reciprocity in the parallel configuration

It is useful to make the reciprocity constraint explicit already at the Hamiltonian level. Let

$$\mathcal{A} \equiv \sigma_h \mathcal{T} = U_{\mathcal{A}} \mathcal{K} \tag{S6}$$

denote the combined antiunitary operation, where $\mathcal{K}$ is complex conjugation and $U_{\mathcal{A}}$ contains the spin-orbital action of $\sigma_h \mathcal{T}$. The nonmagnetic relativistic Wannier Hamiltonian is invariant under both σ_h and $\mathcal{T}$. Including the layer-selective in-plane exchange therefore gives

$$\mathcal{A} H_e(\mathbf{k}; D_+, D_-) \mathcal{A}^{-1} = H_e(-\mathbf{k}; D_+, -D_-). \tag{S7}$$

The pairing channel used in this work is also compatible with $\mathcal{A}$. The active Nb orbitals d_{z^2}, $d_{x^2-y^2}$, and d_{xy} are even under σ_h, while the local spin-singlet matrix $i\sigma_y$ is invariant under time reversal up to the superconducting gauge phase. Choosing the self-consistent scalar gap Δ real, the pairing matrix therefore maps onto itself under $\mathcal{A}$. The corresponding Nambu-space antiunitary operator can be written as

$$\widetilde{\mathcal{A}} = \begin{pmatrix} U_{\mathcal{A}} & 0 \\ 0 & U_{\mathcal{A}}^* \end{pmatrix} \mathcal{K}, \tag{S8}$$

and the finite-Q_y BdG Hamiltonian obeys

$$\widetilde{\mathcal{A}}\, H_{\mathrm{BdG}}(\mathbf{k}, Q_y; D_+, D_-)\, \widetilde{\mathcal{A}}^{-1} = H_{\mathrm{BdG}}(-\mathbf{k}, -Q_y; D_+, -D_-). \tag{S9}$$

Consequently the quasiparticle spectra are paired according to

$$E_n(\mathbf{k}, Q_y; D_+, D_-) = E_n(-\mathbf{k}, -Q_y; D_+, -D_-), \tag{S10}$$

up to a relabeling of BdG eigenstates. Because the pairing functional and the Brillouin-zone sum are invariant under $\mathbf{k} \to -\mathbf{k}$, the self-consistent thermodynamic potential satisfies

$$\Omega_{\mathrm{SC}}(Q_y; D_+, D_-) = \Omega_{\mathrm{SC}}(-Q_y; D_+, -D_-). \tag{S11}$$

The equal parallel configuration has $D_t = D_b$ and hence $D_- = 0$. Equation (S11) therefore reduces directly to

$$\Omega_{\mathrm{SC}}^P(Q_y) = \Omega_{\mathrm{SC}}^P(-Q_y). \tag{S12}$$

This result is exact within the ideal mirror-equivalent model. In particular, every odd power of Q_y is forbidden:

$$\Omega_{\mathrm{SC}}^P(Q_y) = \Omega_0 + \gamma_2 Q_y^2 + \gamma_4 Q_y^4 + \gamma_6 Q_y^6 + \cdots. \tag{S13}$$

The thermodynamic current is therefore strictly odd,

$$K_y^P(Q_y) = \frac{2e}{\hbar A_{\mathrm{uc}}} \frac{\partial \Omega_{\mathrm{SC}}^P}{\partial Q_y} = \frac{2e}{\hbar A_{\mathrm{uc}}} \left(2\gamma_2 Q_y + 4\gamma_4 Q_y^3 + 6\gamma_6 Q_y^5 + \cdots\right), \tag{S14}$$

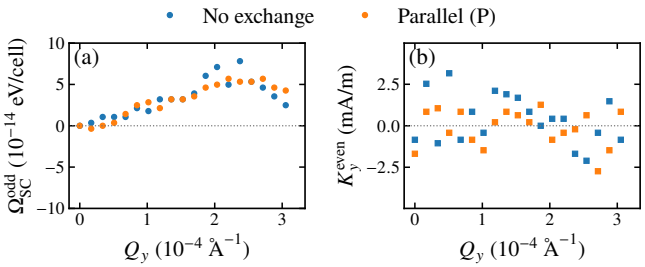


FIG. S1. **Numerical reciprocity controls for pristine and parallel magnetic configurations** (uniform 201 × 201 + third9 mesh, $k_B T = 10^{-5}$ eV). (a) Odd part of the superconducting thermodynamic potential, $\Omega_{\mathrm{SC}}^{\mathrm{odd}}(Q_y) = [\Omega_{\mathrm{SC}}(Q_y) - \Omega_{\mathrm{SC}}(-Q_y)]/2$, for pristine (no-exchange) monolayer $NbSe_2$ and for equal parallel (P) in-plane exchange on the top and bottom Se sublayers. (b) Corresponding even part of the thermodynamic current, $K_y^{\mathrm{even}}(Q_y) = [K_y(Q_y) + K_y(-Q_y)]/2$. Only $Q_y \geq 0$ is shown because the plotted combinations already encode the comparison between $\pm Q_y$. The momentum axis is in 10^{-4} Å^{-1}; the ordinate units are 10^{-14} eV/cell in (a) and mA/m in (b). In both cases the residual signals remain at the numerical reciprocity floor: the odd free-energy component is of order 10^{-14} eV/cell and the forbidden even-current component is of order 10^{-5} of the total current scale.

so that

$$K_y^P(-Q_y) = -K_y^P(Q_y). \tag{S15}$$

The same symmetry maps every stable superconducting solution at $+Q_y$ to one at $-Q_y$, so the stable branch is symmetric and its current extrema satisfy

$$K_c^- = -K_c^+, \qquad \eta = 0. \tag{S16}$$

Equation (S12) alone permits either a unique minimum at $Q_y = 0$ or a pair of degenerate minima at $\pm Q_0$. In the present P calculation the central minimum is unique; hence $Q_{\mathrm{eq}} = 0$ within numerical accuracy.

S1.3. Numerical verification and reciprocity floor

To quantify the numerical accuracy with which the symmetry is satisfied, we evaluate the symmetry-forbidden parts of the superconducting free energy and current,

$$\Omega_{\mathrm{SC}}^{\mathrm{odd}}(Q_y) = \frac{\Omega_{\mathrm{SC}}(Q_y) - \Omega_{\mathrm{SC}}(-Q_y)}{2}, \tag{S17}$$

$$K_y^{\mathrm{even}}(Q_y) = \frac{K_y(Q_y) + K_y(-Q_y)}{2}. \tag{S18}$$

Both quantities must vanish in a reciprocal state.

Figure S1 shows that the pristine and P configurations exhibit essentially the same residual symmetry breaking. For the no-exchange calculation, $\max|\Omega_{\mathrm{SC}}^{\mathrm{odd}}| = 8.17 \times 10^{-14}$ eV/cell, while the P state gives 7.82 ×

10^{-14} eV/cell. These values define the numerical reciprocity floor of the finite-Q thermodynamic calculation. The current provides an independent test: the maximum forbidden even component is only 3.27×10^{-5} and 3.15×10^{-5} of the corresponding total current scale for the no-exchange and P states, respectively. Notably, the P-state residual is not larger than the pristine control on either measure.

The residual equilibrium shifts and diode efficiencies are comparably small. As summarized in Table S1, the extracted equilibrium momenta are $Q_{\rm eq} = 1.84 \times 10^{-9}$ and 3.68×10^{-9} Å^{-1} for the no-exchange and P states, respectively, while the corresponding efficiencies are only 6.9×10^{-4}% and 5.3×10^{-4}%. Thus the P-state values are at the same numerical scale as the nominally reciprocal pristine system. This establishes that the apparent residual $Q_{\rm eq}$ and η of the P state are numerical-resolution effects rather than a physically resolved nonreciprocal signal.

S1.4. Layer-odd selection rules and consequences

Equation (S11) gives a general selection rule for the finite-Q_y free energy. At fixed D_+, write the analytic expansion

$$\Omega_{\rm SC}(Q_y, D_-) = \sum_{m,n\geq 0} c_{mn}\, D_-^m Q_y^n. \tag{S19}$$

Applying Eq. (S11) to each monomial gives

$$c_{mn} = (-1)^{m+n} c_{mn}, \tag{S20}$$

and therefore

$$c_{mn} \neq 0 \quad \Longrightarrow \quad m+n \text{ is even}. \tag{S21}$$

This compact rule contains both the P-state reciprocity and the leading layer-parity response. When $D_- = 0$, all odd powers of Q_y vanish, recovering Eq. (S12). When $D_- \neq 0$, terms such as $D_- Q_y$, $D_- Q_y^3$, and $D_-^3 Q_y$ are symmetry allowed.

Equivalently, if the free energy is written as [9]

$$\Omega_{\rm SC}(Q_y, D_-) = \sum_{n\geq 0} \gamma_n(D_-) Q_y^n, \tag{S22}$$

then

$$\gamma_n(D_-) = (-1)^n \gamma_n(-D_-). \tag{S23}$$

With Q_y in Å^{-1}, γ_n has units of energy times length to the power n, per cell. If a fractional-coordinate fit is written as $\Omega = \sum_n \widetilde{\gamma}_n q_2^n$, then $\gamma_n = \widetilde{\gamma}_n/|\mathbf{b}_2|^n$. Thus even-$n$ coefficients are even functions of D_-, whereas odd-n coefficients are odd functions of D_-. In particular,

$$\begin{aligned} \gamma_1(D_-) &= \lambda_1 D_- + \mathcal{O}(D_-^3), \\ \gamma_3(D_-) &= \lambda_3 D_- + \mathcal{O}(D_-^3). \end{aligned} \tag{S24}$$

Keeping the leading terms,

$$\begin{aligned} \Omega_{\rm SC} = \Omega_0 + a_2 Q_y^2 + a_4 Q_y^4 \\ + \lambda_1 D_- Q_y + \lambda_3 D_- Q_y^3 + \cdots . \end{aligned} \tag{S25}$$

Here a_2 and a_4 are the even coefficients at $D_- = 0$. For weak layer asymmetry and a stable central minimum,

$$Q_{\rm eq} \simeq -\frac{\lambda_1 D_-}{2a_2} = -\frac{\lambda_1}{4a_2}\Delta D. \tag{S26}$$

The coefficients here depend on the fixed layer-even exchange D_+. Equivalently, $Q_{\rm eq}(D_+, D_-) = \chi(D_+) D_- + \mathcal{O}(D_-^3)$, with $\chi(D_+) = -\lambda_1(D_+)/[2a_2(D_+)]$; per unit $\Delta D = 2D_-$ the slope is $\chi/2$, i.e., χ_Q of Sec. S4. The textures in Fig. 1(b) of the main text have different D_+, so a common linear law $Q_{\rm eq} = \chi_Q \Delta D_x$ is not required by the fixed-D_+ selection rule alone. Section S4.2 shows numerically that $\chi(D_+)$ is in fact independent of D_+ to a relative 10^{-3} over the in-plane textures considered.

The selection rule also makes clear why the equilibrium helical momentum does not determine the diode efficiency. The coefficient $\lambda_1 D_- Q_y$ controls the leading displacement of the free-energy minimum, whereas the critical-current asymmetry depends on the full nonlinear free-energy landscape and on the termination of the self-consistent superconducting branch near the positive- and negative-Q_y depairing regions. Higher-order odd terms such as $\lambda_3 D_- Q_y^3$ and the pair breaking discussed in Sec. S4.1 can therefore change the magnitude, and even the sign, of the diode response without a comparable change in $Q_{\rm eq}$.

A one-sided configuration has $D_- \neq 0$, whereas the antiparallel configuration $D_t = -D_b$ maximizes $|D_-|$ for fixed $|D_t| = |D_b|$. At fixed D_+, reversal of the layer-odd channel gives, for the corresponding central-minimum branch,

$$Q_{\rm eq}(D_-) = -Q_{\rm eq}(-D_-), \tag{S27}$$

where the fixed D_+ argument is suppressed. Full magnetic reversal instead maps $(D_+, D_-) \to (-D_+, -D_-)$ and relates the two free-energy landscapes by time reversal with $Q_y \to -Q_y$. It therefore reverses the corresponding $Q_{\rm eq}$ and diode polarity. For the AP texture, $D_+ = 0$, these two relations coincide.

S1.5. Symmetry interpretation

The analytical and numerical results lead to three conclusions. First, equal parallel exchange on mirror-equivalent top and bottom Se sublayers is reciprocal by the antiunitary $\sigma_h \mathcal{T}$ symmetry: BdG eigenvalues at $(\mathbf{k}, Q_y)$ are paired with those at $(-\mathbf{k}, -Q_y)$, up to band relabeling. After the Brillouin-zone sum, the self-consistent free energy is even in Q_y and the corresponding thermodynamic current is odd. Figure S1 and Table S1 verify this constraint down to the same numerical

TABLE S1. **Numerical reciprocity controls at $\mu = \mu_0$** (uniform $201 \times 201 +$ third9 mesh, $k_BT = 10^{-5}$ eV). The quantities $\Omega_{\rm SC}^{\rm odd} = [\Omega_{\rm SC}(Q) - \Omega_{\rm SC}(-Q)]/2$ and $K^{\rm even} = [K(Q) + K(-Q)]/2$ vanish for a reciprocal state. The last column normalizes the forbidden even-current component by the maximum magnitude of the physical current on the same finite-Q branch.

State	$Q_{\rm eq}$ (Å^{-1})	η (%)	$\max\lvert\Omega_{\rm SC}^{\rm odd}\rvert$ (eV/cell)	$\max\lvert K^{\rm even}\rvert / \max\lvert K\rvert$
No exchange	$+1.84 \times 10^{-9}$	$+0.0007$	8.17×10^{-14}	3.27×10^{-5}
Parallel (P)	$+3.68 \times 10^{-9}$	$+0.0005$	7.82×10^{-14}	3.15×10^{-5}

floor as pristine $NbSe_2$. Second, the exchange contrast $\Delta D = 2D_-$ parametrizes the symmetry-breaking layer-odd channel. The selection rule in Eq. (S21) requires the leading helical displacement to be odd in ΔD at fixed D_+, giving a leading linear response near a stable central minimum. Third, once $\sigma_h\mathcal{T}$ is broken, symmetry allows both finite pair momentum and nonreciprocal critical currents but does not lock their magnitudes or signs together. The diode efficiency depends on the nonlinear structure of the critical states, which is analyzed in Secs. S4 and S5.

S2. WANNIER–BDG MODEL AND FINITE-Q NUMERICAL FORMULATION

This section documents the microscopic model, superconducting calibration, finite-**Q** Bogoliubov–de Gennes (BdG) construction, branch-selection criteria, and current evaluation used throughout the main text. The purpose is to make clear which ingredients are fixed by the normal-state first-principles model, which ingredients are phenomenological proximity or pairing terms, and how the critical currents are extracted from the self-consistent finite-Q branch.

S2.1. Fully relativistic Wannier Hamiltonian

The normal-state electronic structure is represented by a fully relativistic Wannier Hamiltonian for monolayer 1H-$NbSe_2$. We use the same first-principles and Wannier90 protocol as in our previous work on layer-selective proximity responses in monolayer 1H-NbX_2 [24]. Briefly, the underlying density-functional calculations were performed using QUANTUM ESPRESSO [25, 26], with the PBEsol functional [39] and fully relativistic PAW pseudopotentials [40, 41, 43]; spin–orbit coupling was included self-consistently. The 3×3 charge-density-wave reconstruction observed in low-temperature monolayer $NbSe_2$ [14] was not included. Self-consistent calculations used a $42 \times 42 \times 1$ k mesh, wave-function and charge-density cutoffs of 90 Ry and 720 Ry, respectively, and Marzari–Vanderbilt cold smearing [42] of width 0.01 Ry. The in-plane lattice constant was $a = 3.42$ Å. The spinor Wannierization employed 50 Kohn–Sham bands, 22 spinor Wannier functions, an outer disentanglement window $[-8, 3]$ eV, a frozen window $[-8, 2]$ eV, and a $60 \times 60 \times 1$ uniform Wannierization grid.

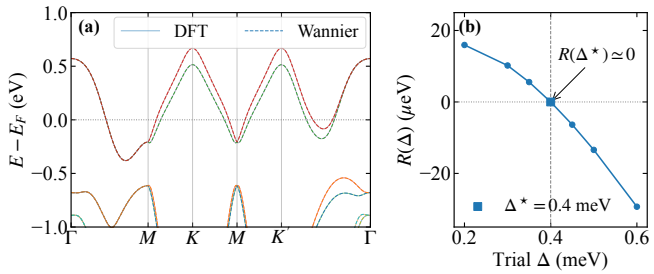


FIG. S2. **Validation and superconducting calibration of the Wannier–BdG model.** (a) Comparison between fully relativistic DFT bands and the 22-state Wannier interpolation along Γ–M–K–M–K'–Γ, with energies shifted by $E_F = \mu_0 = -2.4083$ eV. Within $|E - E_F| \le 1$ eV, the nearest-band RMS deviation is 0.85 meV. (b) Scalar gap-equation residual $R(\Delta) = g_{\rm SC} F_{\rm pair}(\Delta, Q = 0) - \Delta$ for pristine monolayer $NbSe_2$, evaluated on the uniform $201 \times 201 +$ third9 mesh at $k_BT = 10^{-5}$ eV. The calibrated coupling $g_{\rm SC} = 0.500$ eV gives the target pairing amplitude $\Delta^\star = 0.4$ meV with $R(\Delta^\star) = -3.42 \times 10^{-12}$ eV.

Maximally localized spinor Wannier functions (MLWFs) were constructed using WANNIER90 [27, 28, 44, 45], starting from the fully relativistic Bloch states. The Wannier basis consists of five Nb d orbitals and three Se p orbitals on each chalcogen sublayer, giving 11 spatial orbitals and 22 spinor Wannier states. The real-space Hamiltonian is Fourier transformed as

$$H_0(\mathbf{k}) = \sum_{\mathbf{R}} H_0(\mathbf{R}) e^{i\mathbf{k}\cdot\mathbf{R}}, \tag{S28}$$

where $\mathbf{k}$ is a physical wave vector and $\mathbf{R} = \sum_i n_i \mathbf{a}_i$ is a real-space lattice translation, with $n_i \in \mathbb{Z}$. The fractional-coordinate implementation is given in Sec. S2.3. The orbital ordering used in the present calculation is listed in Table S2. Throughout the superconducting calculation, the chemical potential is measured relative to the same Wannier Hamiltonian, with the reference value $\mu_0 = -2.4083$ eV.

Figure S2(a) compares the 22-state Wannier Hamiltonian with the low-energy DFT manifold used in the BdG calculation. After shifting both DFT and Wannier bands by $E_F = \mu_0 = -2.4083$ eV, the nearest-band RMS deviation within $|E - E_F| \le 1$ eV is 0.85 meV. This supports agreement of the interpolated band energies over the displayed window. The nearest-band RMS metric does not, by itself, bound errors in Fermi velocities, eigenvectors,

or sub-meV spin splittings, nor does it fix the detailed filling dependence of the critical currents.

S2.2. Layer-selective magnetic proximity

Magnetic proximity is introduced as a static layer-selective exchange self-energy acting on the Se-derived Wannier spinor blocks,

$$H_{\rm ex} = \sum_{\ell=t,b} P_\ell \, \mathbf{D}_\ell \cdot \boldsymbol{\sigma}, \tag{S29}$$

where P_t and P_b project onto the top and bottom Se p subspaces listed in Table S2. The exchange vector on sublayer ℓ is parameterized as

$$\mathbf{D}_\ell = D_\ell \left(\sin\theta_\ell \cos\phi_\ell, \sin\theta_\ell \sin\phi_\ell, \cos\theta_\ell\right). \tag{S30}$$

The normal-state Hamiltonian entering the BdG calculation is therefore

$$H_e(\mathbf{k}) = H_0(\mathbf{k}) + H_{\rm ex}. \tag{S31}$$

This proximity term should be understood as an effective low-energy exchange self-energy obtained after integrating out the magnetic environment and projecting onto the $NbSe_2$ Wannier subspace. In an explicit magnetic heterostructure, additional terms such as interface electrostatic potentials, spin-dependent hybridization, and modified hoppings can appear. The present model deliberately keeps only the leading local layer-selective exchange so that the layer parity and orientation of the magnetic proximity can be varied in a controlled way.

Unless stated otherwise, the exchange magnitude on each magnetized sublayer is 1 meV. For an ideal pure Wannier spin block the term $\mathbf{D}\cdot\boldsymbol{\sigma}$ has eigenvalues $\pm D$, whereas the shift of an actual low-energy Bloch state is reduced by its Se-layer and orbital weight. We quantified this on the normal-state Fermi contours at μ_0 (36 directions around Γ and around K, $D_b = 1$ meV, exact diagonalization of H_e). The bottom-Se weight of the Fermi-surface states is on average 0.10–0.11 on the Γ pocket and 0.14–0.16 on the K pocket, and reaches 0.20 on parts of the K pocket. Out-of-plane exchange shifts these states at first order: by ± 0.10 meV on the Γ pocket, with the sign of the Ising spin texture, and on average by $+0.13$ and -0.16 meV (at most 0.20 meV) on the two spin-split sheets of the K pocket, i.e., a spin splitting of 0.2–0.3 meV per meV of D_z; a shift of 0.10–0.20 meV is the Zeeman energy $\mu_B B$ of a 1.7–3.5 T field. The largest shift is consistent with the linear closing of the spectral gap, 0.21 meV per meV of D_b (Sec. S4.6). In-plane exchange is quenched by the Ising spin–valley locking: its shifts are of second order and below 0.04 meV. Magnetic-proximity splittings of a few meV are well established in monolayer TMD/magnetic insulator systems, both experimentally and in first-principles calculations [30, 31]. The range used here, $|D_\ell| \le 1.84$ meV, therefore represents weak proximity, and the out-of-plane component is bounded by pair breaking (Sec. S4.2); the magnitudes are not material-specific predictions for a particular $NbSe_2$/magnet interface.

S2.3. Pairing projector and calibration of the superconducting interaction

The superconducting interaction is treated phenomenologically as a local attractive interaction in selected Nb-derived Wannier blocks. In the main calculations the active spatial orbitals are $d_{z^2}, d_{x^2-y^2}$, and d_{xy}, corresponding to spinor block starts 0, 6, and 8 in Table S2; this choice is discussed in Sec. S6.3. The pairing matrix is

$$\hat{\Delta} = \Delta\, \Gamma_{\rm pair}, \qquad \Gamma_{\rm pair} = P_{\rm pair} \otimes i\sigma_y, \tag{S32}$$

where $P_{\rm pair}$ projects onto the three active Nb blocks. The scalar order parameter Δ is taken real; its phase is fixed by a global superconducting gauge choice.

For a trial value of Δ, the anomalous average in the active pairing channel is denoted by

$$F_{\rm pair}(\Delta, Q) = \frac{1}{N_k N_{\rm pair}} \sum_{\mathbf{k}} \sum_{a\in{\rm pair}} \left\langle c_{-\mathbf{k}+\mathbf{Q}/2,a\downarrow} c_{\mathbf{k}+\mathbf{Q}/2,a\uparrow} - c_{-\mathbf{k}+\mathbf{Q}/2,a\uparrow} c_{\mathbf{k}+\mathbf{Q}/2,a\downarrow} \right\rangle /2, \tag{S33}$$

with $N_{\rm pair} = 3$. Equivalently, Eq. (S33) is the projection of the anomalous density matrix onto $\Gamma_{\rm pair}$. The scalar gap equation is

$$\Delta = g_{\rm SC} F_{\rm pair}(\Delta, Q), \tag{S34}$$

where $g_{\rm SC}$ is the effective attractive interaction in the selected pairing channel.

The coupling is calibrated in pristine monolayer $NbSe_2$ at $Q = 0$, $\mu = \mu_0$, and $k_B T = 10^{-5}$ eV by imposing $\Delta_0^\star = 0.4$ meV. The calibration condition is

$$g_{\rm SC} = \frac{\Delta_0^\star}{F_{\rm pair}(\Delta_0^\star, Q = 0)}, \tag{S35}$$

which gives $g_{\rm SC} = 0.500$ eV on the uniform $201 \times 201 +$ third9 mesh. On the production Fermi-surface-adaptive quadrature of Sec. S3.1, the same condition gives $g_{\rm SC} = 0.501$ eV for $L = 2$, 3, and 4 (the three values differ by less than 10^{-4} eV), and the value for the respective L is used for all production results. The imposed $\Delta_0^\star = 0.4$ meV is a phenomenological pairing-amplitude scale, motivated by the superconducting gap $\Delta_{\rm SC} = 0.40 \pm 0.02$ meV measured by scanning tunneling spectroscopy on monolayer $NbSe_2$ on bilayer graphene at 0.34 K [36]. It is not a fit of the minimum quasiparticle excitation gap to an experimental spectral gap. In this multiorbital model, pairing acts only in the selected Nb subspace, so

TABLE S2. **Spinor Wannier basis, pairing projector, and exchange projector.** Each spatial orbital appears as a consecutive two-component spinor block. The main calculations use local spin-singlet pairing only in the active Nb d_{z^2}, $d_{x^2-y^2}$, and d_{xy} blocks, while magnetic proximity exchange is applied only to the top and/or bottom Se p blocks.

Spinor indices	Spatial orbital	Layer	Pairing active?	Exchange projector
0, 1	Nb d_{z^2}	Nb	yes	–
2, 3	Nb d_{xz}	Nb	no	–
4, 5	Nb d_{yz}	Nb	no	–
6, 7	Nb $d_{x^2-y^2}$	Nb	yes	–
8, 9	Nb d_{xy}	Nb	yes	–
10, 11	Se_t p_z	top	no	$\mathbf{D}_t$
12, 13	Se_t p_x	top	no	$\mathbf{D}_t$
14, 15	Se_t p_y	top	no	$\mathbf{D}_t$
16, 17	Se_b p_z	bottom	no	$\mathbf{D}_b$
18, 19	Se_b p_x	bottom	no	$\mathbf{D}_b$
20, 21	Se_b p_y	bottom	no	$\mathbf{D}_b$

the scalar amplitude and the spectral gap generally differ. We define the latter on the sampled Brillouin zone as

$$E_{\mathrm{gap}}(Q) = \min_{n,\mathbf{k}:\, E_{n\mathbf{k}Q}>0} E_{n\mathbf{k}Q}.$$

For the pristine reference calculation at $Q = 0$, $\mu = \mu_0$, and $k_B T = 10^{-5}$ eV on the uniform $201 \times 201 +$ third9 mesh, the recorded values are $\Delta_0^\star = 0.400$ meV and $E_{\mathrm{gap}}(0) = 0.246$ meV; on the production quadrature, $E_{\mathrm{gap}}(0) = 0.237$ meV. This mesh-resolved spectral gap is a separate observable; identifying it with the imposed pairing amplitude would require a different calibration. No such recalibration is made here.

Figure S2(b) shows the residual

$$R(\Delta) = g_{\mathrm{SC}} F_{\mathrm{pair}}(\Delta, Q = 0) - \Delta \tag{S36}$$

on the uniform $201 \times 201 +$ third9 mesh. The residual changes sign through the target value and gives $R(0.4\ \mathrm{meV}) = -3.42 \times 10^{-12}$ eV, corresponding to $|R|/\Delta_0^\star = 8.56 \times 10^{-9}$. After this calibration, g_{SC} is held fixed for all exchange-field, carrier, angular, layer-parity, and temperature calculations; only the gap-magnitude test of Sec. S6.3 uses a different calibration target.

The numerical Wannier interpolation and finite-$\mathbf{Q}$ calculation use fractional reciprocal-lattice coordinates. We define

$$\mathbf{a}_i \cdot \mathbf{b}_j = 2\pi \delta_{ij}, \tag{S37}$$

and distinguish physical wave vectors from dimensionless coordinates:

$$\mathbf{k} = \sum_i \kappa_i \mathbf{b}_i, \qquad \mathbf{Q} = \sum_i q_i \mathbf{b}_i. \tag{S38}$$

For an integer translation vector $\mathbf{n} = (n_1, n_2, n_3)$, let $\mathbf{R}_{\mathbf{n}} = \sum_i n_i \mathbf{a}_i$. The numerical Fourier transform is

$$H_0(\boldsymbol{\kappa}) = \sum_{\mathbf{n}} H_0(\mathbf{R}_{\mathbf{n}}) e^{i 2\pi \mathbf{n}\cdot\boldsymbol{\kappa}}. \tag{S39}$$

Here $H_0(\boldsymbol{\kappa})$ is shorthand for $H_0(\mathbf{k}(\boldsymbol{\kappa}))$.

The lattice vectors in the Wannier Hamiltonian used here are

$$\mathbf{a}_1 = 3.423\,\hat{\mathbf{x}}\ \text{Å},$$
$$\mathbf{a}_2 = (-1.711\,\hat{\mathbf{x}} + 2.964\,\hat{\mathbf{y}})\ \text{Å}.$$

They give

$$\mathbf{b}_1 = (1.836\,\hat{\mathbf{x}} + 1.060\,\hat{\mathbf{y}})\ \text{Å}^{-1},$$
$$\mathbf{b}_2 = 2.120\,\hat{\mathbf{y}}\ \text{Å}^{-1},$$

and $A_{\mathrm{uc}} = 10.144\ \text{Å}^2$. A scan is specified by the angle φ_Q of its direction $\hat{\mathbf{n}}$ from $+\hat{\mathbf{x}}$ and by a scalar fractional parameter q,

$$\mathbf{Q} = Q\,\hat{\mathbf{n}} + Q_\perp \hat{\mathbf{n}}_\perp, \qquad Q = |\mathbf{b}_2|\, q, \tag{S40}$$

with $\hat{\mathbf{n}} = (\cos\varphi_Q, \sin\varphi_Q)$, $\hat{\mathbf{n}}_\perp = \hat{\mathbf{z}} \times \hat{\mathbf{n}}$, and a fixed transverse offset $Q_\perp$ that is zero unless stated otherwise. The fractional components follow from $\mathbf{Q} = \sum_i q_i \mathbf{b}_i$. For $\varphi_Q = 90°$ this is the scan along $\hat{\mathbf{y}} = \hat{\mathbf{b}}_2$, $\mathbf{q} = (0, q, 0)$ and $Q_y = |\mathbf{b}_2| q_2$; $\varphi_Q = 30°$ is the scan along $\mathbf{b}_1$, $\mathbf{q} = (q, 0, 0)$; and $\varphi_Q = 0°$ is the scan along the zigzag direction $\hat{\mathbf{x}}$, for which both fractional components vary. In all cases a stored value of q is multiplied by 2.120 to obtain Q in Å^{-1}, so that the Q spacing and the current conversion below do not depend on the direction. All plotted and quoted momenta in the main text and this Supplemental Material use physical units.

Define the numerical derivative $\mathcal{J} = d\Omega_{\mathrm{SC}}/dq$ along the self-consistent branch. It has units of eV per cell per dimensionless fractional coordinate. The physical sheet current along $\hat{\mathbf{n}}$ is

$$K = \frac{2e}{\hbar A_{\mathrm{uc}}} \frac{d\Omega_{\mathrm{SC}}}{dQ} = \frac{2e}{\hbar A_{\mathrm{uc}} |\mathbf{b}_2|} \mathcal{J}. \tag{S41}$$

With energies and lengths converted to SI, this gives

$$K[\mathrm{A/m}] = 2.264 \times 10^5\, \mathcal{J}[\mathrm{eV/cell}]. \tag{S42}$$

The elementary charge is $e > 0$, and the current polarity follows the phase-gradient convention used in the BdG Hamiltonian. No monolayer thickness is introduced. The common positive current factor leaves the zero crossing in q, the diode efficiency, and relative reciprocity errors unchanged; its physical location is $Q_{\rm eq} = |\mathbf{b}_2| q_{\rm eq}$. The original data headers naming the fractional coordinate (e.g., `Qy_frac`) and the derivative `[arb]` are retained only as file-format conventions, not as physical units. A nonzero $Q_\perp$ is used only for the tilted textures scanned along $\hat{\mathbf{x}}$ (Table S8, block v), where $Q_\perp$ is set to the helical $Q_{\rm eq}$ along $\hat{\mathbf{y}}$ so that the scan line passes through the free-energy minimum, where the transverse current vanishes.

Unless stated otherwise, Brillouin-zone averages use a 201×201 base grid with the shifted "third9" quadrature. Here a shift (s_x, s_y) is specified in units of one base-mesh spacing, and third9 denotes the nine equally weighted meshes

$$(s_x, s_y) \in \left\{0, \frac{1}{3}, \frac{2}{3}\right\} \times \left\{0, \frac{1}{3}, \frac{2}{3}\right\}. \tag{S43}$$

The nine meshes are concatenated before the Brillouin-zone average, giving $N_k = 9 \times 201^2 = 363609$ points. Because the observables are normalized by the total number of points, this is exactly an equal-weight average over the nine shifts; modulo reciprocal-lattice periodicity, the union has the same point spacing as a 603×603 uniform quadrature. The purpose of the shift average is numerical rather than physical: at small thermal energies such as the calibration value $k_B T = 10^{-5}$ eV, Fermi-surface and BdG sums can show appreciable mesh-commensurability (shell) effects when a single grid happens to sample or miss narrow spin-split pockets. The third9 average strongly suppresses this sensitivity without modifying the Hamiltonian or introducing an artificial energy broadening. On top of this base grid, the states near the Fermi level are integrated with the Fermi-surface-adaptive quadrature of Sec. S3.1, which is required to converge the critical currents.

S2.4. Finite-Q BdG Hamiltonian

Following the standard Bogoliubov–de Gennes mean-field construction [32, 46], a superconducting state with center-of-mass momentum $\mathbf{Q}$ [33] pairs electronic states at $\mathbf{k} + \mathbf{Q}/2$ and $-\mathbf{k} + \mathbf{Q}/2$. We use the Nambu spinor

$$\Psi_{\mathbf{kQ}} = \begin{pmatrix} c_{\mathbf{k}+\mathbf{Q}/2} \\ c^\dagger_{-\mathbf{k}+\mathbf{Q}/2} \end{pmatrix}, \tag{S44}$$

where each entry is a 22-component spinor in the Wannier basis. The finite-$\mathbf{Q}$ BdG Hamiltonian is then, with $\mathbf{k}_+ = \mathbf{k} + \mathbf{Q}/2$ and $\mathbf{k}_- = -\mathbf{k} + \mathbf{Q}/2$,

$$H_{\rm BdG}(\mathbf{k}, \mathbf{Q}) = \begin{pmatrix} H_e(\mathbf{k}_+) - \mu & \hat{\Delta} \\ \hat{\Delta}^\dagger & -H_e^*(\mathbf{k}_-) + \mu \end{pmatrix}. \tag{S45}$$

For the present 22-state Wannier model, Eq. (S45) is a 44×44 Hermitian matrix at each $\mathbf{k}$ and $\mathbf{Q}$. The quasiparticle energies and eigenvectors are obtained from

$$H_{\rm BdG}(\mathbf{k}, \mathbf{Q}) |\Phi_{n\mathbf{kQ}}\rangle = E_{n\mathbf{kQ}} |\Phi_{n\mathbf{kQ}}\rangle. \tag{S46}$$

In each calculation, $\mathbf{Q}$ runs along the scan line of Eq. (S40). The formulas of Secs. S2.5 and S2.6 are written for the scans along $\hat{\mathbf{y}}$, $\mathbf{Q} = Q_y \hat{\mathbf{y}}$; for any other direction Q_y and K_y are replaced by Q and K along $\hat{\mathbf{n}}$.

S2.5. Self-consistency workflow and superconducting stability

For each value of Q_y, the calculation proceeds as follows. First, the finite-Q_y BdG Hamiltonian in Eq. (S45) is constructed on the shifted Brillouin-zone mesh defined in Eq. (S43). Second, the anomalous average $F_{\rm pair}(\Delta, Q_y)$ is evaluated from the positive-energy BdG eigenvectors, weighted by $\tanh(\beta E_n/2)$. Particle–hole symmetry maps an eigenstate with energy E at $\mathbf{k}$ onto one with $-E$ at $-\mathbf{k}$ with the same contribution, and the quadrature is symmetric under $\mathbf{k} \to -\mathbf{k}$, so this equals half the sum over all 44 eigenstates, also when Bogoliubov pockets make some energies of the upper half of the spectrum negative. It is therefore consistent with the grand potential below, which sums over all eigenvalues. Third, the scalar gap equation

$$G(\Delta, Q_y) \equiv g_{\rm SC} F_{\rm pair}(\Delta, Q_y) - \Delta = 0 \tag{S47}$$

is solved for the self-consistent value $\Delta^\star(Q_y)$. The scan starts at $Q_y = 0$ and proceeds outward separately along the positive and negative branches. At each point the solver is seeded with the converged value at the neighboring Q_y; a previously converged branch interpolated to that Q_y, when one is supplied, serves only as a fallback seed (Sec. S3.3). It brackets the local positive root near this seed and then refines it within the bracket, by bisection in the uniform-mesh tests and by the Illinois variant of the regula falsi method, which needs fewer evaluations, in all Fermi-surface-adaptive calculations. This continuation procedure helps track a connected branch, but does not by itself guarantee selection of the lowest-grand-potential root when multiple superconducting solutions exist; Sec. S6.5 checks this explicitly.

For clarity, we write the thermodynamic functional in the same normalization used in the code. Define

$$h_e(\mathbf{k}, Q_y) = H_e(\mathbf{k} + \mathbf{Q}/2) - \mu, \tag{S48}$$
$$h_h(\mathbf{k}, Q_y) = H_e(-\mathbf{k} + \mathbf{Q}/2) - \mu. \tag{S49}$$

After diagonalizing the full 44×44 BdG matrix, the quasiparticle and Nambu-trace contribution per primi-

tive cell is

$$F_{\mathrm{BdG}}(Q_y,\Delta) = \frac{1}{N_k}\sum_{\mathbf{k}}\left\{\frac{1}{4}\,\mathrm{Tr}[h_e(\mathbf{k},Q_y)+h_h(\mathbf{k},Q_y)] - \frac{1}{2\beta}\sum_n \ln\left[2\cosh\left(\frac{\beta E_{n\mathbf{k}Q_y}}{2}\right)\right]\right\}, \tag{S50}$$

where $\beta = (k_B T)^{-1}$. The first term is the Nambu trace correction; it removes the double counting introduced by the particle–hole representation. The superconducting grand potential per primitive cell is then

$$\Omega_{\mathrm{SC}}(Q_y,\Delta) = F_{\mathrm{BdG}}(Q_y,\Delta) + N_{\mathrm{pair}}\frac{\Delta^2}{g_{\mathrm{SC}}},\ N_{\mathrm{pair}} = 3, \tag{S51}$$

where the factor N_{pair} is required because the same scalar gap is applied to the three active Nb pairing blocks. The normal-state reference $\Omega_{\mathrm{N}}(Q_y)$ is evaluated with the identical Q_y and k mesh but with $\Delta = 0$. We define

$$\Delta\Omega(Q_y) = \Omega_{\mathrm{SC}}(Q_y,\Delta^\star(Q_y)) - \Omega_{\mathrm{N}}(Q_y). \tag{S52}$$

We use two complementary controls to delimit the finite-Q_y branch on which critical currents are searched. First, a conservative numerical amplitude cutoff is imposed,

$$\Delta^\star(Q_y) > 0.2\,\Delta^\star(0). \tag{S53}$$

This threshold is not a thermodynamic phase boundary; it is a branch-termination safeguard that prevents very small, poorly conditioned residual roots from being interpreted as a robust superconducting state. Second, the comparison with the normal state requires

$$\Delta\Omega(Q_y) < 0, \tag{S54}$$

so that the superconducting solution is lower in grand potential than the normal state. Once $\Delta\Omega > 0$, the normal state is thermodynamically preferred even if the nonlinear gap equation still admits a small nonzero solution. We retain a point on the selected superconducting branch only while both Eqs. (S53) and (S54) are satisfied. Within the scalar-gap ansatz the selected root is moreover a local minimum of $\Omega_{\mathrm{SC}}(\Delta)$. Differentiating Eq. (S51) at fixed $\mathbf{Q}$ gives $\partial\Omega_{\mathrm{SC}}/\partial\Delta = -(2N_{\mathrm{pair}}/g_{\mathrm{SC}})\,G(\Delta)$, so a root at which G changes from positive to negative is a minimum. Because the term $N_{\mathrm{pair}}\Delta^2/g_{\mathrm{SC}}$ dominates at large Δ, $G < 0$ above the largest root, which is therefore always a minimum. At $\mathbf{Q} = 0$ the solver starts from 0.4 meV and selects the root nearest to it; Sec. S6.5 confirms that this is the largest root. Continuation in Q preserves the character of the root until a fold, where $\Delta^\star(Q)$ jumps; such jumps are excluded by the extraction rule of Sec. S2.6. Section S6.5 verifies this directly at the equilibrium and critical momenta of representative states. Stability against spatially varying amplitudes or other pairing channels is outside this ansatz. A small minimum positive BdG quasiparticle energy E_{gap} is recorded as a diagnostic but is not, by itself, used to declare loss of superconductivity, since a gapless superconducting state can still have $\Delta^\star > 0$ and $\Delta\Omega < 0$.

S2.6. Thermodynamic current, critical currents, and diode efficiency

The supercurrent is obtained by differentiating the self-consistent superconducting thermodynamic potential,

$$K_y(Q_y) = \frac{2e}{\hbar A_{\mathrm{uc}}}\frac{d}{dQ_y}\Omega_{\mathrm{SC}}(Q_y,\Delta^\star(Q_y)). \tag{S55}$$

Because $\Delta^\star(Q_y)$ satisfies the stationary condition

$$\left.\frac{\partial\Omega_{\mathrm{SC}}(Q_y,\Delta)}{\partial\Delta}\right|_{\Delta=\Delta^\star(Q_y)} = 0, \tag{S56}$$

the implicit derivative through $\Delta^\star(Q_y)$ does not contribute to Eq. (S55); only the explicit Q_y derivative of the self-consistent free energy is needed.

The equilibrium pair momentum Q_{eq} is obtained from the central zero crossing of $K_y(Q_y)$ associated with the central free-energy minimum on the selected branch. The positive and negative critical currents are defined as

$$K_c^+ = \max_{Q_y\in\mathrm{selected}} K_y(Q_y),\qquad K_c^- = \min_{Q_y\in\mathrm{selected}} K_y(Q_y). \tag{S57}$$

Here "selected" denotes the branch satisfying the criteria in Sec. S2.5, with one further restriction. Near the end of the branch, $\Delta^\star(Q_y)$ can collapse within a few grid points before the criteria of Sec. S2.5 are violated, and a finite-difference derivative taken across the collapse produces an isolated spike in K_y. Starting from $Q_y = 0$ and moving outward, we therefore terminate the search interval at the first abrupt step, defined as $|\Delta^\star(Q_{i+1}) - \Delta^\star(Q_i)| > 0.02\,\Delta^\star(0)$ and more than three times the preceding step, and also discard the last point before it. Branches on which $\Delta^\star$ decreases smoothly are followed to their end, apart from the outermost point, whose derivative is one-sided. The result is insensitive to these choices: for all calculations reported here, thresholds of 0.01, 0.02, and $0.05\,\Delta^\star(0)$ and factors of 2, 3, and 5 give the same η at the quoted precision, and the reported $K_c^\pm$ are interior extrema of the remaining interval (Sec. S3.2). The extrema estimate intrinsic uniform-state depairing currents within the chosen pairing ansatz. Their extraction requires that the extrema be resolved before the numerical branch cutoff; cutoff and grid sensitivity must be assessed in the convergence analysis. They are not a calculation of device switching currents, which

can depend on vortex entry, contacts, and spatial inhomogeneity. The superconducting diode efficiency is

$$\eta = \frac{K_c^+ - |K_c^-|}{K_c^+ + |K_c^-|}. \tag{S58}$$

For diagnostic purposes we also separate the diode numerator and overall critical-current scale,

$$\begin{aligned} K_{\mathrm{diode}} &= K_c^+ + K_c^- = K_c^+ - |K_c^-|, \\ K_{\mathrm{scale}} &= K_c^+ - K_c^- = K_c^+ + |K_c^-|, \end{aligned} \tag{S59}$$

so that $\eta = K_{\mathrm{diode}}/K_{\mathrm{scale}}$. This separation shows whether a change of η comes from the current asymmetry or from the overall current scale.

S3. NUMERICAL CONVERGENCE AND RECIPROCITY CONTROLS

This section quantifies the numerical uncertainty of the finite-Q observables with respect to Brillouin-zone sampling, Q-grid spacing, and the self-consistency criterion, and summarizes the reciprocity floor. Section S3.1 shows that uniform Brillouin-zone meshes do not converge the critical currents, introduces the Fermi-surface-adaptive quadrature used for all diode efficiencies in this work, and establishes its accuracy.

S3.1. Brillouin-zone sampling and Fermi-surface-adaptive quadrature

Uniform meshes. Table S3 lists one-sided in-plane states ($\theta = 90°$, $D_b = 1$ meV) computed on uniform third9 meshes with base sizes $N = 201$ to 601, i.e., 603 to 1803 points per reciprocal-lattice direction. For each N the coupling g_{SC} is recalibrated on the same mesh (Sec. S2.3), so that every mesh describes the same superconductor. The equilibrium momentum is converged on all meshes: Q_{eq} varies by at most 0.05×10^{-6} Å^{-1}. It is set by the linear-in-Q part of the free energy near $Q = 0$, where the spectrum is fully gapped and the Brillouin-zone integrand is smooth. The critical currents are not converged. Between neighboring meshes, η changes by up to a factor of three without a monotonic trend (by an order of magnitude at $\delta\mu = +5$ meV), and at $\delta\mu = +5$ meV even $\Delta^\star(0)$ fluctuates between 0.347 and 0.408 meV.

The origin is the structure of the critical states. In every state the critical momenta lie beyond the momenta at which the quasiparticle gap closes, so the critical states are gapless and contain small Bogoliubov Fermi surfaces. For the converged one-sided state at μ_0, for example, the gap falls below 1 μeV at $Q_y \approx +1.8$ and -2.3×10^{-4} Å^{-1}, whereas $K_c^\pm$ occur at $+2.54$ and -2.88×10^{-4} Å^{-1} ($L = 3$). Near these surfaces the integrand varies on the energy scale $\Delta^\star, k_BT \lesssim 0.4$ meV, whereas a uniform cell spans an energy range $v_F\,\delta k \approx 4$ meV at $N = 601$. The Brillouin-zone sum then depends on how the mesh intersects these surfaces. A direct measure of the resulting error is the normal-state current $K_{\mathrm{N}} = (2e/\hbar A_{\mathrm{uc}})\, d\Omega_{\mathrm{N}}/dQ_y$. It vanishes identically in the continuum limit, because a rigid shift of $\mathbf{k}$ leaves the normal state unchanged, but on the uniform meshes it reaches 2–20 A/m (Table S3). This is comparable to the diode numerator $|K_c^+ + K_c^-| \approx 2$ A/m. Below we quote its effect on the efficiency as the spurious fraction $[K_{\mathrm{N}}(Q_c^+) + K_{\mathrm{N}}(Q_c^-)]/\Delta K$, the part of the current asymmetry $\Delta K = K_c^+ - |K_c^-|$ (= K_{diode} of Sec. S2.6) that comes from the normal-state quadrature error. Brute-force convergence would require several thousand points per direction.

Fermi-surface-adaptive quadrature. We therefore refine the Brillouin-zone quadrature only where the integrand varies rapidly, on the scale k_BT, and becomes non-analytic as $T \to 0$. Let $Q_l[f]$ denote the midpoint rule for an integrand $f(\mathbf{k})$ on the base mesh subdivided l times into $m \times m$ sub-cells (spacing $\delta k/m^l$), and let $S_l(E)$ be a C^∞ window with $S_l = 1$ for $|E| \le W_l/4$, $S_l = 0$ for $|E| \ge W_l$, and $W_l = W/m^{l-1}$. Every Brillouin-zone average in Sec. S2 has the form $f(\mathbf{k}) = \sum_n g(E_n(\mathbf{k}), \psi_n(\mathbf{k}))$ over BdG eigenpairs, and we write $(fS_l)(\mathbf{k}) = \sum_n g\, S_l(|E_n|)$. The integral is evaluated as

$$\begin{aligned} \langle f \rangle &= Q_0[f] + \sum_{l=1}^{L} \Big(Q_l[fS_l] - Q_{l-1}[fS_l] \Big) \\ &= Q_L[fS_L] + \sum_{l=0}^{L-1} Q_l\big[f\,(S_l - S_{l+1})\big], \end{aligned} \tag{S60}$$

with $S_0 \equiv 1$. The second form shows the logic. The rapidly varying part of the integrand near $E = 0$ is integrated on the finest mesh, with spacing $\delta k/m^L$. Each coarser mesh only integrates $f(S_l - S_{l+1})$, which is smooth on that mesh provided the taper of S_{l+1} spans several of its cells; for such integrands the periodic midpoint rule converges faster than any power of the spacing. Each correction in Eq. (S60) is evaluated only on the cells of level $l-1$ that S_l can reach. These are selected from the normal-state bands at $\pm\mathbf{k}$ on a 3×3 stencil per cell, with the band intervals padded by one quarter of their spread and by an additional 1 meV. The correction weights sum to zero, so the normalization of every average is unchanged. Inside a refined cell, $\mathcal{H}(\mathbf{k})$ is obtained from a Taylor expansion about the cell center, constructed once and independent of $\mathbf{Q}$. The expansion order is chosen such that $\max|\mathcal{H}_{\mathrm{Taylor}} - \mathcal{H}| < 10^{-9}$ eV over the cell and $|Q|/2 \le 5 \times 10^{-4}$ in fractional units (fifth order at $N = 201$, error 7×10^{-11} eV).

Two limits make the scheme testable. For $W \to \infty$ and odd m, Eq. (S60) reduces exactly to the uniform mesh with spacing $\delta k/m^L$; we verified this to a relative 10^{-14} for $L = 1$ and 2. For finite W, the only additional error is the quadrature of the smooth remainder on the coarser meshes. We measured it directly at $N = 201$, $L = 1$, and $m = 3$, where the refined points coincide

with the uniform $N = 603$ mesh, at fixed (Q_y, Δ) pairs bracketing the critical region. The error decreases rapidly with the ratio of W to the energy spread ϵ_c of a Fermi-surface cell ($\epsilon_c = 11.8$ meV at $N = 201$, 90th percentile). The relative error of the pairing kernel [Eq. (S33)] is 3×10^{-7}, 2×10^{-8}, and 3×10^{-9} for $W/\epsilon_c = 4$, 6, and 8. The corresponding error of the nonreciprocal free-energy difference $\Omega(Q_y) - \Omega(-Q_y)$ is 1.1×10^{-2}, 1.8×10^{-3}, and 3×10^{-4} at the near-critical pair $(Q_y, \Delta) = (\pm 3.2 \times 10^{-4}$ Å$^{-1}, 0.25$ meV). For comparison, the uniform $N = 201$ mesh differs from $N = 603$ by a relative 0.17 in the same quantity. We use $m = 3$ and $W = 72$ meV $\approx 6\epsilon_c$.

Convergence and production protocol. With the adaptive quadrature the diode efficiency converges (Fig. S3 and Table S3). At μ_0 and $k_BT = 5 \times 10^{-5}$ eV, $L = 2$ on base meshes $N = 201$ and 233 gives $\eta = -0.95\%$ and -0.96%, and $L = 3$ gives -0.93%. The critical currents agree to 0.3 A/m, $\Delta^\star(0)$ to 10^{-4} meV, and the recalibrated couplings to 10^{-4} ($g_{\rm SC} = 0.500676$, 0.500716, and 0.500721 eV). The spurious current $K_{\rm N}$ drops to 0.9, 0.2, and 0.1 A/m. At $\mu_0 + 5$ meV, $L = 2$ and $L = 3$ give $\eta = -0.93\%$ to within 0.01 percentage points, and the large fluctuations of $\Delta^\star(0)$ on the uniform meshes disappear. The $L = 3$ values, $\eta(\mu_0) = -0.93\%$ and $\eta(\mu_0 + 5$ meV$) = -0.93\%$ at $k_BT = 5 \times 10^{-5}$ eV, differ from every $L = 2$ result by at most 0.09 percentage points, and by at most 0.03 when the current is taken from $d\Omega_{\rm SC}/dQ_y$ as in the rest of this work. The uniform-mesh results scatter around these values by up to ± 0.9 percentage points. In particular, the apparent near-cancellation of η at $\delta\mu = +5$ meV on uniform meshes is a sampling artifact: the converged efficiencies at μ_0 and $\mu_0 + 5$ meV are equal within their uncertainty.

Unless stated otherwise, diode efficiencies for in-plane and tilted exchange are therefore computed on the $N = 201$ third9 base mesh with $m = 3$, $L = 2$, and $W = 72$ meV, with $g_{\rm SC}$ calibrated on the same quadrature, at $k_BT = 5 \times 10^{-5}$ eV and $dq = 4 \times 10^{-6}$ (or 2×10^{-6} where noted). Doubling the Q spacing from 2×10^{-6} changes η by at most 0.02 percentage points. From the comparison above, the accuracy of this protocol is ± 0.1 percentage points in η and ± 0.3 A/m in $K_c^\pm$. Purely out-of-plane exchange produces critical states that are closer to gapless, and $L = 2$ is not sufficient there; those states are computed with $L = 3$ unless marked, and checked against $L = 4$ at $D_z = 1$ meV (Sec. S4.6). One gap-equation evaluation takes 14 s on 128 cores (4.9 million points in total), compared with 5 s for the uniform $N = 601$ mesh and 50 s for $L = 3$. The production temperature corresponds to $T \approx 0.58$ K, about $0.3\,T_c$ for the model $T_c \approx 1.9$ K estimated from $\Delta^\star(T)$ (Sec. S6.2). At $k_BT = 10^{-5}$ eV the in-plane state was computed only with $L = 2$, which gives $\eta = -1.18\%$; an $L = 3$ comparison was not made at this temperature, but the convergence diagnostics are as good as for the production states (Sec. S6.2).

S3.2. Q-grid resolution and critical-current extraction

Table S4 tests the Q spacing on the production quadrature. The coarser grids are taken from the same runs. The full-precision current is integrated to $\Omega_{\rm SC}(Q_y)$, which is then differentiated by central differences using every second or fourth point. The test therefore covers both the finite-difference error in K_y and the sampling of the extrema. Going from $dq = 2 \times 10^{-6}$ to the production value 4×10^{-6} ($\delta Q_y = 4.2$ and 8.5×10^{-6} Å^{-1}) changes $K_c^\pm$ by at most 0.13 A/m and η by at most 0.02 percentage points. $Q_{\rm eq}$ does not change at the quoted precision. Doubling the spacing again, to $dq = 8 \times 10^{-6}$, shifts η by up to 0.08 percentage points (AP). The production spacing is therefore well within the ± 0.1-percentage-point accuracy of the quadrature (Sec. S3.1). The same subsampling applied to the out-of-plane states at $L = 3$ of Table S8 (not tabulated) changes η by at most 0.06 percentage points when the spacing is doubled ($D_b = 1$ meV, $-1.447\% \to -1.389\%$), including the cusp at $k_BT = 10^{-5}$ eV ($-3.372\% \to -3.406\%$). For an error that scales as a power ≥ 1 of the spacing, the error at the production spacing is at most this change, also at the cusp, where the extremum-sampling error is linear rather than quadratic in the spacing. The production values are thus accurate to better than 0.06 percentage points, within the ± 0.1-percentage-point accuracy of the quadrature.

The extraction rule of Sec. S2.6 matters only where $\Delta^\star(Q_y)$ collapses abruptly at the end of a branch. There, a finite-difference derivative across the collapse produces an isolated spike in K_y, and a naive extremum search can return it as a critical current. On uniform meshes this happened, for example, for the AP state at $dq = 5 \times 10^{-7}$, where it gave $K_c^- = -136.2$ A/m instead of the interior extremum. On the production quadrature, all reported $K_c^\pm$ are interior extrema. Varying the collapse threshold between 0.01 and $0.05\,\Delta^\star(0)$ and the abruptness factor between 2 and 5 leaves every η in this work unchanged at the quoted precision.

S3.3. Self-consistency criterion and seeding

The gap equation, Eq. (S47), is solved to an absolute residual $|G| < \epsilon$ with $\epsilon = 10^{-8}$ eV in production. At each Q_y, the solver starts from the converged value at the neighboring Q_y. When an earlier branch is available, its value interpolated to that Q_y is used as a fallback seed. The tolerance test of Table S5 was performed on the uniform $N = 201$ third9 mesh at $k_BT = 10^{-5}$ eV. The residual criterion acts on the gap equation at each Q_y and does not depend on how the Brillouin-zone sum is evaluated, so its conclusion carries over to the production quadrature. Tightening ϵ to 10^{-9} and 10^{-10} eV changes $\Delta^\star(0)$ by at most 10^{-4} meV, $Q_{\rm eq}$ by at most

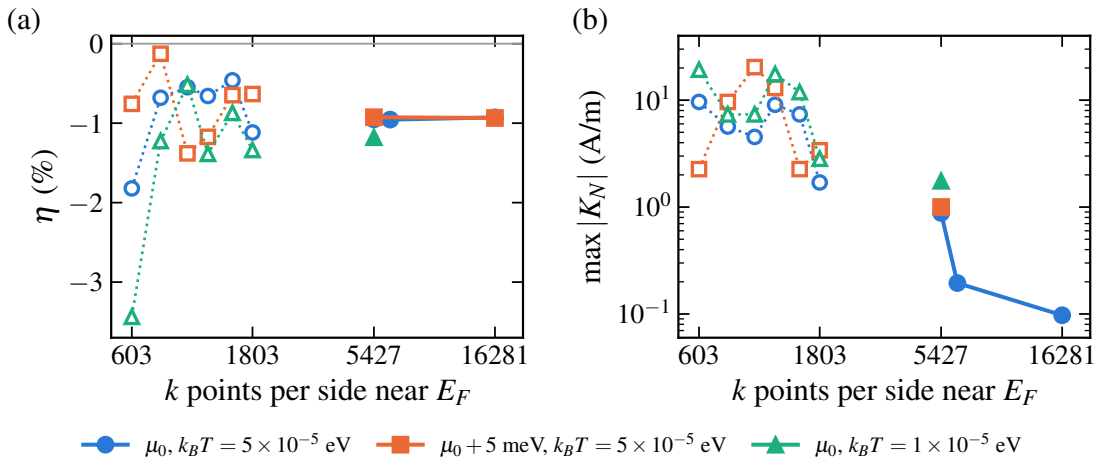


FIG. S3. **Brillouin-zone convergence of the diode efficiency.** (a) η and (b) maximum spurious normal-state current $|K_{\mathrm{N}}|$ versus the number of k points per reciprocal-lattice direction near E_F, for one-sided in-plane exchange. Open symbols: uniform third9 meshes, $N = 201$–601 ($3N$ points per direction). Filled symbols: Fermi-surface-adaptive quadrature [Eq. (S60)] with $m = 3$ on base meshes $N = 201$ ($L = 2$: 5427; $L = 3$: 16281) and $N = 233$ ($L = 2$: 6291). The $L = 2$ quadrature resolves the Fermi surface three times more finely than the largest uniform mesh (5427 versus 1803 points per direction) with about 1.5 times as many k points in total. Values are listed in Table S3.

0.01×10^{-6} Å^{-1}, $K_c^{\pm}$ by less than 0.01 A/m, and η by less than 0.01 percentage points. The production criterion is therefore not a limiting source of error.

S3.4. Numerical reciprocity floor

The reciprocity floor is established in Sec. S1.3 with the no-exchange and P states: $\max|\Omega_{\mathrm{SC}}^{\mathrm{odd}}| \approx 8 \times 10^{-14}$ eV/cell, $\max|K^{\mathrm{even}}|/\max|K| \approx 3 \times 10^{-5}$, and $|\eta| < 10^{-3}\%$. On the production quadrature, the out-of-plane one-sided state scanned along $\hat{\mathbf{y}}$, which is reciprocal by $M_x\mathcal{T}$ (Sec. S4.1), gives $|Q_{\mathrm{eq}}| < 0.01 \times 10^{-6}$ Å^{-1} and $|\eta| = 0.003\%$ (Table S6). Symmetry checks compare states computed on the same quadrature. They bound numerical symmetry breaking but not the quadrature error of Sec. S3.1, which affects symmetry-related partners identically.

S4. HELICAL RESPONSE AND LAYER PARITY: COMPLETE RESULTS

This section collects the $\mu = \mu_0$ calculations behind the helical magnetoelectric response and the layer-parity control of the main text. All states use the production quadrature of Sec. S3.1 ($N = 201$, third9, $m = 3$, $L = 2$, $W = 72$ meV; $L = 3$ for the out-of-plane states of Sec. S4.6 unless marked, and in addition for the tilted textures with $D_z > 1$ meV), $k_BT = 5 \times 10^{-5}$ eV, $dq = 4 \times 10^{-6}$ (or 2×10^{-6} where noted), and g_{SC} calibrated on the same quadrature (Sec. S2.3). The observables are listed in Table S6 and summarized in Fig. S4.

To place one-sided, two-sided, and tilted textures on a common footing, we use the x component of the top–bottom exchange contrast,

$$\Delta D_x \equiv D_{b,x} - D_{t,x}, \qquad D_{\ell,x} = D_\ell \sin\theta_\ell \cos\phi_\ell, \quad \text{(S61)}$$

and the out-of-plane component $D_z = D_b \cos\theta$ of the one-sided textures. For the collinear in-plane textures, ΔD_x reduces to $\Delta D = D_b - D_t = 2D_-$ [Eq. (S4)].

All states scanned along $\hat{\mathbf{y}}$ fall on a single line [Fig. S4(a)],

$$Q_{\mathrm{eq}} \simeq \chi_Q \, \Delta D_x, \qquad \chi_Q = -17.81 \times 10^{-6} \text{ Å}^{-1}\,\text{meV}^{-1}, \quad \text{(S62)}$$

where χ_Q is a least-squares fit through the origin over the states of Fig. S4(a); including the four further tilted states of Sec. S4.1 changes it by 0.09×10^{-6} Å^{-1} meV^{-1}. The deviation is below 0.09×10^{-6} Å^{-1} for all in-plane textures and reaches 0.34 and 0.53×10^{-6} Å^{-1} for the tilted states with $\theta = 45°$ and $D_b = 1.5$ and 1.75 meV. The collapse holds, to this accuracy, irrespective of the layer-even exchange D_+ and of the out-of-plane component. The diode efficiency behaves differently. For in-plane textures it is also a function of ΔD_x alone, and is linear in it [Fig. 1(c) of the main text]. An out-of-plane component, which leaves Q_{eq} nearly unchanged, strongly suppresses it and, for $D_z \gtrsim 1.1$ meV and at low temperature (Sec. S6.2), reverses its sign. The following subsections document the individual scans.

TABLE S3. **Brillouin-zone convergence for one-sided in-plane exchange ($\theta = 90°$, $D_b = 1$ meV).** N is the base mesh (third9); N_F is the number of k points per reciprocal-lattice direction in the energy window around E_F ($3N$ for uniform meshes and $3N \cdot 3^L$ for the Fermi-surface-adaptive quadrature). g_{SC} is recalibrated for every quadrature. $\Delta^\star(0)$ is in meV, Q_{eq} in 10^{-6} Å^{-1}, $K_c^\pm$ and K_N in A/m. $K_c^\pm$ are obtained from $d\Omega_{SC}/dQ_y$ with the rule of Sec. S2.6; FS-refined runs use $dq = 2\times10^{-6}$ ($L = 2$) and 4×10^{-6} ($L = 3$).

State	Quadrature	N	N_F	$\Delta^\star(0)$	Q_{eq}	K_c^+	K_c^-	η (%)	max $\lvert K_N\rvert$
μ_0, $k_BT = 5\times10^{-5}$ eV	uniform	201	603	0.3985	−17.83	96.96	−100.56	−1.82	9.6
	uniform	261	783	0.3985	−17.87	96.47	−97.79	−0.68	5.7
	uniform	333	999	0.3985	−17.86	99.14	−100.23	−0.55	4.5
	uniform	401	1203	0.3984	−17.86	94.33	−95.58	−0.66	9.1
	uniform	501	1503	0.3985	−17.88	95.38	−96.27	−0.46	7.4
	uniform	601	1803	0.3984	−17.85	95.75	−97.91	−1.12	1.7
	FS, $L = 2$	201	5427	0.3985	−17.86	95.64	−97.48	−0.95	0.88
	FS, $L = 2$	233	6291	0.3985	−17.85	95.88	−97.73	−0.96	0.19
	FS, $L = 3$	201	16281	0.3985	−17.86	95.95	−97.75	−0.93	0.10
$\mu_0 + 5$ meV, $k_BT = 5\times10^{-5}$ eV	uniform	201	603	0.3542	−17.82	80.68	−81.91	−0.76	2.3
	uniform	261	783	0.3999	−17.86	100.99	−101.24	−0.13	9.6
	uniform	333	999	0.4079	−17.81	93.66	−96.28	−1.38	20.4
	uniform	401	1203	0.3470	−17.82	82.34	−84.29	−1.17	13.0
	uniform	501	1503	0.3569	−17.84	80.30	−81.35	−0.65	2.3
	uniform	601	1803	0.3689	−17.84	85.89	−86.98	−0.63	3.4
	FS, $L = 2$	201	5427	0.3671	−17.83	85.18	−86.77	−0.93	1.0
	FS, $L = 3$	201	16281	0.3677	−17.83	84.93[a]	−86.53[a]	−0.93[a]	–
μ_0, $k_BT = 10^{-5}$ eV	uniform	201	603	0.3997	−17.87	118.55	−126.99	−3.44	19.2
	uniform	261	783	0.3999	−17.87	116.62	−119.51	−1.23	7.4
	uniform	333	999	0.3998	−17.87	124.66	−125.95	−0.52	7.4
	uniform	401	1203	0.3999	−17.87	114.92	−118.15	−1.39	17.5
	uniform	501	1503	0.3998	−17.87	115.96	−118.00	−0.87	11.9
	uniform	601	1803	0.3998	−17.87	119.20	−122.44	−1.34	2.8
	FS, $L = 2$	201	5427	0.3998	−17.87	117.24	−120.04	−1.18	1.8

[a] From $d(\Omega_{SC} - \Omega_N)/dQ_y$. For the other converged runs this definition and $d\Omega_{SC}/dQ_y$ agree to within 0.07 percentage points in η; at $L = 3$ (μ_0) they agree to 0.002.

TABLE S4. **Q-grid convergence on the production quadrature** ($N = 201$, third9, $m = 3$, $L = 2$, $k_BT = 5\times10^{-5}$ eV unless noted). dq is the fractional spacing, and the first row of each block is the native grid of the run. Units as in Table S3.

State	dq	Q_{eq}	K_c^+	K_c^-	η (%)
One-sided, μ_0	2×10^{-6}	−17.86	95.64	−97.48	−0.952
	4×10^{-6}	−17.86	95.51	−97.39	−0.974
	8×10^{-6}	−17.86	95.25	−97.13	−0.976
One-sided,	2×10^{-6}	−17.83	85.18	−86.77	−0.925
$\delta\mu = +5$ meV	4×10^{-6}	−17.84	85.08	−86.65	−0.918
	8×10^{-6}	−17.84	84.70	−86.22	−0.891
One-sided,	2×10^{-6}	−17.87	117.24	−120.04	−1.176
$k_BT = 10^{-5}$ eV	4×10^{-6}	−17.87	117.20	−119.99	−1.178
	8×10^{-6}	−17.87	117.00	−119.87	−1.211
AP, μ_0	4×10^{-6}	−35.71	94.18	−97.82	−1.895
	8×10^{-6}	−35.71	93.65	−97.43	−1.977
	1.6×10^{-5}	−35.71	92.63	−96.37	−1.980

TABLE S5. **Self-consistency criterion** (uniform $N = 201$ third9 mesh, $dq = 10^{-6}$, $k_BT = 10^{-5}$ eV). ϵ is the absolute residual tolerance of the gap equation; units as in Table S3. The one-sided rows were computed with an earlier version of the one-sided exchange Hamiltonian file, which had a shorter hopping range, and therefore differ from the uniform $N = 201$ row of Table S3; all other results in this work use the full Hamiltonian. Only the dependence on ϵ is tested here.

State	ϵ (eV)	$\Delta^\star(0)$	Q_{eq}	K_c^+	K_c^-	η (%)
One-sided, μ_0	10^{-8}	0.3951	−17.88	117.36	−125.41	−3.32
	10^{-9}	0.3951	−17.88	117.36	−125.41	−3.32
	10^{-10}	0.3951	−17.88	117.36	−125.41	−3.32
One-sided,	10^{-8}	0.3521	−17.85	108.24	−108.02	+0.10
$\delta\mu = +5$ meV	10^{-9}	0.3520	−17.85	108.24	−108.02	+0.10
	10^{-10}	0.3520	−17.86	108.24	−108.02	+0.10
AP, μ_0	10^{-8}	0.4000	−35.73	116.85	−130.27	−5.43
	10^{-9}	0.4000	−35.73	116.85	−130.27	−5.43

S4.1. Polar angle and the out-of-plane limit

For one-sided bottom-layer exchange with $D_b = 1$ meV and $\phi = 0°$, the ratio $Q_{eq}/\sin\theta$ is −17.65, −17.75, −17.82, and -17.86×10^{-6} Å^{-1} for $\theta = 30°$, 45°, 60°, and 90° (Table S6, block i). It is constant to within 0.21×10^{-6} Å^{-1}, and the small reduction at small θ comes from the mixed terms discussed below. The helical displacement is thus controlled by the in-plane component

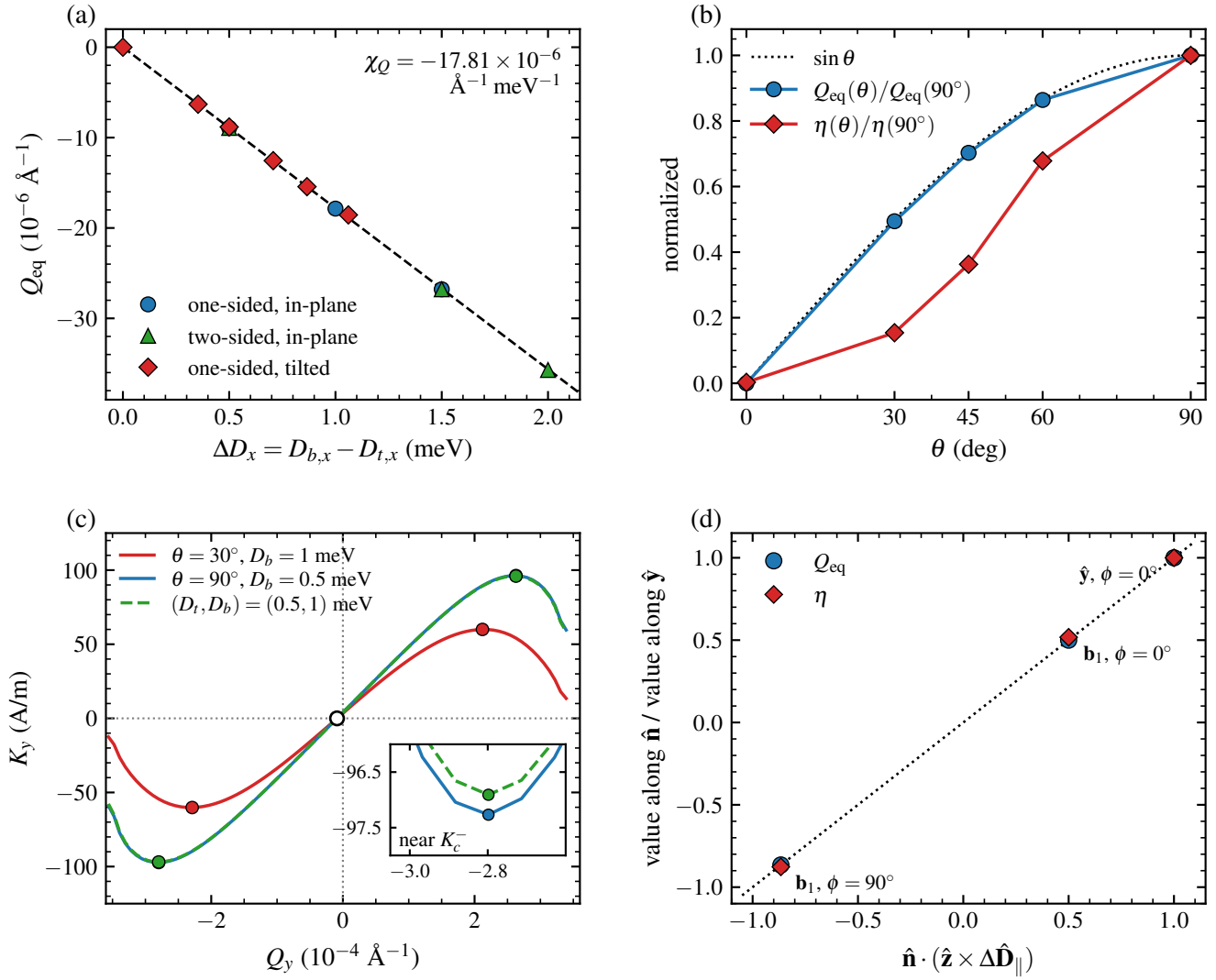


FIG. S4. **Helical momentum and diode efficiency at** $\mu = \mu_0$ (production quadrature, $k_BT = 5 \times 10^{-5}$ eV). (a) Q_{eq} versus ΔD_x [Eq. (S61)] for the following states scanned along $\hat{\mathbf{y}}$ (Table S6): one-sided in-plane (D_b = 0.5, 1, 1.5 meV), two-sided in-plane ((D_t, D_b) = (0.5, 1), (−0.5, 1), and AP), and one-sided tilted (θ = 0°–60° at D_b = 1 meV, and θ = 45° at 0.5 and 1.5 meV). The dashed line is Eq. (S62). (b) $Q_{eq}(\theta)/Q_{eq}(90°)$ and $\eta(\theta)/\eta(90°)$ for the one-sided polar-angle scan at D_b = 1 meV, $\phi = 0°$. The dotted curve is $\sin\theta$. (c) Sheet current $K_y(Q_y)$ for three states with $Q_{eq} \simeq -8.9 \times 10^{-6}$ Å^{-1}. The two in-plane states, which differ only in D_+, are indistinguishable on this scale; the inset enlarges the region near K_c^-. Filled circles mark $K_c^{\pm}$, and the open circle marks the common zero crossing. (d) Vector form of the helical response. Q_{eq} and η along a scan direction $\hat{\mathbf{n}}$, normalized to the values for $\hat{\mathbf{n}} = \hat{\mathbf{y}}$ and $\phi = 0°$, versus the projection $\hat{\mathbf{n}} \cdot (\hat{\mathbf{z}} \times \Delta\hat{\mathbf{D}}_{\parallel})$. The dotted line is the projection law. Momenta are in 10^{-6} Å^{-1} in (a) and 10^{-4} Å^{-1} in (c).

$D_b \sin\theta$ [Fig. S4(b)].

The out-of-plane limit is reciprocal along $\hat{\mathbf{y}}$ by symmetry. Besides σ_h, the $1H$ structure with $\mathbf{a}_1 \parallel \hat{\mathbf{x}}$ has the vertical mirror

$$M_x: \quad (x, y, z) \to (-x, y, z), \tag{S63}$$

which maps each Se sublayer onto itself. An axial vector transforms as $(D_x, D_y, D_z) \to (D_x, -D_y, -D_z)$ under M_x. Combining this with time reversal gives

$$M_x\mathcal{T}: \quad (D_{\ell,x}, D_{\ell,y}, D_{\ell,z}) \to (-D_{\ell,x}, D_{\ell,y}, D_{\ell,z}),$$
$$(Q_x, Q_y) \to (Q_x, -Q_y). \tag{S64}$$

Any texture with $D_{t,x} = D_{b,x} = 0$ is therefore invariant under $M_x\mathcal{T}$ and satisfies $\Omega_{SC}(Q_y) = \Omega_{SC}(-Q_y)$ along $\hat{\mathbf{y}}$, for arbitrary y and z exchange components on the two layers. Only the x components can generate nonreciprocity along $\hat{\mathbf{y}}$. Together with the $\sigma_h\mathcal{T}$ rule of Sec. S1.4, the only term linear in both Q_y and the exchange field

TABLE S6. **Finite-Q observables at $\mu = \mu_0$** (production quadrature, $k_BT = 5 \times 10^{-5}$ eV). Exchange magnitudes D_t and D_b are in meV. For the two-sided textures ($\theta = 90°$, $\phi = 0°$), D_t and D_b are signed x components, so that a negative value denotes $\mathbf{D}_\ell \parallel -\hat{\mathbf{x}}$. The column "$\mathbf{Q} \parallel$" gives the scan direction; $\mathbf{b}_1$ lies at 30° to $\hat{\mathbf{x}}$, and for these rows $Q_{\rm eq}$ is the component along the scan. ΔD_x [Eq. (S61)] is in meV, $Q_{\rm eq}$ in 10^{-6} Å^{-1}, $K_c^{\pm}$ in A/m, and $\Delta^\star(0)$ in meV. Entries marked "sym." are fixed by symmetry and were not recomputed on the production quadrature (Secs. S1 and S4.1). Rows marked ($L = 3$) use the three-level quadrature, all others $L = 2$. † $dq = 2 \times 10^{-6}$; all other rows $dq = 4 \times 10^{-6}$.

State	D_t	D_b	θ	ϕ	$\mathbf{Q} \parallel$	ΔD_x	$Q_{\rm eq}$	K_c^+	K_c^-	η (%)	$\Delta^\star(0)$
(i) One-sided, polar angle											
Bottom only	0	1	0°	0°	$\hat{\mathbf{y}}$	0	0.00	49.35	−49.35	−0.003	0.385
Bottom only	0	1	30°	0°	$\hat{\mathbf{y}}$	0.50	−8.82	60.00	−60.17	−0.147	0.390
Bottom only	0	1	45°	0°	$\hat{\mathbf{y}}$	0.71	−12.55	71.29	−71.78	−0.346	0.394
Bottom only	0	1	60°	0°	$\hat{\mathbf{y}}$	0.87	−15.43	83.14	−84.22	−0.646	0.397
Bottom only†	0	1	90°	0°	$\hat{\mathbf{y}}$	1.00	−17.86	95.64	−97.48	−0.952	0.398
($L = 3$)	0	1	90°	0°	$\hat{\mathbf{y}}$	1.00	−17.86	95.95	−97.75	−0.927	0.398
(ii) One-sided, exchange strength											
Bottom only	0	0.5	90°	0°	$\hat{\mathbf{y}}$	0.50	−8.93	96.33	−97.27	−0.483	0.399
Bottom only	0	1.5	90°	0°	$\hat{\mathbf{y}}$	1.50	−26.78	94.60	−97.37	−1.442	0.398
Bottom only	0	0.5	45°	0°	$\hat{\mathbf{y}}$	0.35	−6.31	90.02	−90.60	−0.319	0.398
Bottom only	0	1.5	45°	0°	$\hat{\mathbf{y}}$	1.06	−18.53	43.83	−43.88	−0.061	0.381
($L = 3$)	0	1.5	45°	0°	$\hat{\mathbf{y}}$	1.06	−18.55	44.01	−44.04	−0.034	0.381
Bottom only	0	1.75	45°	0°	$\hat{\mathbf{y}}$	1.24	−21.47	28.30	−28.13	+0.309	0.366
($L = 3$)	0	1.75	45°	0°	$\hat{\mathbf{y}}$	1.24	−21.51	28.44	−28.24	+0.354	0.366
Bottom only	0	1.5	30°	0°	$\hat{\mathbf{y}}$	0.75	−13.05	23.05	−22.92	+0.289	0.359
($L = 3$)	0	1.5	30°	0°	$\hat{\mathbf{y}}$	0.75	−13.07	23.17	−23.02	+0.330	0.359
Bottom only ($L = 3$)	0	1.84	45°	0°	$\hat{\mathbf{y}}$	1.30	−22.67	22.74	−22.46	+0.615	0.358
Bottom only	0	1.414	60°	0°	$\hat{\mathbf{y}}$	1.22	−21.73	70.76	−71.62	−0.605	0.394
(iii) Two-sided, in-plane ($\mathbf{D}_\ell \parallel \pm\hat{\mathbf{x}}$)											
P	1	1	90°	0°	$\hat{\mathbf{y}}$	0	sym.	–	–	0 (sym.)	–
Two-sided	0.5	1	90°	0°	$\hat{\mathbf{y}}$	0.50	−8.93	95.97	−96.91	−0.488	0.398
Two-sided	−0.5	1	90°	0°	$\hat{\mathbf{y}}$	1.50	−26.78	94.94	−97.72	−1.441	0.399
AP	−1	1	90°	0°	$\hat{\mathbf{y}}$	2.00	−35.71	94.18	−97.82	−1.895	0.398
(iv) Direction of $\mathbf{Q}$											
Bottom only	0	1	90°	90°	$\hat{\mathbf{y}}$	0	sym.	–	–	0 (sym.)	–
Bottom only	0	1	90°	0°	$\mathbf{b}_1$	1.00	−8.93	95.81	−96.75	−0.493	0.398
Bottom only	0	1	90°	90°	$\mathbf{b}_1$	0	+15.45	97.20	−95.59	+0.835	0.398

is $Q_y \Delta D_x$, and Eq. (S62) is the corresponding leading response. Mixed terms such as $Q_y \Delta D_x D_z^2$ are allowed at higher order. They account for the reduction of $Q_{\rm eq}/\Delta D_x$ by up to 0.5×10^{-6} Å^{-1} meV^{-1} in the tilted states. On the production quadrature, the out-of-plane state gives $|Q_{\rm eq}| < 0.01 \times 10^{-6}$ Å^{-1} and $\eta = -0.003\%$ along $\hat{\mathbf{y}}$, which sets the numerical floor for this symmetry class (Sec. S3.4). Equation (S64) leaves the $\hat{\mathbf{x}}$ direction unconstrained; the out-of-plane state is nonreciprocal along $\hat{\mathbf{x}}$ (Sec. S4.6).

The efficiency does not follow $\sin\theta$ [Fig. S4(b)]. For $\theta = 60°$, 45°, and 30°, η is 0.78, 0.51, and 0.31 times the in-plane value at the same ΔD_x, $\eta_\parallel(\Delta D_x) = -0.955\% \times \Delta D_x$/meV (Sec. S4.2). At $\theta = 45°$, the ratio is 0.94 for $D_b = 0.5$ meV and drops to 0.03 for $D_b = 1.5$ meV. The latter state, computed with $L = 3$ because its efficiency is small, has $Q_{\rm eq} = -18.55 \times 10^{-6}$ Å^{-1}, nearly the same as the one-sided in-plane state with $D_b = 1$ meV (-17.86×10^{-6} Å^{-1}), but an efficiency 27 times smaller (−0.034% against −0.927%, both at $L = 3$). With $L = 2$ the values are −0.061% and −0.952%, a factor of 16. The suppression thus exceeds an order of magnitude at both refinement levels, but its precise factor depends on the convergence of this small residual efficiency, which changes from −0.061% to −0.034% between $L = 2$ and $L = 3$ and was not computed at $L = 4$. For this state the spurious fraction is 0.014, and the efficiency from $d(\Omega_{\rm SC} - \Omega_{\rm N})/dQ$ is −0.035%. The suppression is controlled by D_z [Fig. 1(d) of the main text]. The out-of-plane exchange is not protected by Ising spin–valley locking and is pair breaking. It reduces the mean critical current $\bar{K}_c = (K_c^+ + |K_c^-|)/2$ to 0.94, 0.87, 0.74, 0.62, and 0.46 of the in-plane value for $D_z = 0.35$, 0.5, 0.71, 0.87, and 1.06 meV. The current asymmetry $K_c^+ - |K_c^-|$ is reduced even more strongly, to 0.89, 0.68, 0.38, 0.19, and 0.015 (0.027 with $L = 2$) of its in-plane value at the same ΔD_x; for the last state $\Delta K = -0.030$ A/m (−0.053 A/m with $L = 2$), against −1.96 A/m from the in-plane slope of Sec. S4.2. The suppression follows the closing of the spectral gap at the equilibrium momentum: $E_{\rm gap}(Q_{\rm eq}) = 0.163$, 0.131, 0.088, 0.055, and 0.007 meV for the same states, against 0.209 meV for the in-plane state with $D_b = 1$ meV and 0.2365 meV for the AP$_z$

texture, whose exchange has no measurable effect on the condensate (Sec. S4.6). The values at $D_z = 0.5$, 0.71, and 0.87 meV are computed directly at $\mathbf{Q} = Q_{\rm eq}\hat{\mathbf{y}}$ (Table S8, block v); the others, here and below, are obtained by linear interpolation of $E_{\rm gap}(Q)$ on the Q grid, which underestimates the cusp maximum at $Q_{\rm eq}$ by up to a few μeV.

At larger D_z the efficiency changes sign. The tilted states with $\theta = 45°$, $D_b = 1.75$ meV ($D_z = 1.24$ meV) and $\theta = 30°$, $D_b = 1.5$ meV ($D_z = 1.30$ meV), computed with $L = 3$, give $\eta = +0.354\%$ and $+0.330\%$ ($+0.309\%$ and $+0.289\%$ with $L = 2$), i.e., -0.30 and -0.46 times $\eta_\parallel(\Delta D_x)$; $d(\Omega_{\rm SC} - \Omega_{\rm N})/dQ$ gives $+0.360\%$ and $+0.337\%$. Their current asymmetry, $K_c^+ - |K_c^-| = +0.20$ and $+0.15$ A/m, is -0.087 and -0.110 (-0.076 and -0.096 with $L = 2$) times its in-plane value at the same ΔD_x. Linear interpolation of this ratio between the two states with $\theta = 45°$ and $D_b = 1.5$ and 1.75 meV puts the zero at $D_z \approx 1.09$ meV (1.11 meV with $L = 2$). Both states are gapless along the whole branch, $\bar{K}_c$ drops to 0.29 and 0.24 of the in-plane value, and the selected solution is the global minimum at the tested momenta (Sec. S6.5); the temperature dependence of the reversal is given in Sec. S6.2. Their helical momenta, $Q_{\rm eq} = -21.51$ and -13.07×10^{-6} Å^{-1}, nevertheless remain within 0.53×10^{-6} Å^{-1} of Eq. (S62).

The suppression and the reversal are set by D_z alone. Two further states repeat the D_z of earlier ones with a different in-plane component (Table S6, block ii). The state with $\theta = 60°$ and $D_b = 1.414$ meV ($D_z = 0.71$ meV, $\Delta D_x = 1.22$ meV, $L = 2$) gives $\eta = -0.605\%$. Its ratios to the in-plane values, $\eta/\eta_\parallel = 0.517$ and $\bar{K}_c/\bar{K}_{c\parallel} = 0.738$, agree with 0.512 and 0.742 for $\theta = 45°$, $D_b = 1$ meV ($D_z = 0.71$ meV, $\Delta D_x = 0.71$ meV), and so does the interpolated $E_{\rm gap}(Q_{\rm eq})$, 0.086 against 0.087 meV. The state with $\theta = 45°$ and $D_b = 1.84$ meV ($D_z = 1.30$ meV, $\Delta D_x = 1.30$ meV, $L = 3$) gives $\eta = +0.615\%$, with ratios -0.495 and 0.234 against -0.461 and 0.240 for $\theta = 30°$, $D_b = 1.5$ meV ($\Delta D_x = 0.75$ meV); its current asymmetry is -0.115 times the in-plane value, against -0.110, and it is gapless along the whole branch. With ΔD_x changed by a factor of 1.7 at fixed D_z, the ratios thus differ by at most 0.04, and the curves of Fig. 1(d) of the main text are functions of D_z. The helical momenta, -21.73 and -22.67×10^{-6} Å^{-1}, lie 0.08 and 0.50×10^{-6} Å^{-1} from Eq. (S62).

Pocket-resolved current asymmetry. The following decomposition locates the asymmetry $K_c^+ - |K_c^-|$ of the in-plane state with $D_b = 1$ meV and of the tilted states with $\theta = 45°$, $D_b = 1.5$ and 1.75 meV, and $\theta = 30°$, $D_b = 1.5$ meV, all at $L = 3$. Because $\partial\Omega_{\rm SC}/\partial\Delta = 0$ at self-consistency, the sheet current can be evaluated at fixed $\Delta^\star(Q)$ and split term by term. The current decomposed here is taken from $d(\Omega_{\rm SC} - \Omega_{\rm N})/dQ$, which removes the normal-state quadrature error $K_{\rm N}$ (Sec. S3.1); for these states it changes $K_c^+ - |K_c^-|$ from that of Eq. (S41) by at most 0.01 A/m. For each signed eigenvalue E_n in the upper half of the BdG spectrum, the free-energy term $-\beta^{-1}\ln[2\cosh(\beta E_n/2)]$, with $\beta = 1/k_BT$, splits as

$$-\frac{E_n}{2} - \beta^{-1}\ln\left(1 + e^{-\beta E_n}\right). \tag{S65}$$

The second term gives the quasiparticle back-flow $K^{\rm qp}$, carried by thermally excited quasiparticles and by the occupied states of Bogoliubov pockets ($E_n < 0$). The remainder, including the pairing term and the normal-state reference, is the condensate part $K^{\rm c} = K - K^{\rm qp}$. The current density is also resolved on the base $\mathbf{k}$ mesh, with the refined cells folded onto their base cell, and summed over the regions nearest to Γ and to K or K'. Only the sum over K and K' is meaningful, because the Nambu spinor at $\mathbf{k}$ contains the electron at $\mathbf{k}+\mathbf{Q}/2$ and the hole at $-\mathbf{k}+\mathbf{Q}/2$.

The critical momenta lie at slightly different distances from $Q_{\rm eq}$: $+272.2$ and -270.4×10^{-6} Å^{-1} in-plane, and $+196.6$ and -193.4×10^{-6} Å^{-1} for $\theta = 45°$, $D_b = 1.5$ meV. The total current is flat there, but its two parts are not; each changes by about 0.46 A/m per 10^{-6} Å^{-1}, with opposite signs. The parts are therefore compared at the mirrored momenta $Q_{\rm eq} \pm f s_c$, where s_c is the mean critical distance and $\Delta^\star$ is interpolated from the scan:

$$A_X(f) = X(Q_{\rm eq}+fs_c) + X(Q_{\rm eq}-fs_c) - 2X(Q_{\rm eq}). \tag{S66}$$

Subtracting $2X(Q_{\rm eq})$ removes the equilibrium counterflow between the pockets. At $Q_{\rm eq}$, where $K = 0$, the Γ pocket carries $+1.02$ A/m in-plane ($+1.10$ A/m for $\theta = 45°$, $D_b = 1.5$ meV), and the K and K' pockets carry the opposite current. For the total current, $X = K$, we write $A_{\rm tot} \equiv A_K$; at $f = 1$ it equals $K_c^+ - |K_c^-|$ up to the offset of the critical momenta: -1.79 A/m against $\Delta K = -1.79$ A/m in-plane, -0.008 A/m against $\Delta K = -0.031$ A/m for $\theta = 45°$, $D_b = 1.5$ meV, and $+0.205$ and $+0.152$ A/m against $+0.204$ and $+0.155$ A/m in the two sign-reversed states. All differences are small compared with the pocket contributions below.

Table S7 lists the decomposition at $f = 1$, and Fig. S5 shows its dependence on f. In all four states the condensate part drops out, because it is odd in $Q - Q_{\rm eq}$ along the branch: $|A_{\rm c}| < 4 \times 10^{-3}$ A/m at every f in the first two states of Table S7 and ≤ 0.01 A/m in the other two. In the first two states it has the same slope, 0.46 A/m per 10^{-6} Å^{-1}. The asymmetry is therefore carried by quasiparticle back-flow, and it builds up close to the critical momenta: in-plane, $A_{\rm tot} = -0.02$, -0.13, -0.57, and -1.79 A/m for $f = 0.25$, 0.5, 0.75, and 1. In the in-plane state it comes from the Γ pocket (-1.90 A/m), with a small contribution of opposite sign from the K and K' pockets ($+0.10$ A/m). Effective models restricted to the K and K' pockets [12, 13] therefore do not capture the dominant contribution in this setting. In the tilted state with $\theta = 45°$ and $D_b = 1.5$ meV, the back-flow of the Γ pocket changes little, and its asymmetry decreases in magnitude to -1.40 A/m. The back-flow in

the K and K' pockets, in contrast, doubles: the out-of-plane exchange depairs these pockets. Its asymmetry keeps the sign opposite to that of the Γ pocket and grows to +1.39 A/m, which cancels the Γ contribution to within 0.01 A/m. The same back-flow lowers $\bar{K}_c$: with an unchanged condensate slope, the larger back-flow makes the current peak at a smaller $|Q-Q_{\rm eq}|$. The suppression of η in this state is therefore a compensation between the two pocket families, not a removal of the helical asymmetry.

At larger D_z the balance tips [Fig. S5(d)]. The back-flow in the K and K' pockets no longer grows: it is 30–33 A/m on each side in all three tilted states. Per meV of ΔD_x, its asymmetry decreases only slightly, from +1.31 A/m at $D_z = 1.06$ meV to +1.25 and +1.15 A/m at $D_z = 1.24$ and 1.30 meV. The asymmetry of the Γ pocket per meV of ΔD_x keeps decreasing in magnitude, from −1.90 A/m in-plane to −1.32, −1.09, and −0.95 A/m. The K and K' pockets therefore dominate, and $A_{\rm tot} = +0.21$ and +0.15 A/m for $D_z = 1.24$ and 1.30 meV, the sign of the reversed efficiency.

S4.2. Exchange strength and the layer-even exchange

Table S6, blocks ii and iii, contains two pairs of in-plane states with the same ΔD_x but different layer-even exchange D_+: one-sided $D_b = 0.5$ meV against $(D_t, D_b) = (0.5, 1)$ meV ($\Delta D_x = 0.5$ meV), and one-sided $D_b = 1.5$ meV against $(D_t, D_b) = (-0.5, 1)$ meV ($\Delta D_x = 1.5$ meV). Within each pair, $Q_{\rm eq}$ agrees to 0.01×10^{-6} Å^{-1}, $K_c^{\pm}$ to 0.4 A/m, and η to 0.005 percentage points (−0.483% against −0.488%, and −1.442% against −1.441%). The current curves of the first pair cannot be distinguished on the scale of Fig. S4(c). For in-plane exchange, both observables therefore depend on $\Delta D_x = 2D_-$ alone; the layer-even exchange D_+, up to $|D_+| = 0.75$ meV, has no measurable effect.

Both observables are also linear in ΔD_x. Over the six in-plane states, $0.5 \le \Delta D_x \le 2$ meV, $Q_{\rm eq}/\Delta D_x$ lies between −17.86 and -17.85×10^{-6} Å^{-1} meV^{-1}, and $\eta/\Delta D_x$ between −0.95 and −0.98% per meV; a fit through the origin gives $\eta_\parallel = -0.955\% \times \Delta D_x/\text{meV}$. The current asymmetry $K_c^+ - |K_c^-| = -1.85 \pm 0.03$ A/m per meV of ΔD_x is equally linear, while $\bar{K}_c = 96.4 \pm 0.4$ A/m does not depend on the exchange. In-plane exchange is weakly pair breaking because of Ising spin–valley locking, so that the critical-current scale is that of the no-exchange superconductor; the AP$_z$ texture, whose exchange has no measurable effect on the condensate (Sec. S4.6), gives $\bar{K}_c = 97.1$ A/m along $\hat{\mathbf{x}}$. The spectral gap at $Q_{\rm eq}$ falls only from 0.2365 meV (AP$_z$) to 0.209 and 0.156 meV for one-sided in-plane exchange $D_b = 1$ and 1.5 meV.

Out-of-plane exchange, in contrast, is strongly pair breaking. At $\theta = 0°$, $D_b = 1$ meV reduces $\bar{K}_c$ to 49.0 A/m ($L = 3$) and reduces the spectral gap to 27 μeV at $Q = 0$. At $D_b = 1.5$ meV, the state is gapless at all Q, and its condensation energy is 0.04 times that at $D_b = 1$ meV. The normal state is then already a local minimum of $\Omega_{\rm SC}(\Delta)$, but the superconducting solution lies below it at every Q of the branch and is the global minimum at the tested momenta (Sec. S6.5). The one-sided scans are therefore restricted to $D_z \le 1.5$ meV and, except for the tilted states with $D_b = 1.75$ and 1.84 meV of Sec. S4.1, to $D_b \le 1.5$ meV, i.e., $\Delta D_x \le 1.5$ meV; the two-sided textures extend the in-plane contrast to 2 meV.

S4.3. Parallel, antiparallel, and single-layer textures

The P state is reciprocal by $\sigma_h\mathcal{T}$ (Sec. S1). On the uniform mesh, the independently computed P state satisfied this to within the no-exchange floor (Sec. S1.3). It was not recomputed on the production quadrature. The AP state has the largest contrast, $\Delta D_x = 2$ meV, and gives $Q_{\rm eq} = -35.71 \times 10^{-6}$ Å^{-1} and $\eta = -1.895\%$, twice the one-sided values (−17.86 and −0.952%). At a common spacing $dq = 4 \times 10^{-6}$, the ratio $\eta_{\rm AP}/\eta_{\text{one-sided}}$ is 2.06, 1.95, and 2.01 at $\delta\mu = -5$, 0, and +5 meV (Sec. S5).

The horizontal mirror maps a top-layer exchange $D_{t,x}$ onto a bottom-layer exchange $-D_{b,x}$ [Eq. (S2)]. Top-only exchange along $+\hat{\mathbf{x}}$ is therefore symmetry-equivalent to bottom-only exchange along $-\hat{\mathbf{x}}$, and both have $\Delta D_x = -1$ meV. Time reversal maps $(\mathbf{D}_t, \mathbf{D}_b, Q_y)$ to $(-\mathbf{D}_t, -\mathbf{D}_b, -Q_y)$ and therefore requires

$$K_y(Q_y; \mathbf{D}_t, \mathbf{D}_b) = -K_y(-Q_y; -\mathbf{D}_t, -\mathbf{D}_b). \tag{S67}$$

These textures thus have $Q_{\rm eq} = +17.86$ and $+35.71 \times 10^{-6}$ Å^{-1} and $\eta = +0.952\%$ and +1.895%, with $K_c^{\pm}$ interchanged. On the uniform mesh, the corresponding independent calculations reproduced Eq. (S67) to within 0.01 A/m between the critical momenta.

S4.4. Vector form of the helical response

The layer-preserving subgroup of D_{3h} contains C_3 and the vertical mirrors. Under this subgroup, the only invariant that couples the polar in-plane vector $\mathbf{Q}_\parallel$ to the in-plane axial exchange contrast $\Delta\mathbf{D}_\parallel = \mathbf{D}_{b,\parallel} - \mathbf{D}_{t,\parallel}$ at linear order is $\mathbf{Q}_\parallel \cdot (\hat{\mathbf{z}} \times \Delta\mathbf{D}_\parallel)$. The scalar $\mathbf{Q}_\parallel \cdot \Delta\mathbf{D}_\parallel$ is odd under M_x. The C_3 symmetry also makes the quadratic superfluid stiffness isotropic at zeroth order in the exchange. The equilibrium momentum is therefore

$$\mathbf{Q}_{\rm eq} \simeq \chi_Q\, \hat{\mathbf{z}} \times \Delta\mathbf{D}_\parallel, \tag{S68}$$

which reduces to Eq. (S62) for $\Delta\mathbf{D}_\parallel \parallel \hat{\mathbf{x}}$. The helical momentum is perpendicular to the exchange contrast and rotates rigidly with it.

Table S6, block iv, tests Eq. (S68) with scans along $\mathbf{b}_1$. For an isotropic quadratic term, the minimum along a line through the origin with direction $\hat{\mathbf{n}}$ lies at $\mathbf{Q}_{\rm eq} \cdot \hat{\mathbf{n}}$.

TABLE S7. **Pocket-resolved helical current asymmetry** at the mirrored momenta $Q_{\rm eq} \pm s_c$ [$f = 1$ in Eq. (S66); $L = 3$, $k_BT = 5 \times 10^{-5}$ eV, scans along $\hat{\mathbf{y}}$]. s_c in 10^{-6} Å^{-1}, $E_{\rm gap}(Q_{\rm eq})$ in meV, and currents in A/m. $A_{\rm tot} = A_{\rm c} + A_{\rm qp} = A_\Gamma + A_{K+K'}$ up to rounding. The last two columns give the back-flow of each pocket family at $Q_{\rm eq} + s_c$ and $Q_{\rm eq} - s_c$.

State	s_c	$E_{\rm gap}(Q_{\rm eq})$	$A_{\rm tot}$	$A_{\rm c}$	A_Γ	$A_{K+K'}$	$K^{\rm qp}_\Gamma$	$K^{\rm qp}_{K+K'}$
In-plane, $D_b = 1$ meV	271.3	0.209	−1.79	0.00	−1.90	+0.10	−13.5, +11.6	−15.2, +15.3
$\theta = 45°$, $D_b = 1.5$ meV	195.0	0.007	−0.008	0.00	−1.40	+1.39	−14.1, +12.6	−31.7, +32.8
$\theta = 45°$, $D_b = 1.75$ meV	156.9	0	+0.205	0.01	−1.34	+1.55	−12.6, +10.9	−31.4, +32.7
$\theta = 30°$, $D_b = 1.5$ meV	139.9	0	+0.152	0.01	−0.71	+0.86	−11.1, +10.1	−30.2, +31.0

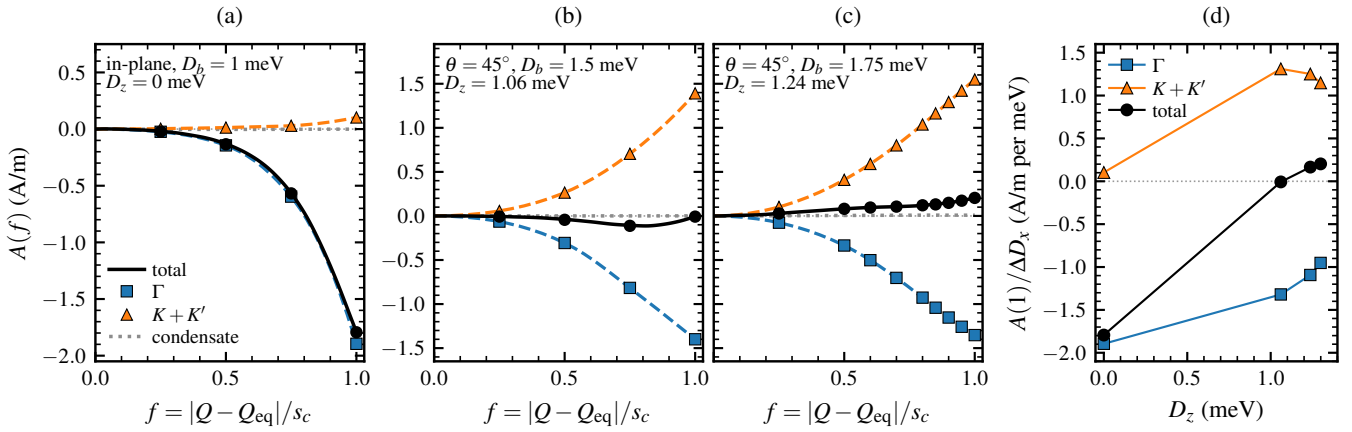


FIG. S5. **Pocket-resolved helical current asymmetry** ($L = 3$, $k_BT = 5 \times 10^{-5}$ eV, scans along $\hat{\mathbf{y}}$). (a)–(c) Mirrored asymmetry $A_X(f)$ [Eq. (S66)] for (a) the in-plane state with $D_b = 1$ meV and the tilted states with $\theta = 45°$ and (b) $D_b = 1.5$ meV and (c) $D_b = 1.75$ meV: total current (solid line, from the scan; circles, from the decomposition), quasiparticle back-flow in the Γ (squares) and $K + K'$ (triangles) regions, and condensate part (dotted). Dashed lines are monotone interpolations in f^2, a guide to the eye. (d) The pocket contributions and the total at $f = 1$ per meV of ΔD_x versus D_z for the four states of Table S7.

Equation (S68) then predicts $-17.86 \sin 30° = -8.93$ and $+17.86 \cos 30° = +15.47$ (in 10^{-6} Å^{-1}) for $\phi = 0°$ and 90°. The computed values are −8.93 and +15.45. The diode efficiency follows the same projection law closely: $\eta = -0.493\%$ and $+0.835\%$, against -0.476% and $+0.825\%$ from projecting the $\hat{\mathbf{y}}$ value [Fig. S4(d)]. To a good approximation, the in-plane efficiency along $\hat{\mathbf{n}}$ is thus proportional to $\hat{\mathbf{n}} \cdot (\hat{\mathbf{z}} \times \Delta\mathbf{D}_\parallel)$. The ratios of computed to projected values (1.036 and 1.012) are partly a Q-grid effect: the $\mathbf{b}_1$ scans use $dq = 4 \times 10^{-6}$, and projecting the $\hat{\mathbf{y}}$ value at the same spacing (-0.974%, Table S4) gives -0.487% and $+0.844\%$, and ratios of 1.012 and 0.990. An anisotropy of the depairing regions, allowed by C_3 at higher order in Q, is therefore at most at this level.

S4.5. Summary of the helical channel

For in-plane exchange, the helical momentum and the diode efficiency are both linear responses to the single parameter $\Delta\mathbf{D}_\parallel = 2\mathbf{D}_{-,\parallel}$. Both are governed by $\hat{\mathbf{z}} \times \Delta\mathbf{D}_\parallel$ (the momentum as a vector, the efficiency through its projection on the scan direction), and both are independent of the layer-even exchange. The out-of-plane exchange separates them. It leaves $\mathbf{Q}_{\rm eq}$ on the in-plane line to within 0.53×10^{-6} Å^{-1} but, through pair breaking, suppresses η by more than an order of magnitude (a factor of 27 at $L = 3$ and 16 at $L = 2$ for $\theta = 45°$, $D_b = 1.5$ meV) and, at low temperature (Sec. S6.2), reverses it for $D_z \gtrsim 1.1$ meV: the depaired K and K' pockets carry a back-flow asymmetry that compensates or, at larger D_z, exceeds the one carried by the Γ pocket (Sec. S4.1). A finite helical momentum is therefore not a quantitative proxy for the rectification. The symmetry relations of the model (σ_h, $\mathcal{T}$, $\sigma_h\mathcal{T}$, and $M_x\mathcal{T}$) are reproduced at the level of the numerical floor.

S4.6. Out-of-plane exchange: nonreciprocity along $\hat{\mathbf{x}}$

For purely out-of-plane exchange, $D_{\ell,x} = D_{\ell,y} = 0$, the magnetic point group of a one-sided texture is $3m'$. It contains C_3 and the three vertical mirrors combined with time reversal, $\sigma_v\mathcal{T}$, but not σ_h or C_2'. The operation $M_x\mathcal{T}$ maps $(Q_x, Q_y) \to (Q_x, -Q_y)$ [Eq. (S64)]. A linear term $\mathbf{Q} \cdot \mathbf{v}$ in $\Omega_{\rm SC}$ is therefore allowed only for $\mathbf{v} \parallel \hat{\mathbf{x}}$, and C_3 then forces $\mathbf{v} = 0$. The point $\mathbf{Q} = 0$ is therefore

stationary for any D_z. Symmetry alone does not exclude finite-$\mathbf{Q}$ minima that break C_3. C_3 does, however, make the quadratic term isotropic, so a positive curvature along one direction makes $\mathbf{Q}=0$ a local minimum in the whole $\mathbf{Q}$ plane. The computed free energy is lowest at $\mathbf{Q}=0$ over the whole superconducting branch in every purely out-of-plane scan (Table S8, blocks i–iv, and the out-of-plane rows of Table S10). These form a collection of scans rather than a full parameter grid: along $\varphi_Q=0°$ for one- and two-sided textures with $D_b=0.25$–1.5 meV (for $D_b=1$ meV also at $k_BT=10^{-5}$ and 10^{-4} eV, and for $D_b=1$ and 1.5 meV also with the larger gap of Sec. S6.3), and along $\varphi_Q=10°$, $20°$, and $90°$ for $D_b=1$ meV at $k_BT=5\times10^{-5}$ eV. Since $\Omega_{\rm SC}(\mathbf{Q})$ is invariant under C_3 and under $M_x\mathcal{T}$, which maps φ_Q to $-\varphi_Q$, the half-lines φ_Q and $\varphi_Q+180°$ of these four scans cover the inequivalent wedge $0°\le\varphi_Q\le60°$ in $10°$ steps for $D_b=1$ meV. We therefore take

$$\mathbf{Q}_{\rm eq}=0. \tag{S69}$$

The lowest odd invariant is cubic,

$$\Omega_{\rm SC}^{\rm odd}(\mathbf{Q})\propto D_z\,(Q_x^3-3Q_xQ_y^2)=D_z\,|\mathbf{Q}|^3\cos3\varphi_Q, \tag{S70}$$

where φ_Q is measured from $\hat{\mathbf{x}}$, the normal of the mirror M_x. All odd invariants up to order $|\mathbf{Q}|^7$ share the $\cos3\varphi_Q$ dependence. The diode efficiency along $\hat{\mathbf{n}}$ is then expected to vary as $\cos3\varphi_Q$. It vanishes exactly along the mirror lines ($\varphi_Q=30°,90°,\ldots$), which includes the $\hat{\mathbf{y}}$ scans of Sec. S4.1, and $\eta(60°)=-\eta(0°)$ and $\eta(45°)=-\eta(15°)$ by symmetry. The horizontal mirror keeps D_z and exchanges the layers. A two-sided out-of-plane texture is therefore σ_h-symmetric when parallel and $\sigma_h\mathcal{T}$-symmetric (reciprocal) when antiparallel. This channel is controlled by the layer-even exchange $D_{+,z}$, opposite to the helical channel, which is controlled by $D_{-,x}$.

Converged result. For $D_b=1$ meV, $\theta=0°$, scanned along $\hat{\mathbf{x}}$ ($\varphi_Q=0°$), the three-level refinement ($L=3$) gives $Q_{\rm eq}=0.05\times10^{-6}$ Å^{-1}, which is zero within the Q grid, together with $K_c^+=48.26$ A/m, $K_c^-=-49.68$ A/m, and $\eta=-1.447\%$. The definition through $d(\Omega_{\rm SC}-\Omega_{\rm N})/dQ$ gives -1.437%, and the spurious fraction is 0.01. A four-level refinement ($L=4$, $g_{\rm SC}$ recalibrated on the same quadrature) gives $K_c^+=48.26$ A/m, $K_c^-=-49.68$ A/m, and $\eta=-1.452\%$ (-1.445% from $d(\Omega_{\rm SC}-\Omega_{\rm N})/dQ$); at common Q points the currents of the two refinements agree to a relative 10^{-4}. The value is therefore converged to within 0.01 percentage points. For this symmetry class, the $L=2$ quadrature is not sufficient. It gives $\eta=-1.668\%$ from $d\Omega_{\rm SC}/dQ$ and -1.107% from $d(\Omega_{\rm SC}-\Omega_{\rm N})/dQ$, and its spurious fraction is 0.23–0.84 for all out-of-plane scans along $\hat{\mathbf{x}}$ with $D_z\le1$ meV (not tabulated; it shows up as the difference between η and $\eta_{\Delta\Omega}$ in Table S8), compared with at most 0.07 for the in-plane states. For $D_b=1.5$ meV, whose critical momenta are three times smaller (Table S11), the spurious fraction is only 0.01. The normal-state quadrature error has the same $3m'$ symmetry as the physical effect, so the angular dependence alone cannot separate the two. The $L=2$ angular ratios are therefore only a symmetry check; the quantitative test of the angular dependence uses $L=3$ (below).

Why the efficiency exceeds the in-plane value. The out-of-plane state has a larger efficiency than the one-sided in-plane state of the same strength (-1.447% against -0.927%, both at $L=3$), although its helical momentum vanishes. Two facts explain this. First, $Q_{\rm eq}$ is set by the linear coefficient of $\Omega_{\rm SC}(Q)$, Eq. (4) of the main text, whereas η is set by the odd part of $\Omega_{\rm SC}$ about its minimum, which first enters at cubic order. C_3 forbids the former but allows the latter, Eq. (S70). Second, writing $\eta=\Delta K/(2\bar{K}_c)$, the two states have comparable current asymmetries, $\Delta K=-1.42$ and -1.80 A/m, but very different current scales, $\bar{K}_c=48.97$ and 96.85 A/m. The ratio of efficiencies, $1.56=(1.42/1.80)\times(96.85/48.97)$, comes from the current scale. In-plane exchange is ineffective against Ising-locked pairs, whereas out-of-plane exchange acts as a Zeeman field along the Ising axis. It reduces the spectral gap at $\mathbf{Q}=0$ to 27 μeV (from 0.24 meV) and halves the critical current.

Microscopically, the out-of-plane exchange adds to the Ising spin splitting in one valley and subtracts from it in the other. The Fermi pockets at K and K' are trigonally warped with opposite orientations. In the time-reversal-symmetric state their odd contributions to $\Omega_{\rm SC}$ cancel. The exchange-induced valley imbalance leaves a net term with the $\cos3\varphi_Q$ form of Eq. (S70), but no net displacement of the condensate, since each pocket is C_3 symmetric about its valley. This is the mechanism of magnetochiral anisotropy in gated MoS_2 and of the out-of-plane-field diode effect in few-layer $NbSe_2$ [5, 6, 17], and a cubic term of this form has been invoked for the field-free diode effect of $NbSe_2/CrBr_3$ heterostructures [21]. The same exchange also acts on the helical (in-plane) diode effect of tilted textures (Sec. S4.1). Along $\hat{\mathbf{y}}$ it contributes no asymmetry on its own, by $M_x\mathcal{T}$, but it depairs the K and K' pockets. Their back-flow then carries an asymmetry of opposite sign to that of the Γ pocket and compensates or, for $D_z\gtrsim1.1$ meV and at low temperature, exceeds it.

Layer parity. The horizontal mirror extends the selection rule of Sec. S1.4 to arbitrary collinear textures. With $D_{\pm,i}=(D_{b,i}\pm D_{t,i})/2$ for each Cartesian component i, Eq. (S2) and time reversal give

$$\begin{aligned}\sigma_h\mathcal{T}:\quad &(D_{+,\parallel},D_{-,\parallel},D_{+,z},D_{-,z})\\ &\to(D_{+,\parallel},-D_{-,\parallel},-D_{+,z},D_{-,z}),\quad \mathbf{Q}\to-\mathbf{Q}.\end{aligned} \tag{S71}$$

$\Omega_{\rm SC}(\mathbf{Q})$ can therefore be odd in $\mathbf{Q}$ only through the layer-odd in-plane exchange $D_{-,\parallel}$, which drives the helical channel (Secs. S4.1–S4.5), and the layer-even out-of-plane exchange $D_{+,z}$, which drives the trigonal channel. The components $D_{+,\parallel}$ and $D_{-,z}$ cannot rectify on their own.

Table S8, block ii, tests this for the out-of-plane channel. The parallel textures $D_t=D_b=0.25$ and 0.5 meV

have the same $D_{+,z}$ as the one-sided textures $D_b = 0.5$ and 1 meV, but no $D_{-,z}$. They reproduce the one-sided states: over the whole branch, $\Delta^\star(Q_x)$ and $K_x(Q_x)$ agree to a relative 3×10^{-5}, and η to 0.001 percentage points. The antiparallel texture $D_t = -D_b = -1$ meV has $D_{+,z} = 0$ and $D_{-,z} = 1$ meV. It is reciprocal, $K_c^+ = |K_c^-| = 97.07$ A/m and $|\eta| < 10^{-3}\%$, as Eq. (S71) requires. Its $\Delta^\star(0) = 0.399$ meV and $E_{\rm gap}(0) = 0.2365$ meV agree with the no-exchange values calibrated at $k_BT = 10^{-5}$ eV (0.400 and 0.237 meV) to within 1 μeV, the reduction expected from the higher temperature; the weakest in-plane state, $D_b = 0.5$ meV, has the same $\Delta^\star(0)$. A layer-odd out-of-plane exchange of 1 meV thus has no measurable effect on the condensate. The residual differences between the parallel and one-sided states scale as $D_{-,z}^2$. Their normal-state free energies differ by 2.7×10^{-8} and 1.09×10^{-7} eV per cell for $D_{-,z} = 0.25$ and 0.5 meV. This follows from σ_h. With spin–orbit coupling, σ_h (which leaves the in-plane $\mathbf{k}$ unchanged) acts as $z \to -z$ combined with is_z, so the Bloch states at every $\mathbf{k}$ are σ_h eigenstates with eigenvalues $\pm i$. The exchange $D_{-,z}s_z(n_b - n_t)$ is σ_h odd and therefore has no diagonal matrix elements in this basis, so it shifts nondegenerate energies only at second order. Its off-diagonal elements connect opposite mirror eigenvalues. At the Fermi level this requires the small admixture of σ_h-odd orbitals to the Nb-d-dominated bands (Sec. S6.3); otherwise it reaches only bands far from E_F. A first-order effect is possible only where bands of opposite mirror eigenvalue are degenerate, i.e., at the crossings of the spin-split bands on the nodal lines of the Ising splitting (Γ–M), and it is small for the same reason. The computed $D_{-,z}^2$ scaling shows that the condensate responds at second order in the investigated range. Because the parallel and one-sided states differ only at this level and are computed on the same quadrature, the converged one-sided value at $L = 3$ applies to the parallel texture with the same $D_{+,z}$.

Pair breaking by the four components. The components also differ in their effect on the condensate. Relative to the AP$_z$ value, $E_{\rm gap}(0) = 0.2365$ meV, the layer-even out-of-plane exchange reduces the spectral gap linearly, $E_{\rm gap}(0) \simeq (0.238 - 0.421|D_{+,z}|/\text{meV})$ meV for $|D_{+,z}| \leq 0.5$ meV, and the state is gapless at $D_{+,z} = 0.75$ meV (Table S8). It acts as a Zeeman field along the Ising axis, and $\bar{K}_c$ falls from 97 to 93.9, 83.6, 49.0, and 5.6 A/m for $D_{+,z} = 0.125$, 0.25, 0.5, and 0.75 meV. Ising spin–valley locking protects the condensate against in-plane exchange, which reduces the gap much more weakly. For the in-plane states the relevant gap is that at the equilibrium momentum, since $\mathbf{Q} = 0$ is Doppler shifted away from the helical minimum. Relative to the AP$_z$ value, $E_{\rm gap}(Q_{\rm eq})$ is reduced by less than 0.01, by 0.03, and by 0.08 meV for the one-sided textures with $D_{+,\parallel} = D_{-,\parallel} = 0.25$, 0.5, and 0.75 meV, faster than linearly in the exchange. The reduction is controlled by $D_{+,\parallel}$: the two-sided textures with $(D_{+,\parallel}, D_{-,\parallel}) = (0.75, 0.25)$ and $(0.25, 0.75)$ meV give 0.08 and 0.01 meV, and the AP texture, $(0, 1)$ meV, gives 0.01 meV. These reductions are accurate to the few-μeV interpolation error stated in Sec. S4.1. A cross term $D_{+,\parallel}D_{-,\parallel}$ is forbidden by σ_h, and $\bar{K}_c = 96.4 \pm 0.4$ A/m is unchanged throughout. The layer-odd out-of-plane exchange has no measurable effect. Only $D_{+,z}$ is pair breaking at linear order, which is why it suppresses the helical channel of tilted textures (Sec. S4.1) while the in-plane components leave the trigonal channel intact (below).

Tilted textures along $\hat{\mathbf{x}}$. For the one-sided tilted textures, the scan along $\hat{\mathbf{x}}$ is shifted to pass through $\mathbf{Q}_{\rm eq} = Q_{\rm eq}\hat{\mathbf{y}}$ (Table S8, block v). M_x keeps D_x and Q_y and reverses D_z and Q_x, so that η_x is odd in D_z; $M_x\mathcal{T}$ reverses D_x and Q_y and keeps D_z and Q_x, so that η_x is even in D_x. An in-plane component alone gives no rectification along $\hat{\mathbf{x}}$. At $L = 3$, the $\theta = 45°$ texture ($D_x = D_z = 0.71$ meV) gives $\eta = -0.735\%$ (-0.738% from $d(\Omega_{\rm SC} - \Omega_{\rm N})/dQ$). The purely out-of-plane $L = 3$ values at $D_z = 0.5$ and 1 meV, interpolated as a power of D_z (exponent 1.98), give -0.729% at $D_z = 0.71$ meV, a ratio of 1.01. At $L = 2$, where the tilted and purely out-of-plane states carry similar quadrature errors, the ratios are 1.01, 1.00, and 0.92 for $\theta = 30°$, 45°, and 60°. The mean critical currents along $\hat{\mathbf{x}}$ likewise follow D_z. An in-plane exchange of up to 0.87 meV thus leaves the trigonal channel essentially unchanged, while an out-of-plane component strongly suppresses the helical one. The mutual influence is asymmetric because only $D_{+,z}$ is pair breaking at linear order.

Angular dependence. At $L = 3$, $\eta(10°) = -1.280\%$ and $\eta(20°) = -0.771\%$ (-1.270% and -0.766% from $d(\Omega_{\rm SC} - \Omega_{\rm N})/dQ$), so that $\eta(\varphi_Q)/\eta(0°) = 0.884$ and 0.532, against $\cos 3\varphi_Q = 0.866$ and 0.500. Both excesses follow from a small $\cos 9\varphi_Q$ harmonic, the next term allowed by C_3, $M_x\mathcal{T}$, and the oddness in $\mathbf{Q}$. The form $\eta(\varphi_Q) \propto \cos 3\varphi_Q + a_9 \cos 9\varphi_Q$ with $a_9 = -0.021$, fixed by the ratio at 20°, predicts 0.885 at 10°, within 0.001 of the computed value. Along the mirror line ($\varphi_Q = 90°$) the efficiency vanishes to -0.003% (Fig. 2(c) of the main text).

Exchange strength. At $L = 3$, $D_b = 0.5$ meV gives $\eta = -0.367\%$ (-0.366% from $d(\Omega_{\rm SC} - \Omega_{\rm N})/dQ$). With -1.447% at $D_b = 1$ meV and -3.354% at 1.5 meV, $\eta/D_b^2 = -1.47$, -1.45, and $-1.49\%/\text{meV}^2$, with mean $-1.47\%/\text{meV}^2$. Over this range the efficiency grows as the square of the exchange; it remains odd in $D_{+,z}$ by time reversal. The $D_b = 1.5$ meV value is taken at $L = 2$, where the spurious fraction is 0.01: its critical momenta are three times smaller than at 1 meV, and the $3m'$-symmetric quadrature error, which is odd and cubic in Q, is correspondingly negligible. The quadratic growth combines a current asymmetry that peaks near 1 meV ($\Delta K = -0.61$, -1.42, and -0.38 A/m) with a collapsing current scale ($\bar{K}_c = 83.6$, 49.0, and 5.6 A/m) as $D_{+,z}$ closes the spectral gap. The efficiency of the trigonal channel exceeds that of the helical channel, $-0.955\% \times \Delta D_x/\text{meV}$, for exchange above 0.65 meV. At smaller exchange the growth is steeper. $D_b = 0.25$ meV

gives $\eta = -0.058\%$ (-0.055% from $d(\Omega_{SC} - \Omega_N)/dQ$, $L = 3$), below the -0.092% of the quadratic law; between 0.25 and 0.5 meV, $\eta \propto D_b^{2.7}$. No term linear in the exchange is resolved. The current asymmetry also changes sign along the branch: at $D_b = 0.25$ meV, $K_x(Q) + K_x(-Q)$ is positive, up to $+0.45$ A/m, while the spectrum is gapped, and turns negative once the gap closes at $|Q_x| \approx 2.4 \times 10^{-4}$ Å^{-1}, before the critical momenta. The critical-current asymmetry thus results from a partial cancellation of two contributions of opposite sign, the second of which appears only in the gapless regime and dominates at larger exchange. As a function of the critical-current suppression, which a spin valve measures directly through its P_z and AP_z states (Table S8, block ii), the efficiency is -0.06, -0.37, -1.45, and -3.4% at $\bar{K}_c/\bar{K}_c(AP_z) = 0.97$, 0.86, 0.50, and 0.06 ($D_b = 0.25$, 0.5, 1, and 1.5 meV).

Temperature. At $L = 3$, $\eta = -3.372\%$, -1.447%, and -0.323% for $k_BT = 10^{-5}$, 5×10^{-5}, and 10^{-4} eV (0.12, 0.58, and 1.16 K), a tenfold change, against 2.4 for the helical channel (Sec. S6.2). The current asymmetry changes by a factor of 35 ($\Delta K = -4.38$, -1.42, and -0.125 A/m) and the current scale by 3.4 ($\bar{K}_c = 65.0$, 49.0, and 19.4 A/m). The spectral gap at $\mathbf{Q} = 0$ is 36 and 27 μeV at the two lower temperatures, and the state is gapless at 10^{-4} eV. At $k_BT = 10^{-5}$ eV, $K_x(Q_x)$ develops a cusp on the $+Q_x$ side at $Q_x \approx 1.9 \times 10^{-4}$ Å^{-1}, where $\Delta^\star$ starts to fall linearly, while the $-Q_x$ side peaks smoothly at a larger $|K|$. The asymmetry thus originates in the nearly gapless, exchange-split quasiparticles, whose structure on the scale of tens of μeV is washed out by thermal smearing.

S5. CARRIER DEPENDENCE

This section documents the chemical-potential dependence of the in-plane states. All calculations use the production quadrature, $k_BT = 5 \times 10^{-5}$ eV, and the same g_{SC} at every filling, so that the exchange field and the pairing interaction are fixed and only μ is varied. Here $\delta\mu = \mu - \mu_0$, and the Brillouin-zone refinement is rebuilt for each μ.

S5.1. Chemical-potential dependence

Table S9 and Fig. S6 show the one-sided in-plane state over $-20 \le \delta\mu \le 20$ meV and the AP texture over ± 5 meV. The three observables respond to filling in different ways. Q_{eq} varies linearly and very weakly, from -18.00 to -17.73×10^{-6} Å^{-1}, with the same relative slope for the AP texture [Fig. S6(b)]. The current scale varies strongly: K_{scale} decreases by a factor of 2.6, from 305 to 115 A/m, while $\Delta^\star(0)$ decreases from 0.557 to 0.290 meV. The filling changes the density of states at the Fermi level, and with it the gap at fixed g_{SC}. The diode numerator K_{diode} follows the current scale, decreasing in magnitude from 2.36 to 1.09 A/m. As a result, the efficiency stays between -0.78% and -0.95% over the whole scan, with no sign change and no near-zero value [Fig. S6(a)].

For the AP texture, $\eta = -1.82\%$, -1.90%, and -1.85% at $\delta\mu = -5$, 0, and $+5$ meV, which is 2.06, 1.95, and 2.01 times the one-sided value at the same filling and the same spacing $dq = 4 \times 10^{-6}$ (Table S4 for $\delta\mu = 0$ and $+5$ meV). The linear dependence on ΔD_x established at μ_0 (Sec. S4.2) thus holds at every filling studied.

S5.2. Filling dependence on uniform meshes

On uniform meshes, η appears to depend strongly on filling. At $k_BT = 5 \times 10^{-5}$ eV (Table S3), the one-sided state gives -0.68% at μ_0 but -0.13% at $\delta\mu = +5$ meV on the $N = 261$ mesh, whereas the $N = 333$ mesh gives the opposite trend, -0.55% and -1.38%. Section S3.1 shows that this structure is a Brillouin-zone sampling artifact: on uniform meshes the error in η is comparable to the variations themselves, whereas the converged efficiencies at μ_0 and $\mu_0 + 5$ meV agree within 0.03 percentage points. On the Fermi-surface-adaptive quadrature, K_{diode} and K_{scale} vary smoothly and nearly in proportion, so that their ratio η stays between -0.78% and -0.95% over 40 meV. Within this model, carrier filling therefore changes the current scale by a factor of 2.6 but the rectification efficiency by less than 20%.

S6. SUPERCONDUCTING STABILITY, TEMPERATURE DEPENDENCE, AND MODEL ROBUSTNESS

S6.1. Representative finite-Q superconducting branch

Figure S7(a)–(c) shows the full self-consistent branch of the AP state at μ_0 on the production quadrature. The pairing amplitude is nearly constant, $\Delta^\star \simeq 0.398$ meV, over the central region. It decreases once the quasiparticle gap closes and drops steeply near the branch ends. The minimum BdG energy E_{gap} is 0.23 meV near Q_{eq} and decreases linearly with $|Q_y - Q_{eq}|$, as expected from the Doppler shift. It vanishes at $Q_y = +2.04$ and -2.80×10^{-4} Å^{-1} (shaded regions). The condensation energy $\Delta\Omega$ is negative over the whole branch and has its minimum at Q_{eq}. The current is linear around Q_{eq} and reaches its extrema inside the gapless regions, at $Q_c^+ = +2.29$ and $Q_c^- = -3.05 \times 10^{-4}$ Å^{-1}. The critical currents of this model therefore correspond to gapless depairing, where $\Delta^\star$ is still close to its zero-current value. This is why their Brillouin-zone convergence is more demanding than that of Q_{eq} (Sec. S3.1). The asymmetry of the two gap-closing momenta about Q_{eq} already sig-

TABLE S8. **Out-of-plane, two-sided out-of-plane, and tilted textures** (production quadrature, $\mathbf{Q} \parallel \hat{\mathbf{x}}$ unless noted, $k_BT = 5 \times 10^{-5}$ eV unless noted). D_t, D_b, and $D_{+,z} = (D_{b,z} + D_{t,z})/2$ are z components in meV. $\eta_{\Delta\Omega}$ is the efficiency from $d(\Omega_{\rm SC} - \Omega_{\rm N})/dQ$; a large difference from η signals an unconverged quadrature (Sec. S4.6). $\Delta^\star(0)$ and $E_{\rm gap}(0)$ are in meV; for block v, $E_{\rm gap}$ is taken at the origin of the scan line, $\mathbf{Q} = Q_{\rm eq}\hat{\mathbf{y}}$. Other units as in Table S6.

State	D_t	D_b	$D_{+,z}$	L	$Q_{\rm eq}$	K_c^+	K_c^-	η (%)	$\eta_{\Delta\Omega}$ (%)	$\Delta^\star(0)$	$E_{\rm gap}(0)$
(i) One-sided, $\theta = 0°$											
Bottom only	0	0.25	0.125	3	−0.01	93.82	−93.93	−0.058	−0.055	0.398	0.186
Bottom only	0	0.5	0.25	2	−0.02	83.01	−83.73	−0.435	−0.098	0.397	0.135
	0	0.5	0.25	3	−0.01	83.34	−83.95	−0.367	−0.366	0.397	0.135
Bottom only	0	1	0.5	2	0.06	47.97	−49.60	−1.668	−1.107	0.385	0.027
	0	1	0.5	3	0.05	48.26	−49.68	−1.447	−1.437	0.385	0.027
	0	1	0.5	4	0.05	48.26	−49.68	−1.452	−1.445	0.385	0.027
Bottom only	0	1.5	0.75	2	0.34	5.40	−5.78	−3.354	−3.425	0.312	0.000
(ii) Two-sided, $\theta = 0°$											
P_z	0.25	0.25	0.25	2	−0.01	83.01	−83.73	−0.435	−0.097	0.397	0.135
P_z	0.5	0.5	0.5	2	0.06	47.97	−49.60	−1.667	−1.107	0.385	0.027
AP_z	−1	1	0	2	0.00	97.07	−97.07	0.000	0.000	0.399	0.236
(iii) Scan direction, one-sided $D_b = 1$ meV											
$\varphi_Q = 10°$	0	1	0.5	2	0.05	48.17	−49.61	−1.471	−0.994	0.385	0.027
	0	1	0.5	3	0.05	48.44	−49.70	−1.280	−1.270	0.385	0.027
$\varphi_Q = 20°$	0	1	0.5	2	0.05	48.67	−49.53	−0.883	−0.614	0.385	0.027
	0	1	0.5	3	0.05	48.92	−49.67	−0.771	−0.766	0.385	0.027
$\varphi_Q = 90°$ ($\hat{\mathbf{y}}$)	0	1	0.5	2	0.00	49.35	−49.35	−0.003	−0.004	0.385	0.027
(iv) Temperature, one-sided $D_b = 1$ meV											
$k_BT = 10^{-5}$ eV	0	1	0.5	2	−0.05	62.76	−67.52	−3.652	−2.794	0.400	0.035
	0	1	0.5	3	−0.05	62.79	−67.18	−3.372	−3.323	0.400	0.036
$k_BT = 10^{-4}$ eV	0	1	0.5	2	0.06	19.12	−19.32	−0.529	−0.227	0.304	0.000
	0	1	0.5	3	0.06	19.30	−19.43	−0.323	−0.309	0.305	0.000
(v) One-sided tilted, $\lvert\mathbf{D}_b\rvert = 1$ meV (z components listed), scan line through $Q_{\rm eq}\hat{\mathbf{y}}$											
$\theta = 30°$	0	0.87	0.43	2	0.01	58.63	−60.15	−1.277	−0.776	0.390	0.055
$\theta = 45°$	0	0.71	0.35	2	−0.02	70.16	−71.37	−0.853	−0.416	0.394	0.088
	0	0.71	0.35	3	−0.02	70.45	−71.50	−0.735	−0.738	0.394	0.088
$\theta = 60°$	0	0.50	0.25	2	−0.02	82.77	−83.43	−0.402	−0.065	0.397	0.131

TABLE S9. **Carrier scans** (production quadrature, $k_BT = 5 \times 10^{-5}$ eV). $\delta\mu$ and $\Delta^\star(0)$ are in meV, $Q_{\rm eq}$ in 10^{-6} Å^{-1}, and currents in A/m. $K_{\rm diode} = K_c^+ + K_c^-$ and $K_{\rm scale} = K_c^+ - K_c^-$ [Eq. (S59)]. † $dq = 2 \times 10^{-6}$; all other rows $dq = 4 \times 10^{-6}$.

$\delta\mu$	$\Delta^\star(0)$	$Q_{\rm eq}$	K_c^+	K_c^-	$K_{\rm diode}$	$K_{\rm scale}$	η (%)
One-sided, $\theta = 90°$, $D_b = 1$ meV							
−20	0.557	−18.00	151.09	−153.45	−2.36	304.54	−0.775
−10	0.470	−17.93	120.87	−122.99	−2.12	243.86	−0.869
−5	0.432	−17.88	107.98	−109.90	−1.92	217.88	−0.881
0†	0.398	−17.86	95.64	−97.48	−1.84	193.12	−0.952
+5†	0.367	−17.83	85.18	−86.77	−1.59	171.95	−0.925
+10	0.339	−17.80	74.85	−76.20	−1.35	151.05	−0.893
+20	0.290	−17.73	57.13	−58.23	−1.09	115.36	−0.948
AP							
−5	0.432	−35.76	106.52	−110.46	−3.94	216.98	−1.818
0	0.398	−35.71	94.18	−97.82	−3.64	192.00	−1.895
+5	0.367	−35.66	83.80	−86.95	−3.15	170.75	−1.845

nals the direction-dependent depairing that underlies the diode effect.

S6.2. Temperature dependence

Figure S7(d)–(f) shows the one-sided in-plane state at μ_0 for $k_BT = 10^{-5}$, 5×10^{-5}, and 10^{-4} eV, with $g_{\rm SC}$ fixed. $\Delta^\star(0)$ is 0.400, 0.398, and 0.362 meV, while $Q_{\rm eq}$ (-17.87, -17.86, and -17.81×10^{-6} Å^{-1}) changes by

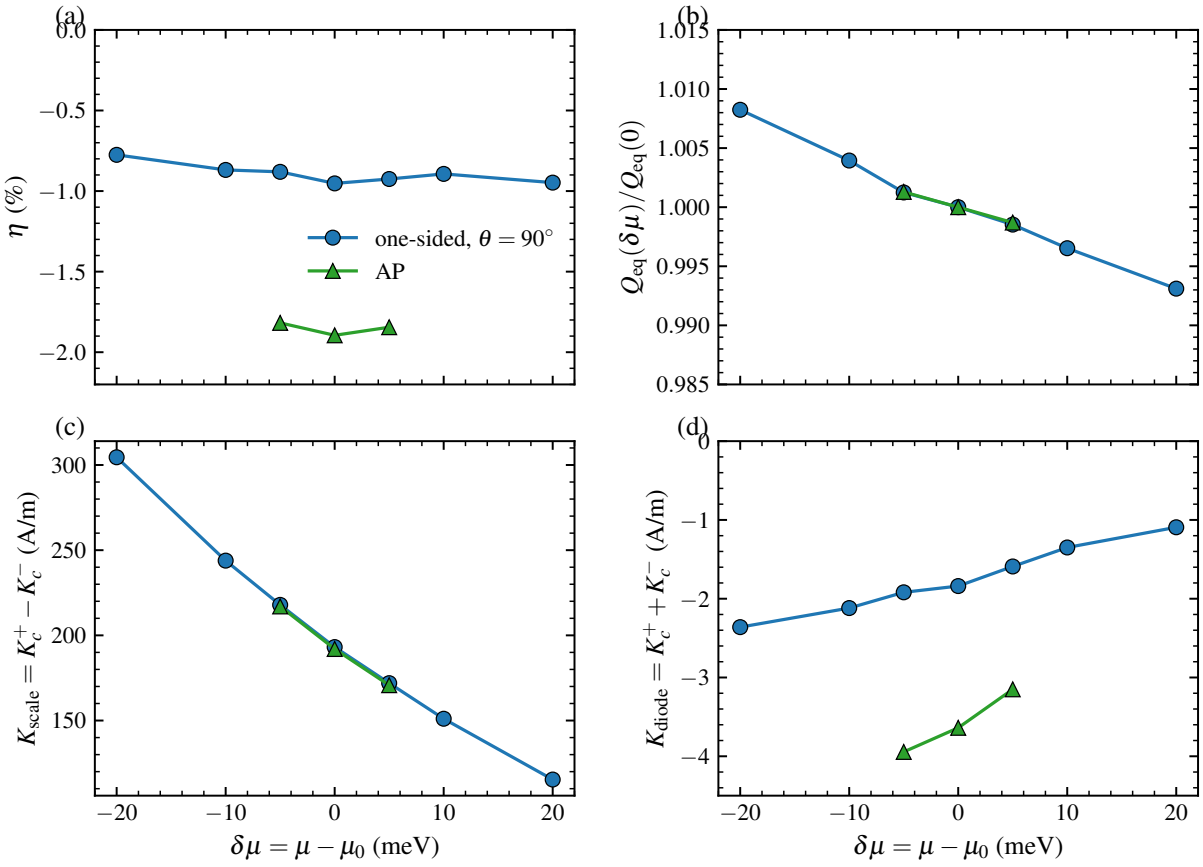


FIG. S6. **Carrier dependence of the finite-Q observables** (production quadrature, $k_BT = 5 \times 10^{-5}$ eV) for the one-sided in-plane state ($D_b = 1$ meV, $\theta = 90°$, $\phi = 0°$) and the AP texture. (a) Diode efficiency η. (b) Equilibrium momentum normalized to its value at $\delta\mu = 0$. (c) Critical-current scale $K_{\rm scale} = K_c^+ - K_c^-$. (d) Diode numerator $K_{\rm diode} = K_c^+ + K_c^-$.

only 0.06×10^{-6} Å^{-1}. Fitting $\Delta^\star(0)$ to the BCS temperature dependence gives $T_c \approx 1.9$ K, close to the onset temperature measured for single-layer $NbSe_2$ [14], so that the three temperatures are about 0.06, 0.3, and $0.6\,T_c$. Over the same range, $K_{\rm scale}$ falls by a factor of 2.5, from 237.3 to 95.8 A/m, and $|K_{\rm diode}|$ by a factor of 5.8, from 2.79 to 0.48 A/m. The efficiency therefore decreases in magnitude from -1.18% to -0.95% to -0.50%. Temperature thus changes η by a factor of about 2.4 while the helical momentum changes by a relative 3×10^{-3}, another instance of the separation between the two observables. The values at $k_BT = 10^{-5}$ and 10^{-4} eV were obtained with $L = 2$. There, η and the efficiency from $d(\Omega_{\rm SC} - \Omega_{\rm N})/dQ$ agree to within 0.006 percentage points (-1.176% against -1.171%, and -0.496% against -0.502%), and the spurious fraction is at most 0.02. These values thus pass the same diagnostics as the production states of Sec. S3.1, although no $L = 3$ comparison was made at these temperatures. The out-of-plane channel is far more sensitive to temperature (Sec. S4.6).

Sign-reversed helical state. The tilted state with $\theta = 45°$ and $D_b = 1.75$ meV (Sec. S4.1) was recomputed at the same three temperatures ($L = 3$, same $g_{\rm SC}$). It gives $\eta = +0.300\%$, $+0.354\%$, and -0.012% at 0.12, 0.58, and 1.16 K ($+0.318\%$, $+0.360\%$, and -0.013% from $d(\Omega_{\rm SC} - \Omega_{\rm N})/dQ$), i.e., -0.21, -0.30, and $+0.02$ times the in-plane efficiency at the same ΔD_x and temperature. The current scale falls from $\bar{K}_c = 43.9$ to 28.3 to 6.9 A/m (0.37, 0.29, and 0.14 of the in-plane values), the current asymmetry from $K_c^+ - |K_c^-| = +0.26$ to $+0.20$ to -0.002 A/m, and $\Delta^\star(0)$ from 0.394 to 0.366 to 0.240 meV; the state is gapless along the whole branch at all three temperatures. The reversed sign thus persists on cooling, whereas at 1.16 K the net asymmetry vanishes within accuracy. The back-flow of the depaired K and K' pockets, which carries the reversal, is a property of the nearly gapless spectrum on the scale of tens of μeV and is washed out by thermal smearing, as for the trigonal channel (Sec. S4.6). The reversal is therefore a low-temperature effect. Its helical momentum, $Q_{\rm eq} = -20.66$, -21.51, and -22.63×10^{-6} Å^{-1}, changes by 2.0×10^{-6} Å^{-1} over this range, more than in the in-plane state but still less than 10%.

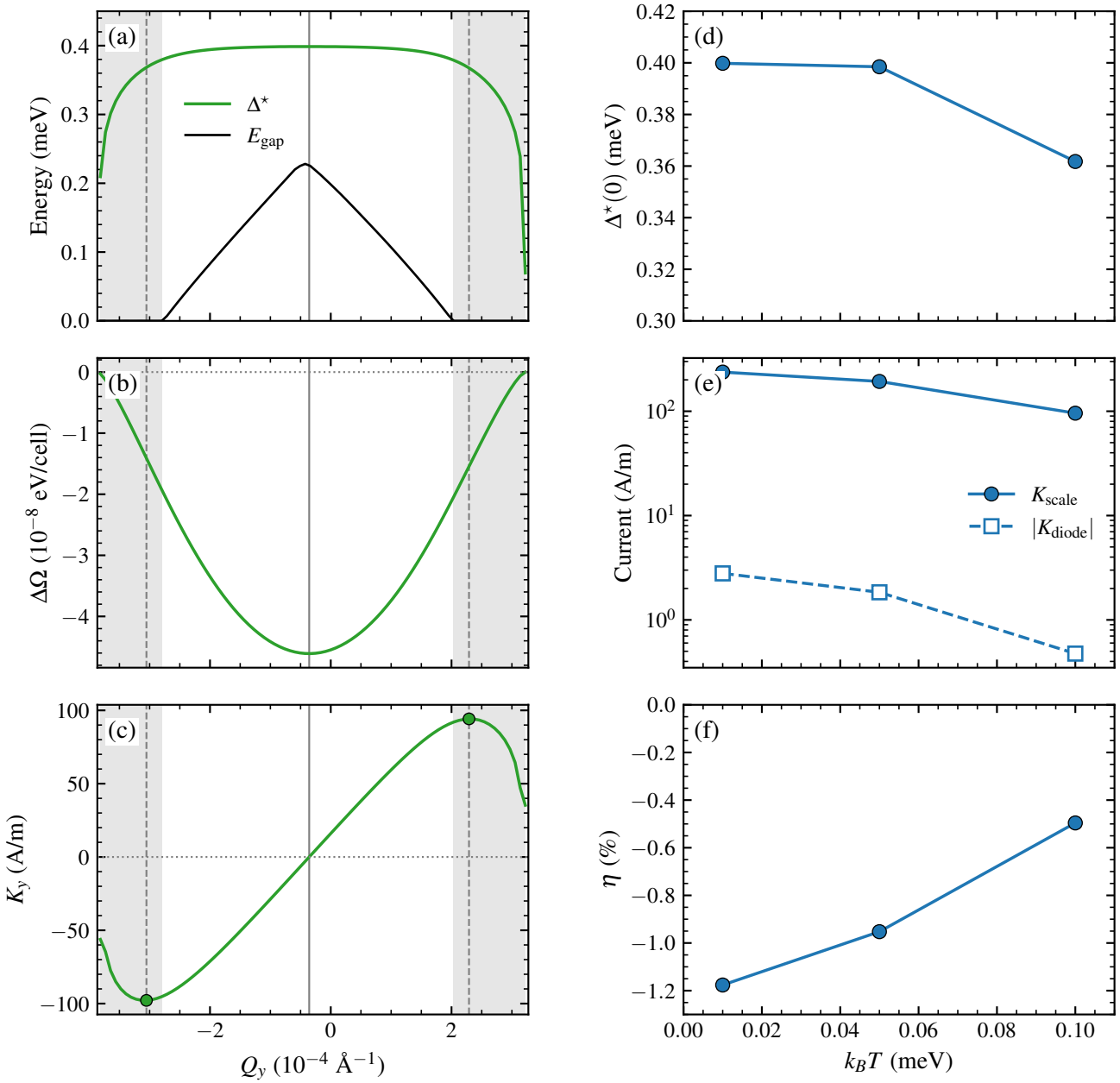


FIG. S7. **Superconducting branch and temperature dependence** (production quadrature). (a)–(c) AP state at μ_0, $k_BT = 5\times10^{-5}$ eV: (a) $\Delta^\star(Q_y)$ and the minimum BdG energy $E_{\rm gap}(Q_y)$, (b) condensation energy $\Delta\Omega(Q_y)$, and (c) sheet current $K_y(Q_y)$ with $K_c^\pm$ marked. The solid vertical line is $Q_{\rm eq}$, dashed lines are $Q_c^\pm$, and shaded regions are gapless ($E_{\rm gap} < 5$ μeV). (d)–(f) Temperature dependence of the one-sided in-plane state at μ_0: (d) $\Delta^\star(0)$, (e) $K_{\rm scale}$ and $|K_{\rm diode}|$ on a logarithmic scale, and (f) η.

S6.3. Gap magnitude and choice of pairing subspace

Gap magnitude. To test how the results depend on the size of the superconducting gap, $g_{\rm SC}$ was recalibrated on the production quadrature so that the no-exchange gap is $\Delta^\star = 0.6$ meV at $k_BT = 10^{-5}$ eV, instead of 0.4 meV ($g_{\rm SC} = 0.52605$ against 0.50068 eV at $L = 2$, and 0.52606 against 0.50072 eV at $L = 3$). Three states were recomputed at $k_BT = 5\times10^{-5}$ eV (Table S10). The helical momentum is nearly independent of the gap: $Q_{\rm eq} = -17.87$ against -17.86×10^{-6} Å^{-1} for the one-sided in-plane state. Its current scale grows by a factor of 1.71 and its current asymmetry by 1.38, so that η decreases in magnitude from -0.974% to -0.785% (both with $dq = 4\times10^{-6}$; Table S4). The out-of-plane state with $D_b = 1$ meV behaves differently. Its current asymmetry and current

scale both grow by a factor of about 2.6, and η changes only from -1.447% to -1.508%. With the larger gap the trigonal channel is therefore 1.92 times stronger than the helical one, against 1.49 at $\Delta^\star = 0.4$ meV (in-plane values at $L = 2$ and $dq = 4 \times 10^{-6}$ in both cases; 1.52 with the $dq = 2 \times 10^{-6}$ value of Table S10). The trigonal efficiency is not a function of $D_z/\Delta^\star$ alone. The out-of-plane state with $D_b = 1.5$ meV at $\Delta^\star = 0.6$ meV, which has the same ratio as $D_b = 1$ meV at 0.4 meV, gives $\eta = -2.428\%$. The largest efficiency occurs close to the depairing limit: $D_b = 1.5$ meV at $\Delta^\star = 0.4$ meV, which is gapless at $\mathbf{Q} = 0$ with $\bar{K}_c = 5.6$ A/m and is the lowest-grand-potential solution at the tested momenta (Sec. S6.5), gives -3.354%, whereas the same exchange with the larger gap gives -2.428% with $\bar{K}_c = 85.2$ A/m. The qualitative conclusions of the main text, the gap-independent helical momentum and the larger trigonal efficiency, thus hold for both gaps.

Pairing subspace. The main calculations restrict local singlet pairing to Nb d_{z^2}, $d_{x^2-y^2}$, and d_{xy}. This is the standard choice in models of Ising superconductivity in monolayer $NbSe_2$, where the same three orbitals and an intra-orbital attraction are used [34], and it is consistent with the conventional phonon-mediated pairing obtained from first principles [35]. In our Wannier model these σ_h-even orbitals carry 0.73 of the spectral weight at E_F (d_{z^2} 0.30, $d_{x^2-y^2}$ and d_{xy} 0.22 each), the Se p orbitals 0.27, and the σ_h-odd d_{xz} and d_{yz} only 0.001 (orbital-projected density of states at μ_0 on a 150×150 mesh, Gaussian broadening of 5 to 20 meV; the fractions change by less than 0.003). The Se weight belongs to the same hybridized bands, so the anomalous amplitude on the Se orbitals is generated self-consistently even without a pairing interaction there. An on-site, orbital-diagonal singlet in d_{xz} and d_{yz}, or one that is equal on the two Se sublayers, is invariant under all symmetries of the model. Including it would therefore leave the symmetry analysis of Secs. S1 and S4 unchanged and would only redistribute the gap among the bands; its overall scale is fixed by the calibration of Sec. S2.3, and we have not tested its effect on the magnitudes. The interaction is singlet only. The triplet correlations that the exchange and the Ising spin–orbit coupling induce are contained in the BdG Green's function, but an attractive triplet channel, which can reshape the in-plane diode response [13], is not included.

S6.4. Scope of the proximity model

The layer-selective on-site exchange of Eq. (S29) is an effective proximity self-energy acting on the Se p orbitals. The model does not include an explicit magnetic substrate, interface reconstruction, charge transfer, or interface-induced changes of the hopping amplitudes. In a real heterostructure, charge transfer would shift μ, and interface hybridization would add layer-odd hopping terms that break σ_h even without magnetism. Both effects are allowed by symmetry, and the second would contribute to Q_{eq} only together with time-reversal breaking.

The induced exchange of a real interface is also not confined to the interfacial Se layer. It generally extends to the Nb d orbitals, which carry most of the Fermi-surface weight. Because Nb lies in the σ_h plane, σ_h maps the Nb site onto itself, so that an exchange field on Nb transforms as the layer-even components: an in-plane Nb field behaves as $D_{+,\parallel}$ and an out-of-plane Nb field as $D_{+,z}$ [Eq. (S71)]. The selection rules are therefore unchanged. For in-plane magnetization, an Nb field cannot rectify on its own; it adds pair breaking, which Ising spin–valley locking weakens, and the helical channel remains controlled by the layer-odd Se contrast. For out-of-plane magnetization, it contributes directly to the trigonal channel and to its pair breaking. The relative size of the Nb and Se components, and with it the magnitude of η, depends on the interface and has to be determined for a specific heterostructure.

The selection rules of Secs. S1 and S4 hold for any extension of the model that preserves the relevant magnetic symmetries: $\sigma_h\mathcal{T}$ for the reciprocity of parallel in-plane and antiparallel out-of-plane textures, and $M_x\mathcal{T}$ and C_3 for the trigonal channel. Interface terms that break them, such as an asymmetric interface potential or Rashba coupling on one side, can add responses; the exact reciprocity of these textures assumes mirror-equivalent interfaces. For a one-sided interface, a layer-odd potential V_- allows, for example, a term $\mathbf{Q} \cdot (\hat{\mathbf{z}} \times \mathbf{D}_{+,\parallel})V_-$, so that the layer-even in-plane exchange can then contribute in proportion to V_-; we have not computed its size. The magnitudes of Q_{eq} and η are model-specific. The results should therefore be read as microscopic design principles within a controlled effective model, not as parameter-free predictions for a particular heterostructure. The uniform-amplitude finite-Q ansatz also excludes vortex entry, inhomogeneous depairing, and contact effects. The computed $K_c^{\pm}$ are therefore intrinsic depairing currents, which bound but need not equal measured switching currents. Field-free rectification with a zero-momentum condensate, the signature of the trigonal channel, has been reported in $NbSe_2/CrBr_3$ heterostructures with out-of-plane magnetization, with efficiencies of several tens of percent [21]. A quantitative comparison with the intrinsic values computed here would require the interface-specific exchange and the switching mechanism of the device.

Broadening and layer number. The calculations are for clean monolayers. The sign reversal of the helical channel and the dominance of the trigonal channel originate in structure of the nearly gapless spectrum on the scale of tens of μeV: both are present for $k_BT \leq 5 \times 10^{-5}$ eV and are removed by thermal smearing at 10^{-4} eV (Secs. S4.6 and S6.2). Disorder or Dynes broadening of comparable size is expected to act similarly, so that these two features require broadening well below 0.1 meV, whereas the selection rules do not. The rules themselves are for the monolayer. In a $2H$ bilayer, the two layers are related by inversion, which keeps axial vectors and reverses $\mathbf{Q}$. A

TABLE S10. **Dependence on the gap magnitude** (production quadrature, $k_BT = 5 \times 10^{-5}$ eV). $\Delta_N^\star$ is the calibrated no-exchange gap at $k_BT = 10^{-5}$ eV; the in-plane state is scanned along $\hat{\mathbf{y}}$ and the out-of-plane states along $\hat{\mathbf{x}}$. $\Delta_N^\star$, $\Delta^\star(0)$, and $E_{\rm gap}(0)$ in meV; other units as in Table S6. For the in-plane state $\mathbf{Q} = 0$ is not the equilibrium, so $E_{\rm gap}(0)$ there includes the Doppler shift of the helical state. † $dq = 2 \times 10^{-6}$; all other rows $dq = 4 \times 10^{-6}$.

State	$\Delta_N^\star$	L	$\Delta^\star(0)$	$E_{\rm gap}(0)$	$Q_{\rm eq}$	K_c^+	K_c^-	$\bar{K}_c$	η (%)	$\eta_{\Delta\Omega}$ (%)
In-plane, $D_b = 1$ meV†	0.4	2	0.398	0.189	−17.86	95.64	−97.48	96.56	−0.952	−0.980
	0.6	2	0.600	0.337	−17.87	163.46	−166.05	164.75	−0.785	−0.801
Out-of-plane, $D_b = 1$ meV	0.4	3	0.385	0.027	0.05	48.26	−49.68	48.97	−1.447	−1.437
	0.6	3	0.599	0.153	−0.04	123.14	−126.92	125.03	−1.508	−1.506
Out-of-plane, $D_b = 1.5$ meV	0.4	2	0.312	0.000	0.34	5.40	−5.78	5.59	−3.354	−3.425
	0.6	3	0.593	0.049	0.05	83.09	−87.23	85.16	−2.428	−2.418

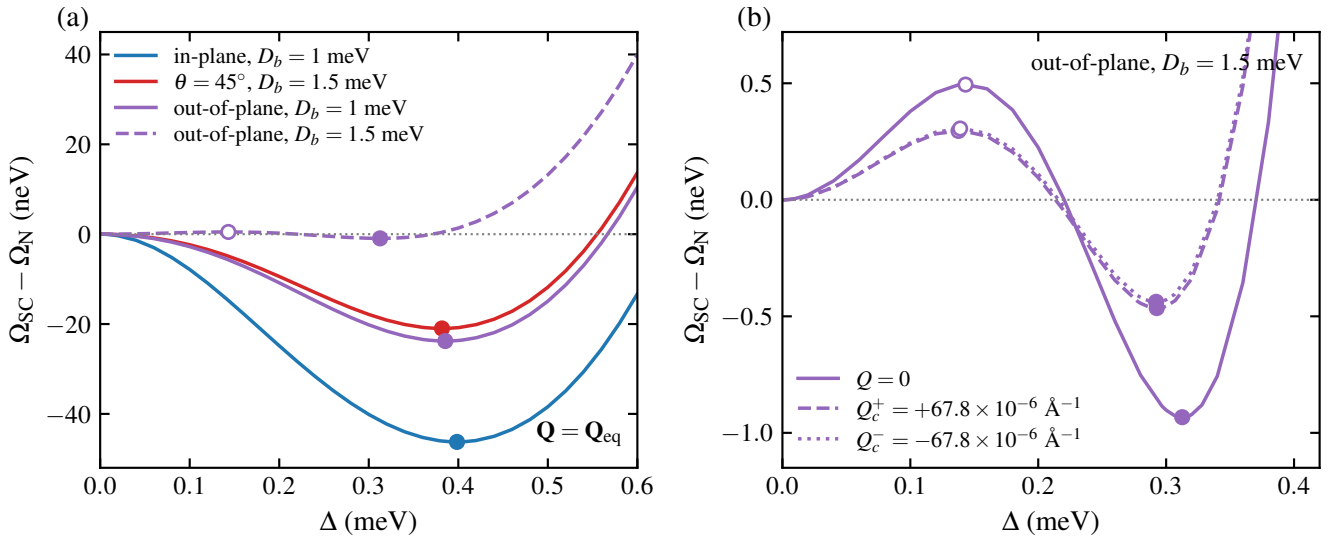


FIG. S8. **Stability of the selected solutions within the scalar-gap ansatz** (production quadrature, $k_BT = 5 \times 10^{-5}$ eV). Grand potential relative to the normal state, $\Omega_{\rm SC}(\Delta) - \Omega_{\rm N}$, per primitive cell at fixed $\mathbf{Q}$. (a) Four states of Table S11 (in-plane; tilted, $\theta = 45°$, $D_b = 1.5$ meV; out-of-plane, $D_b = 1$ and 1.5 meV) at the equilibrium momentum ($\mathbf{Q} = 0$ for the out-of-plane states). (b) Out-of-plane state with $D_b = 1.5$ meV at $\mathbf{Q} = 0$ and at the critical momenta. Filled circles are roots of G that are minima of $\Omega_{\rm SC}(\Delta)$ (the production $\Delta^\star$); open circles are roots that are maxima.

texture with parallel exchange on the two outer Se layers is then inversion symmetric and reciprocal for any orientation, whereas an antiparallel texture may rectify. For out-of-plane exchange this is the reverse of the monolayer rule (Sec. S4.6). $2H$ stacks with an odd number of layers keep σ_h through the middle layer and follow the monolayer rules, so that out-of-plane spin valves should show an even–odd dependence on the layer number. By the same argument, a uniform out-of-plane field rectifies in even-layer $2H$ stacks only through inversion breaking by the substrate or the surfaces, which bears on the field-driven diode effect in few-layer $NbSe_2$ [17].

S6.5. Stability of the selected solutions within the scalar-gap ansatz

Section S2.5 shows that the largest root of the gap equation is always a local minimum of $\Omega_{\rm SC}(\Delta)$ and that continuation in Q preserves the character of the selected root up to a fold. We verified directly that the selected root is the largest one and examined the other solutions. For six states that cover the two channels, the most strongly depaired cases, and the sign-reversed helical states (one-sided in-plane $D_b = 1$ meV with $L = 2$; tilted $\theta = 45°$, $D_b = 1.5$ and 1.75 meV, and $\theta = 30°$, $D_b = 1.5$ meV, with $L = 3$; one-sided out-of-plane $D_b = 1$ meV with $L = 3$; one-sided out-of-plane $D_b = 1.5$ meV with $L = 2$), the residual $G(\Delta)$ and $\Omega_{\rm SC}(\Delta)$ were tabulated at the equilibrium momentum and at both critical momenta, on a grid from 0.002 to 0.6 meV refined around the production $\Delta^\star$. For the in-plane and tilted states the grid point nearest to $Q_{\rm eq}$ was used, and for the out-of-plane states $\mathbf{Q} = 0$; the critical momenta are those of the production branches.

Figure S8 and Table S11 summarize the result. The finite-difference derivative $\partial\Omega_{\rm SC}/\partial\Delta$ between neighboring grid points equals $-(2N_{\rm pair}/g_{\rm SC})G$, prefactor in-

TABLE S11. **Stability scan** (production quadrature, $k_BT = 5 \times 10^{-5}$ eV). For each state the rows are the equilibrium momentum (nearest grid point, or $\mathbf{Q} = 0$) and Q_c^+, Q_c^-. Q in 10^{-6} Å^{-1}; $\Delta^\star$, the production gap, and $E_{\rm gap}$ at $\Delta^\star$ in meV; $\Delta\Omega = \Omega_{\rm SC}(\Delta^\star) - \Omega_{\rm N}$ in neV per primitive cell. In all rows $\Delta^\star$ is the largest root of G and a minimum of $\Omega_{\rm SC}(\Delta)$. Δ_2 is the only other root (a maximum), and $\Delta\Omega_2$ is its grand potential relative to the normal state.

State	Q	$\Delta^\star$	$E_{\rm gap}$	$\Delta\Omega$	Δ_2 ($\Delta\Omega_2$)
In-plane,	−17.0	0.3985	0.209	−46.24	–
$D_b = 1$ meV,	250.1	0.3672	0	−14.79	–
$L = 2$	−288.3	0.3677	0	−14.11	–
Tilted 45°,	−17.0	0.3817	0.006	−20.99	–
$D_b = 1.5$ meV,	178.1	0.3279	0	−9.67	–
$L = 3$	−212.0	0.3297	0	−9.94	–
Tilted 45°,	−25.4	0.3667	0	−12.86	–
$D_b = 1.75$ meV,	135.7	0.3207	0	−7.07	–
$L = 3$	−178.1	0.3201	0	−7.13	–
Tilted 30°,	−17.0	0.3595	0	−10.10	–
$D_b = 1.5$ meV,	127.2	0.3186	0	−5.92	–
$L = 3$	−152.6	0.3183	0	−5.97	–
Out-of-plane,	0	0.3854	0.027	−23.78	–
$D_b = 1$ meV,	203.5	0.3322	0	−10.88	–
$L = 3$	−203.5	0.3347	0	−10.76	–
Out-of-plane,	0	0.3125	0	−0.93	0.143 (+0.49)
$D_b = 1.5$ meV,	67.8	0.2925	0	−0.46	0.138 (+0.30)
$L = 2$	−67.8	0.2920	0	−0.44	0.139 (+0.31)

cluded, to within 1.3×10^{-3} of its largest magnitude, and integrating $-(2N_{\rm pair}/g_{\rm SC})G$ over Δ reproduces $\Omega_{\rm SC} - \Omega_{\rm N}$ to within 4×10^{-3} of its range. This confirms the identity of Sec. S2.5, and with it the normalization of Eq. (S51), on the production quadrature. In all eighteen cases the production $\Delta^\star$ has $|G| < 0.7 \times 10^{-8}$ eV, within the tolerance of Sec. S3.3, and lies within 0.18 μeV of a root of G. This root is the largest one, a local minimum of $\Omega_{\rm SC}(\Delta)$, and the solution of lowest grand potential, the normal state included. Because $\Omega_{\rm SC}$ is stationary at the root, the small offset of $\Delta^\star$ affects $\Omega_{\rm SC}$, and hence K, only at second order.

For all states except the out-of-plane state with $D_b = 1.5$ meV, this root is the only one, including the two sign-reversed tilted states, which are gapless already at $Q_{\rm eq}$. $G > 0$ at all smaller Δ, so the normal state is a local maximum and $\Omega_{\rm SC}$ decreases monotonically up to $\Delta^\star$ [Fig. S8(a) and Table S11]. The out-of-plane state with $D_b = 1.5$ meV is qualitatively different [Fig. S8(b)]. There $G < 0$ as $\Delta \to 0$, so the normal state is itself a local minimum, and a second root near 0.14 meV is a maximum of $\Omega_{\rm SC}$ that separates it from the selected solution. This is the structure expected for a Zeeman field along the Ising axis near the Pauli limit, where the transition becomes first order at low temperature. At the tested momenta the selected solution nevertheless remains the global minimum. It lies 0.93 neV per primitive cell below the normal state at $\mathbf{Q} = 0$ and 0.44–0.46 neV below it at $Q_c^\pm$, while the maximum between them lies 0.3–0.5 neV above the normal state. The largest trigonal efficiency of Sec. S6.3, −3.354%, therefore belongs to the thermodynamically stable state, although one whose condensation energy is only 0.04 times that at $D_b = 1$ meV.

The selected root is thus a local minimum and the lowest-grand-potential scalar-gap solution at the equilibrium momentum and at both critical momenta. Between these momenta the production branch lies below the normal state at every Q (Sec. S2.5), and the extraction rule of Sec. S2.6 excludes abrupt steps of $\Delta^\star(Q)$. These checks establish a smooth branch that is the stable scalar-gap solution at the tested momenta. They do not exclude a competing superconducting solution that appears only between the tested momenta, which the single-minimum structure at both ends makes unlikely. Within these limits, the computed $K_c^\pm$ are depairing currents of the stable superconducting state. Stability against spatially varying amplitudes or other pairing channels is not tested here (Sec. S2.5).